Divergent Ca^{2+}/calmodulin feedback regulation of Ca_V1 and Ca_V2 voltage-gated calcium channels evolved in the common ancestor of Placozoa and Bilateria

Received for publication, August 7, 2021, and in revised form, February 10, 2022 Published, Papers in Press, February 16, 2022,
https://doi.org/10.1016/j.jbc.2022.101741

Julia Gauberg[1], **Wassim Elkhatib**[1], **Carolyn L. Smith**[2], **Anhadvir Singh**[1], **and Adriano Senatore**[1,*]

From the [1]*Department of Biology, University of Toronto Mississauga, Mississauga, Ontario, Canada;* [2]*NINDS, National Institutes of Health, Bethesda, Maryland, USA*

Edited by Mike Shipston

Ca_V1 and Ca_V2 voltage-gated calcium channels evolved from an ancestral $Ca_V1/2$ channel *via* gene duplication somewhere near the stem animal lineage. The divergence of these channel types led to distinguishing functional properties that are conserved among vertebrates and bilaterian invertebrates and contribute to their unique cellular roles. One key difference pertains to their regulation by calmodulin (CaM), wherein bilaterian Ca_V1 channels are uniquely subject to pronounced, buffer-resistant Ca^{2+}/CaM-dependent inactivation, permitting negative feedback regulation of calcium influx in response to local cytoplasmic Ca^{2+} rises. Early diverging, nonbilaterian invertebrates also possess Ca_V1 and Ca_V2 channels, but it is unclear whether they share these conserved functional features. The most divergent animals to possess both Ca_V1 and Ca_V2 channels are placozoans such as *Trichoplax adhaerens*, which separated from other animals over 600 million years ago shortly after their emergence. Hence, placozoans can provide important insights into the early evolution of Ca_V1 and Ca_V2 channels. Here, we build upon previous characterization of *Trichoplax* Ca_V channels by determining the cellular expression and ion-conducting properties of the Ca_V1 channel orthologue, TCa_V1. We show that TCa_V1 is expressed in neuroendocrine-like gland cells and contractile dorsal epithelial cells. *In vitro*, this channel conducts dihydropyridine-insensitive, high-voltage–activated Ca^{2+} currents with kinetics resembling those of rat $Ca_V1.2$ but with left-shifted voltage sensitivity for activation and inactivation. Interestingly, TCa_V1, but not TCa_V2, exhibits buffer-resistant Ca^{2+}/CaM-dependent inactivation, indicating that this functional divergence evolved prior to the emergence of bilaterian animals and may have contributed to their unique adaptation for cytoplasmic Ca^{2+} signaling within various cellular contexts.

Voltage-gated calcium (Ca_V) channels belong to a vast eukaryotic lineage of four-domain channels, which in animals includes voltage-gated sodium (Na_V) and NALCN sodium leak channels (1). These pore-forming proteins, also referred to as α_1 subunits, share a common transmembrane architecture of four homologous repeat domains (DI to DIV), each bearing six transmembrane alpha helices (Fig. 1*A*). In addition to opening with changes in membrane voltage, a key feature of Ca_V channels is their selective permeability for Ca^{2+}, which acts as a second messenger in the cytosol. Hence, Ca_V channels are able to translate electrical signals at the cell membrane into cytoplasmic Ca^{2+} signals, for example at the presynaptic terminal where they drive vesicle exocytosis and neurotransmitter release (*i.e.*, excitation-secretion coupling) and in muscle where they drive contraction (excitation-contraction coupling) (2).

Most animals possess three types of Ca_V channels that separate into two ancient and phylogenetically distinct clades: Ca_V3 or T-type channels, which become activated by small membrane depolarization and are classified as low-voltage–activated channels, and high-voltage–activated or HVA channels, which are further classified as Ca_V1 or L-type channels and Ca_V2 or N-, P/Q-, and R-type channels (3). Ca_V3 channels are present in the genomes of single-celled choanoflagellates, our closest unicellular ancestors, and hence likely evolved before the emergence of animals (4). Ca_V1 and Ca_V2 channels are thought to have evolved strictly in animals *via* gene duplication of an ancestral $Ca_V1/2$-type channel type, still present in choanoflagellates and poriferan animals (sponges) (4, 5). In accordance, Ca_V1, Ca_V2, and $Ca_V1/2$ channels share common structural features that distinguish them from Ca_V3 channels, including an alpha interaction domain (AID) in the cytoplasmic linker between DI and DII, where the obligate ancillary subunit $Ca_V\beta$ binds and regulates channel membrane expression and gating (1, 6). The association of the Ca_V1 and Ca_V2 channels with $Ca_V\beta$ was likely inherited from the ancestral $Ca_V1/2$ channel, given the presence of a $Ca_V\beta$ gene in choanoflagellates (4, 7) that can regulate mammalian $Ca_V1.2$ and $Ca_V2.3$ channels *in vitro* (8), and the unpublished observation that efficient *in vitro* expression of the $Ca_V1/2$ channel cloned from the choanoflagellate *Salpingoecca rosetta* requires co-expression with its cognate $Ca_V\beta$ subunit (9). Ca_V1 and Ca_V2 channels also require the ancillary subunit $Ca_V\alpha_2\delta$ for their membrane expression, localization, and gating characteristics, which in contrast to the cytoplasmic $Ca_V\beta$ subunit associates with extracellular regions of the pore-forming α_1

* For correspondence: Adriano Senatore, adriano.senatore@utoronto.ca.

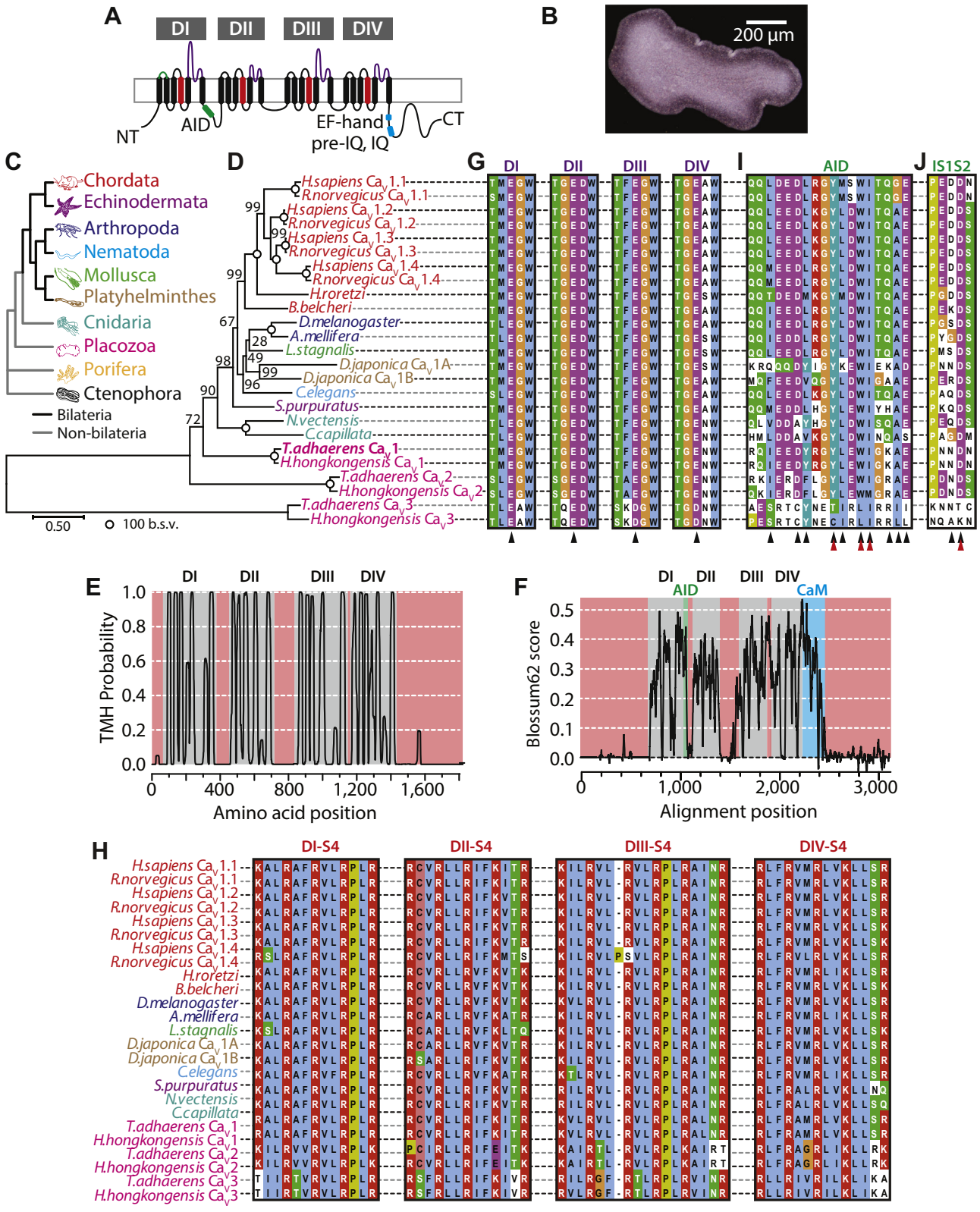

Figure 1. Conserved structural features of the *Trichoplax* Ca_V1 (TCa_V1) channel. *A*, illustration of the TCa_V1 channel membrane topology. Four sets of six transmembrane segments are arranged in four repeat domains (DI–DIV), connected to each other with extracellular and cytosolic loops/linkers respectively. The N terminus, C terminus, alpha interaction domain (AID), as well as C-terminal EF hand, pre-IQ, and IQ regions required for calmodulin-dependent regulation are indicated and color coded with respect to panels *F* to *J*. *B*, top-down micrograph of *Trichoplax adhaerens* reveals its small, asymmetrical body plan. *C*, cladogram depicting the proposed sister relationship of placozoans to bilaterians (*black lines*) and nonbilaterian invertebrates (*gray lines*). The colors are used to code for each phylum represented in panels *D* and *H*. *D*, maximum likelihood phylogenetic tree of representative full-length Ca_V1 channel protein sequences from major animal phyla, as well as Ca_V2 and Ca_V3 channels from the placozoans *Trichoplax adhaerens* and *Hoilungia hongkongensis*. Branch length scale bar on the *bottom left* corresponds to 0.5 substitutions per site, and nodes are labeled with bootstrap values for 1000 ultrafast replicates.

subunit (6). Whether this subunit also interacts with and regulates extant $Ca_V1/2$ channels is unclear, given its reported absence in the genomes of poriferans and choanoflagellates, the only organismal lineages known to possess $Ca_V1/2$ channels (4).

Also in accordance with their evolutionary relatedness, Ca_V1, Ca_V2, and $Ca_V1/2$ channels share C-terminal EF-hand, pre-IQ, and IQ domains/structures where the Ca^{2+} sensor protein calmodulin (CaM) binds and regulates channel gating. For Ca_V1 and Ca_V2 channels, Ca^{2+}/CaM regulation is an important feedback mechanism that permits fine tuning of cytoplasmic Ca^{2+} influx in response to background Ca^{2+} levels. Most often, Ca^{2+}/CaM regulation of Ca_V1 and Ca_V2 channels results in accelerated inactivation of macroscopic currents recorded under voltage-clamp (*i.e.*, Ca^{2+}-dependent inactivation or CDI), although vertebrate $Ca_V2.1$ channels can also exhibit Ca^{2+}-dependent facilitation (10). Importantly, CaM bears two Ca^{2+}-binding lobes (N and C terminal or N- and C-lobes), each with different Ca^{2+}-binding properties. Specifically, the N-lobe exhibits weaker Ca^{2+} binding affinity and thus senses slow, global rises in cytoplasmic Ca^{2+}, while the C-lobe has a much higher binding affinity, optimal for detecting transient local rises in Ca^{2+} emanating from the open channel pore (11). This difference in Ca^{2+} binding also permits experimental distinction between N- and C-lobe regulation, where N-lobe processes are disrupted by strong cytoplasmic Ca^{2+} buffering (*e.g.*, 10 mM BAPTA), while C-lobe processes are buffer-resistant. Under strong buffering conditions, C-lobe regulation can be subsequently identified by switching the permeating cation from Ca^{2+} to Ba^{2+}, the latter weakly binding CaM and hence unable to to triggering the CDI process (12).

In mammals, both Ca_V1 and Ca_V2 channels are subject to N-lobe regulation by CaM. However, $Ca_V1.2$ and $Ca_V1.3$ channels exhibit altered N-lobe modulation that is buffer resistant (*i.e.*, local sensitivity), caused by direct interactions between CaM and the channels' N termini, at structures referred to as NSCaTE (for N-terminal spatial Ca^{2+} transforming element) and NATE (for NSCaTE associated transduction element) (13, 14). Bilaterian (*i.e.*, animals with bilateral body symmetry) invertebrate Ca_V1 channels also possess an NSCaTE motif; however, unlike $Ca_V1.2$ and $Ca_V1.3$, removal of this motif *in vitro* does not impact CDI (15), suggesting that this altered N-lobe regulation is a unique feature of mammalian $Ca_V1.2$ and $Ca_V1.3$ channels. Additionally, mammalian Ca_V1 channels, but not Ca_V2 channels, are also subject to pronounced, buffer-resistant CDI that is mediated by the C-lobe of CaM (10). Thus, altogether, a key distinction in CaM regulation between mammalian Ca_V1 and Ca_V2 channels is that only Ca_V1 channels exhibit buffer-resistant regulation for sensing local Ca^{2+} plumes, in addition to global sensitivity that is also apparent for Ca_V2 channels. Importantly, a similar distinction has been reported for the Ca_V1 and Ca_V2 channel homologues from the snail *Lymnaea stagnalis*, where under strong buffering conditions, the Ca_V2 channel lacks CDI when the permeating cation is switched from Ba^{2+} to Ca^{2+}, while the Ca_V1 channel shows pronounced buffer-resistant CDI, that becomes apparent when Ca^{2+} is replaced with Ba^{2+} as the permeating cation (15, 16). Altogether, it is apparent that differential regulation of Ca_V1 and Ca_V2 channels by CaM is an ancestral trait that likely emerged hundreds of millions of years ago in last common ancestor of all bilaterians. However, the evolutionary origin of this distinction and whether it conserved in early diverging, nonbilaterian animals is not known.

The most early diverging animals to possess Ca_V1 and Ca_V2 channels, along with Ca_V3 channels, are species within the phylum Placozoa such as *Trichoplax adhaerens* (4, 5, 17). *Trichoplax* is a flat, disc-shaped marine invertebrate that lacks a neuromuscular system and synapses (Fig. 1*B*) and possess only six ultrastructurally distinguishable cell types (18). Despite their morphological simplicity, placozoans possess a large repertoire of genes associated with electrochemical signaling in the nervous system, which in addition to Ca_V channels, includes Na_V and voltage-gated K^+ channels (19, 20). Accordingly, placozoans produce action potentials (APs) (21), and it is likely that electrical and transient Ca^{2+} signaling play important roles in their biology. Having diverged from other animals over 600 MYA (22, 23), shortly after the emergence of Ca_V1 and Ca_V2 channels *via* gene duplication, placozoans can provide unique perspectives on the distinct evolutionary histories of Ca_V1 and Ca_V2 channels.

Previously, we determined the cellular expression and *in vitro* functional properties of the *T. adhaerens* Ca_V2 and Ca_V3 channel homologues (5, 24, 25). Here, we complete the characterization of the *Trichoplax* Ca_V channel set by similarly chracterizing the *Trichoplax* Ca_V1 channel, and describe the phylogenetic properties of the placozoan $Ca_V\beta$ and $Ca_V\alpha_2\delta$ and related subunit homologues. *Trichoplax* Ca_V1 (TCa_V1) is expressed in contractile epithelial cells located on the dorsal epithelium and neuroendocrine-like gland cells located along

E, Phobius (127) transmembrane helix probability plot of the TCa_V1 channel protein sequence. DI to DIV are back colored in *gray*, while the cytoplasmic N terminus, C terminus, and cytoplasmic linkers are back colored *red*. *F*, EMBOSS Plotcon (128) running window similarity plot of the TCa_V1 channel protein aligned with single representative Ca_V1 channels from each phylum included in panel *D*, revealing strong conservation within the transmembrane segments of DI to DIV (*gray*) and highly divergent cytoplasmic regions (*red*). The AID and calmodulin-interacting domains are highlighted in *green* and *blue*, respectively. *G*, amino acid sequence alignment of the selectivity filters from DI to DIV reveals a conserved four-glutamate selectivity filter P-loop motif (*i.e.*, EEEE, indicated by *black* chevrons), present in all Ca_V1 and Ca_V2 channels, whereas placozoan Ca_V3 channels resemble other Ca_V3 channels with aspartate residues in lieu of glutamate in domains DIII and DIV (*i.e.*, EEDD). Also conserved among all included calcium channels is an asparate residue adjacent to the DII selectivity filter glutamate, thought to contribute to Ca^{2+} selectivity. *H*, alignment of DI to DIV segment 4 (S4) helices that make up the voltage sensors. Positively charged lysine (K) and arginine (R) residues critical for voltage sensing are highlighted in *red*. *I*, protein alignment revealing conserved AIDs within the DI–DII cytoplasmic linkers of Ca_V1 and Ca_V2 channels, absent in Ca_V3 channels, which are required for interaction with the $Ca_V\beta$ ancillary subunit. The *black* chevrons denote amino acid positions that interface with the $Ca_V\beta$ protein, and *red* chevrons indicate amino acids positions considered most critical for the interaction (37, 38). *J*, alignment revealing a highly conserved aspartate in the DI S1–S2 extracellular loop of Ca_V1 and Ca_V2 channels that is essential for the interaction with the $Ca_V\alpha_2\delta_1$ ancillary subunit (39). CT, C terminus; NT, N terminus; TCa_V, *T. adhaerens* voltage-gated calcium channel; TMH, transmembrane helix.

the periphery of the animal. *In vitro* expression of the cloned channel is significantly increased upon co-expression with mammalian $Ca_V\beta_{1b}$ and $Ca_V\alpha_2\delta_1$ subunits, in lieu of co-expressed *Trichoplax* ancillary subunits. Whole-cell voltage-clamp recording of transfected mammalian cells revealed robust high-voltage–activated Ca^{2+} currents with left-shifted voltage dependencies compared to the rat $Ca_V1.2$ channel ($rCa_V1.2$), especially with respect to channel inactivation, producing a prominent window current at resting voltages between −50 and −30 mV. Interestingly, omission of a cotransfected $Ca_V\alpha_2\delta_1$ subunit resulted in significant rightward shifts in channel activation and inactivation, underscoring the significance of this subunit in regulating TCa_V1 channel gating. More similar to $rCa_V1.2$ is the recovery from inactivation and kinetics for current activation, inactivation, and deactivation. Altogether, the functional properties of the *Trichoplax* Ca_V1 channel are somewhat divergent compared to the mammalian $Ca_V1.2$ channel orthologue, in line with the extreme phylogenetic distance between placozoans and bilaterians.

Similar to our finding for *Trichoplax* Ca_V2 (5), TCa_V1 is insensitive to pharmacological blockers that are selective for mammalian orthologues, with minimal sensitivity to the dihydropyridine (DHP) blockers nifedipine, isradipine, and the two enantiomers of Bay K8644 which either block or enhance macroscopic currents. Considering the recent discovery of APs in the Placozoa, we compared the Ca^{2+} conducting properties of TCa_V1 and TCa_V2 using square voltage-clamp waveforms of different durations and frequencies, revealing similar Ca^{2+} currents under most tested conditions. Where the two channels were found to differ was in their regulation by CaM. Specifically, whereas both channels are subject to CDI mediated by CaM, only TCa_V1 exhibits modulation that is resistant to strong cytoplasmic Ca^{2+} buffering, evident when comparing inactivation properties when switching the permeating cation from Ca^{2+} to Ba^{2+}. Thus, like in bilaterians, the *Trichoplax* Ca_V1 and Ca_V2 channels are differentially regulated by CaM, with the Ca_V1 channel capable of detecting local Ca^{2+} plumes, a feature that likely impacted the differential selection of Ca_V1 channels for specific Ca^{2+} signaling functions in different cellular contexts.

Results

The Trichoplax Ca_V1 channel bears the distinctive structural features of high-voltage–activated Ca_V channels

T. adhaerens (Fig. 1*B*) is the most studied species from the phylum Placozoa (Fig. 1*C*), a group of simple seawater animals that have a phylogenetic sister clade relationship with bilaterians, and cnidarians (*e.g.*, jellyfish, sea anemones, and corals). Placozoans lack a nervous system and synapses, although they possess most genes required for electrochemical neural signaling (19). The two most early diverging animal phyla are the poriferans (sponges) and ctenophores (comb jellies), the former lacking a nervous system (26) and the latter bearing the most divergent nervous systems, proposed by some to have evolved independently (27). Both ctenophores and sponges lack Ca_V1 and Ca_V3 channels (4), making placozoans the most early diverging group to possess a complete set of Ca_V1 to Ca_V3 channels, as well as one ancillary $Ca_V\beta$ and two $Ca_V\alpha_2\delta$ orthologues (20). A maximum likelihood phylogenetic tree of representative full-length Ca_V channel protein sequences from select species reveals phylogenetic relationships for Ca_V1 channels that mostly match the species phylogeny (28), with the orthologues from *Trichoplax* and the fellow placozoan *Hoilungia hongkongensis* being the most divergent, followed by those from cnidarians (Fig. 1*D*). Like most invertebrates (*e.g.*, echinoderms, molluscs, nematodes, and most arthropods), placozoans possess single copy genes for Ca_V1 to Ca_V3 channels, whereas independent gene duplications produced multiple isotypes in certain lineages. For example, higher chordates possess four Ca_V1 channel isotypes ($Ca_V1.1$–$Ca_V1.4$), while more early diverging chordates such as tunicates (*e.g.*, the sea squirt *Halocynthia roretzi*) and cephalochordates (*e.g.*, the lancelet *Branchiostoma belcheri*) only have single Ca_V1 channel genes. Ca_V1 channels duplicated independently in Platyhelminthes (*e.g.*, the planarian *Dugesia japonica*) to produce two isotypes, Ca_V1A and Ca_V1B (29). After placozoans, the next most early diverging animals to possess Ca_V1 to Ca_V3 channels are the cnidarians such as the starlet sea anemone *Nematostella vectensis* and the lion's mane jellyfish *Cyanea capillata*, which notably duplicated Ca_V2 and Ca_V3 channels to produce three and two genes respectively, while retaining a single Ca_V1 channel gene (4, 5, 30, 31).

The open reading frame of the TCa_V1 α_1 subunit was cloned from a whole animal cDNA library, producing a consensus sequence encoding a 1822 amino acid protein with a predicted molecular weight of ∼208 kDa (GenBank accession number MW915585). When comparing the three *Trichoplax* Ca_V channels to each other, the more proximal phylogenetic relationship between TCa_V1 and TCa_V2 is apparent as they share ∼41% sequence identity on a global protein alignment, compared to only 29% and 26%, respectively, with the TCa_V3 channel. TCa_V1 is also more similar to rat $Ca_V1.2$ than it is to TCa_V2 and TCa_V3, with 49% sequence identity. Structurally, the TCa_V1 channel bears the hallmark features of bilaterian and cnidarian Ca_V1 and Ca_V2 channels (Fig. 1*A*), including four homologous repeat domains (domains I to IV), each bearing six predicted transmembrane alpha helices or segments (S1–S6) (Fig. 1*E*). Alignment of single representative Ca_V1 channel protein sequences from each phylum included in Figure 1*D* reveals that the transmembrane segments and intervening loops within the four repeat domains are highly conserved, while the N and C termini and cytoplasmic linkers between domains I to IV are highly divergent (Fig. 1*F*). Sequence conservation within domains I to IV includes four glutamate (E) residues within the extracellular pore-loop (P-loop) of each domain, located between S5 and S6, that form a Ca^{2+} selectivity filter motif of EEEE common to Ca_V1 and Ca_V2 channels (Fig. 1*G*). In contrast, and conserved in placozoans, Ca_V3 channels bear distinct selectivity filter motifs of two glutamate and two aspartate (D) residues (*i.e.*, EEDD; Figs. 1*G* and S1). Notably, all three placozoan Ca_V channels possess a ubiquitously conserved aspartate residue adjacent to

the DII selectivity filter glutamate (Fig. 1*G*), suggested to contribute to Ca^{2+} selectivity (32) but a reduced number of negatively charged amino acids four positions downstream of each selectivity filter residue which are thought to secondarily contribute (Fig. S1) (33, 34). There is also strong conservation of repeating positively charged arginine (R) and lysine (K) residues within the S4 helices of all Ca_V channels (Figs. 1*H* and S1), key for voltage sensing (35). Notable is the deep conservation of proline (P) residues within DI and DIV S4 helices, important for the contribution of these segments to channel gating (36), and a lysine to glutamate substitution in the DII S4 helix of placozoan Ca_V2 channels, a unique feature that likely affects the local electrostatic environment due a switch in polarity and perhaps impacts gating.

An exception to the highly divergent cytoplasmic regions of Ca_V1 channels across phyla is the AID located between DI and DII (Figs. 1, *A*, *I*, *F* and S1), where the ancillary subunit $Ca_V\beta$ binds and regulates Ca_V1 and Ca_V2 channel membrane expression and gating. Within the AID is a highly conserved amino acid motif of tyrosine-X-X-tryptophan-isoleucine (YXXWI) which is critical for interactions with $Ca_V\beta$ (37, 38), also found in placozoan Ca_V1 and Ca_V2 channels, the *S. rosetta* $Ca_V1/2$ channel, but not Ca_V3 channels which lack an AID structure (Figs. 1*I* and S1). Placozoan Ca_V1 and Ca_V2 channels also bear a conserved, negatively charged aspartate residue in the extracellular DI S1–S2 loop (Fig. 1*J*), identified as a critical determinant for the interaction between the $Ca_V1.2$ α_1 subunit and the ancillary subunit $Ca_V\alpha_2\delta_1$ (39). Lastly, we note deep conservation of C-terminal structures adjacent to DIV S6, named the EF-hand, pre-IQ, and IQ domains (Fig. 1, *A* and *F*), also present in *S. rosetta* $Ca_V1/2$ (Fig. S1), which are absent in Ca_V3 channels and are binding loci for the Ca^{2+} sensor protein CaM (discussed later).

Phylogenetic and primary sequence properties of the placozoan $Ca_V\beta$ and $Ca_V\alpha_2\delta$ ancillary subunits

Previously, *T. adhaerens* was reported to possess single $Ca_V\beta$ and $Ca_V\alpha_2\delta$ subunit homologues (4). Here, we sought to update these findings by searching for sequences within recently improved gene datasets for *Trichoplax* (20, 40), as well as *H. hongkongensis* (41). In accordance with the previous report, we identified single $Ca_V\beta$ protein sequences for each placozoan, both bearing predicted tandem SRC homology 3 (SH3) and guanylate kinase (GK) domains (Figs. 2*A* and S2 and File S1), a hallmark feature of the $Ca_V\beta$ subunit and other members of the membrane-associated guanylate kinase family (42). In accordance with the species phylogeny, the placozoan $Ca_V\beta$ subunits form a sister clade relationship with homologues from cnidarians and bilaterians on a phylogenetic tree (Fig. 2*A*). An exception is the highly divergent homologue from *Caenorhabditis elegans*, dubbed CCB-2, which lacks a predicted GK domain and *in vivo*, does not appear to regulate Ca_V channel α_1 subunit function (43).

Global alignment of the *Trichoplax* $Ca_V\beta$ ($TCa_V\beta$) protein sequence with that of the rat $Ca_V\beta_1$ to $Ca_V\beta_4$ subunits, and the functionally characterized homologues from the snail *L. stagnalis* (7) and *S. rosetta* (8), reveals strong sequence conservation within the SH3 and GK domains, including key residues within the GK domain that mediate interactions with the $Ca_V\alpha1$ AID structure (38) (Fig. S2). This includes an "MLHKAL" motif, similar to the "LMQRAL" sequence of *S. rosetta* $Ca_V\beta$ shown to be essential for the ability of this divergent subunit to regulate mammalian $Ca_V2.3$ channels *in vitro* (8). Consistent with the phylogenetic relationships, the *Trichoplax* $Ca_V\beta$ is more similar to homologues from the rat and *Lymnaea* compared to *S. rosetta*, sharing between 41.0 and 43.4% amino acid sequence identity on a multiple alignment (Fig. 2*B*). $TCa_V\beta$ also more resembles the rat and *Lymnaea* subunits in bearing an extended N terminus upstream of the SH3 domain, but more resembles the *S. rosetta* homologue with its shorter C terminus downstream of the GK domain (Fig. S2). Interestingly, $TCa_V\beta$ as well as the *Lymnaea* and *S. rosetta* homologues resemble rat $Ca_V\beta_2$ in possessing large sequence inserts within the HOOK region that interrupt the SH3 domain structure, compared to the much shorter inserts found in rat $Ca_V\beta_1$ to $Ca_V\beta_3$ subunits (Fig. S2). This is significant because this unique feature of the mammalian $Ca_V\beta_2$ subunit imposes a significant rightward shift in the inactivation properties of calcium channels (44, 45), and as such, $TCa_V\beta$ might also exert such effects on $Ca_V\alpha_1$ subunits.

In contrast to the single $Ca_V\beta$ subunit, we identified 4 $\alpha_2\delta$ and related proteins for *Trichoplax* and *Hoilungia*, two of which form a strongly supported clade with bona fide $\alpha_2\delta$ subunits from bilaterians and cnidarians (Fig. 2*C*). Because of their proximity to each other on the phylogenetic tree, the set of *Trichoplax* and *Hoilungia* $\alpha_2\delta$ homologues likely duplicated from a single parent gene uniquely within the Placozoa, similar to the independent duplication apparent for arthropods which gave rise to three subunits (*i.e.*, *Drosophila melanogaster* and *Apis mellifera* straightjacket, Ma2/d, and CG4587 homologues). Notably, all invertebrate animals included in the analysis possess two $\alpha_2\delta$ homologues, while mammals possess four (*e.g.*, rat $\alpha_2\delta_1$ to $\alpha_2\delta_4$), with unclear phylogenetic relationships because of low node support values distributed within the $\alpha_2\delta$ clade. Also with strong node support, *Trichoplax* and *Hoilungia* each possess single CACHD1 homologues, shown in vertebrates to interact with and regulate Ca_V3 channels (46, 47), as well as a single protein falling within an undescribed clade of $\alpha_2\delta$-like homologues, also apparent in *L. stagnalis*, *N. vectensis*, and *S. rosetta* (Fig. 2*C*). Domain prediction analysis reveals that most $\alpha_2\delta$ and related proteins share a conserved N-terminal signal peptide, von Willebrand A-N (vWA-N) and vWA-A motifs, a calcium channel and chemotaxis receptors (Cache) domain (also known as Per-Arnt-Sim or PAS domains), and a C-terminal transmembrane helix. Most homologues also possess a conserved divalent cation binding site, called a metal-ion–dependent adhesion site (MIDAS), within the vWA-A domain (Figs. 2*C* and S3), consisting of five polar/charged amino acids that likely binds Mg^{2+} or Ca^{2+} in the endoplasmic reticulum to regulate trafficking of the α_1 subunit to the cell membrane (48).

A global protein alignment of the two *Trichoplax* $\alpha_2\delta$ subunits with rat $\alpha_2\delta_1$ to $\alpha_2\delta_4$ homologues reveals conservation of

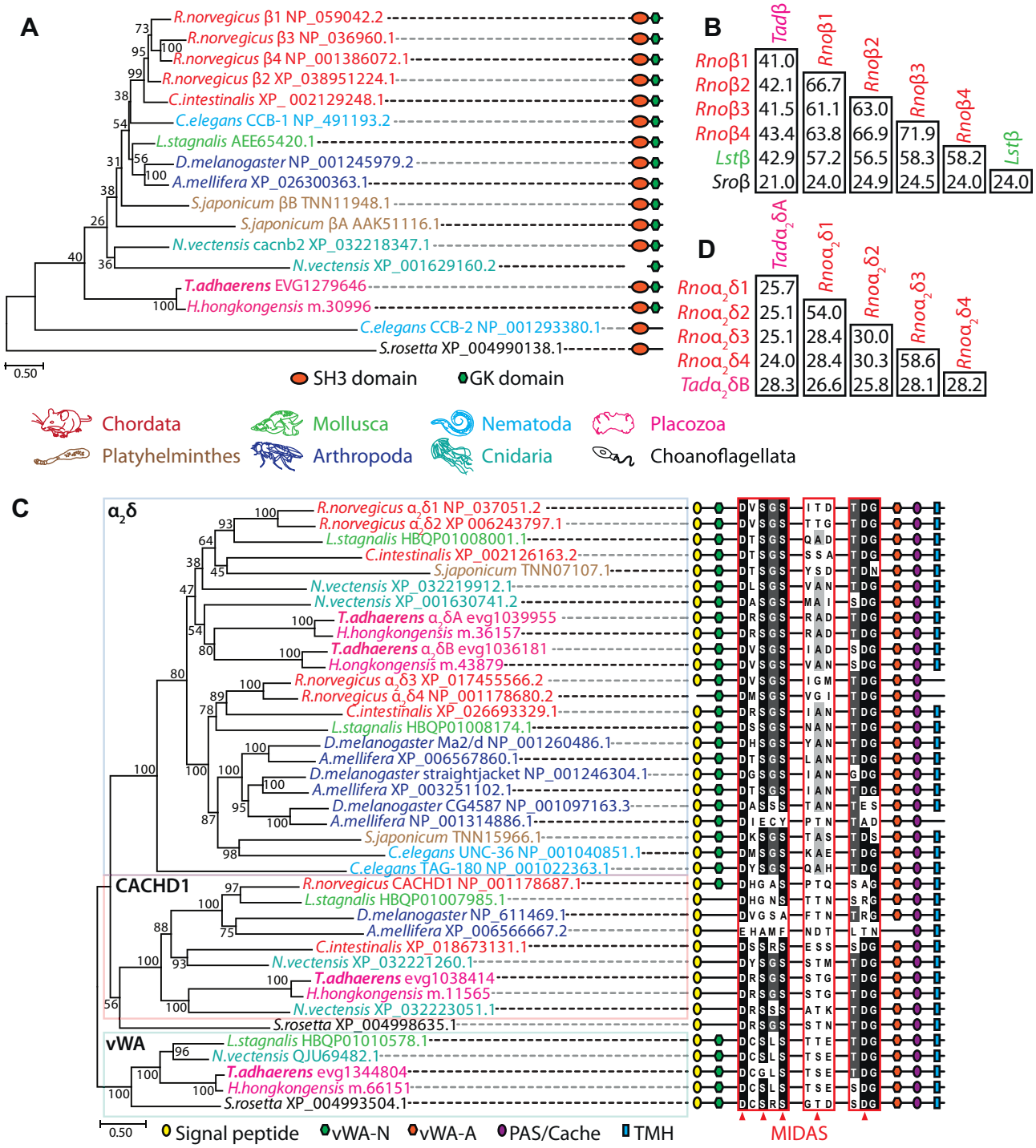

Figure 2. Phylogenetic properties of the *Trichoplax adhaerens* $Ca_V\beta$ and $Ca_V\alpha_2\delta$ subunits. *A*, maximum likelihood protein phylogeny of select $Ca_V\beta$ ancillary subunits from select species, rooted on the homologue from the choanoflagellate species *Salpingoeca rosetta*, revealing that single homologues from the placozoan species *Trichoplax adhaerens* and *Hoilungia hongkongensis* placozoans form a sister clade relationship with most metazoan homologues, except the highly divergent *C.elegans* homologue CCB-2. The *symbols* on the *right* of the phylogenetic tree depict successful prediction of SH3 and guanylate kinase (GK) domains using the structure prediction software InterProScan (129). Bootstrap node support values for 1000 ultrafast replicates are also presented on the phylogenetic tree, as well as the tree presented in panel *C*. *B*, sequence identity matrix for a global alignment of the *Trichoplax adhaerens* $Ca_V\beta$ protein sequence (*Tad*β) with *Rattus norvegicus* $Ca_V\beta1$–4 (*Rno*β1–4), *Lymnaea stagnalis* $Ca_V\beta$ (*Lst*β), and *Salpingoeca rosetta* $Ca_V\beta$ (*Sro*β). *C*, maximum likelihood protein phylogeny of $\alpha_2\delta$ and related proteins from select species, revealing that placozoans possess two $\alpha_2\delta$ homologues, a single CACHD1 homologue, as well as a single $\alpha_2\delta$-like protein from a clade of homologues with similar primary structures as the $\alpha_2\delta$ subunit, including predicted von Wildebrand Factor type A (vWA) domains. The *symbols* on the *right* of the phylogenetic tree depict successful prediction of N-terminal signal peptides, vWA-N and vWA-A domains, PAS/cache domains, and C-terminal transmembrane helices using InterProScan (129). Also included are sequence alignments of the conserved metal ion-dependent adhesion site important for regulation of Ca_V1 and Ca_V2 channel α_1 subunits. For panels *A* and *C*, the color coding of text refers to the different animal phyla as indicated in the legend located between the panels, and NCBI accession numbers for all sequence are included, with the exception of the placozoan homologues that were extracted from corresponding genome/transcriptome datasets (20, 41). *D*, sequence identity matrix for a global alignment of the *Trichoplax adhaerens* $Ca_V\alpha_2\delta$ protein sequences (*Tad*$\alpha_2\delta$A and *Tad*$\alpha_2\delta$B) with *Rattus norvegicus* $Ca_V\alpha_2\delta1$–4 (*Rno*$\alpha_2\delta1$–4). Cache; Calcium channel chemotaxis receptors; MIDAS, metal ion-dependent adhesion site; PAS, Per-Arnt-Sim; TMHs, transmembrane helices.

a C-terminal cysteine residue just upstream of the predicted transmembrane helix (Fig. S3), which in the mammalian subunits is posttranslationally modified to form a glycosylphosphatidylinositol anchor that tethers the subunit to the outer leaflet of the cell membrane (49). Interestingly, the two *Trichoplax* subunits share only 28.3% sequence identity with each other, which is similar to the divergence between the two clades of rat homologues (*i.e.*, $\alpha_2\delta_1/\alpha_2\delta_2$ *versus* $\alpha_2\delta_3/\alpha_2\delta_4$; Fig. 2*D*). Furthermore, the *Trichoplax* $\alpha_2\delta$B subunit is slightly more similar to the rat homologues than $\alpha_2\delta$A, sharing between 25.8 and 28.2% sequence identity, compared to 24.0 to 25.1%.

TCa_V1 expresses in vitro *and is expressed in Trichoplax dorsal epithelial and type II gland cells*

With the intention of expressing the TCa_V1 channel in human embryonic kidney cell (HEK)-293T cells for electrophysiological characterization, we synthesized the channel cDNA with codon optimization for enhanced expression in human cells. This cDNA was cloned into two mammalian expression vectors: pIRES2-EGFP and pEGFP-C1. This produced the vectors pTCa$_V$1-IR-EGFP and pEGFP-TCa$_V$1 (Fig. 3*A*), the former allowing bicistronic expression of the TCa$_V$1 channel protein separately from enhanced green fluorescent protein (EGFP) and the latter producing a fusion protein of TCa$_V$1 with EGFP at its N terminus. A qualitative Western blot of HEK-293T cell lysates after transfection with the pEGFP-TCa$_V$1 vector, using anti-GFP antibodies, produced a band of ∼250 kDa that roughly corresponds to the sum molecular weights of the TCa$_V$1 channel (207.6 kDa) plus EGFP (28.9 kDa; Fig. 3*B*). This band was absent in untransfected cells but can be observed in all lanes that contain pEGFP-TCa$_V$1. Furthermore, the bands appear to increase in intensity upon cotransfection with the rat $Ca_V\beta_{1b}$ and $Ca_V\alpha_2\delta_1$ ancillary subunits, consistent with previous reports that these mammalian subunits can be efficiently used for expressing invertebrate Ca$_V$1 and Ca$_V$2 channels *in vitro* (50–52). To ensure equal protein loading, we performed Ponceau staining of the Western blot membrane, revealing similar protein levels for all samples (Fig. 3*B*). The observed effect of $Ca_V\beta_{1b}$ and $Ca_V\alpha_2\delta_1$ co-expression on TCa$_V$1 abundance resembles our previous observations for the cloned *Trichoplax* Ca$_V$2 and Ca$_V$3 channels, whose expression also significantly increased upon co-expression with the two rat ancillary subunits, most markedly for TCa$_V$3 (5, 24). To quantify the effect of the subunits on pEGFP-TCa$_V$1 abundance, EGFP fluorescence intensity of HEK-293T cells transfected with the pEGFP-TCa$_V$1 vector was examined and showed an additive increase upon cotransfection with the rat $Ca_V\beta_{1b}$ and $Ca_V\alpha_2\delta_1$ subunit cDNAs ($p \leq 0.021$ with a Holm–Sidak test after one-way ANOVA; $p < 0.001$, F = 46.0; Table S1). The $Ca_V\beta_{1b}$ and $Ca_V\alpha_2\delta_1$ subunits increased fluorescence intensity when cotransfected separately, but cotransfection with both subunit cDNAs produced the greatest EGFP-TCa$_V$1 expression, with the pattern: no subunits < $Ca_V\alpha_2\delta_1 \leq Ca_V\beta_{1b} < Ca_V\beta_{1b}$ plus $Ca_V\alpha_2\delta_1$ (Fig. 3, *C* and *D*). This increase in fluorescence was not due to changes in cell confluency between the different conditions (untransfected = 70 ± 2%; pEGFP-TCa$_V$1 = 65 ± 4%; pEGFP-TCa$_V$1 + $\alpha_2\delta_1$ = 68 ± 3%; pEGFP-TCa$_V$1 + β_{1b} = 68 ± 1%; pEGFP-TCa$_V$1 + $\alpha_2\delta_1$+ β_{1b} = 68 ± 4%; one-way ANOVA p = 0.484). Thus, similar to other high-voltage–activated Ca$_V$ channels, TCa$_V$1 expression *in vitro* significantly increased upon co-expression with Ca$_V\beta$ and Ca$_V\alpha_2\delta$ ancillary subunits (53), presumably through conserved interactions with the AID and DI S1–S2 loop, respectively (Fig. 1, *I* and *J*). Of note, we made efforts to characterize the *in vitro* properties of the *Trichoplax* Ca$_V\beta$ subunit but were unable to detect the ectopically expressed protein on Western blots *via* a hemagglutinin tag (not shown). As such, analysis of the functional properties of the *Trichoplax* ancillary subunits will be presented in a future study, using codon optimization which has been shown to significantly improve ectopic expression of *Trichoplax* genes in mammalian cells (54).

To enable studying the untagged TCa$_V$1 protein, we generated rabbit polyclonal antibodies against a 121 amino acid recombinant peptide corresponding to the II-III linker (residues 730–850 of accession MW915585). These antibodies could detect a band corresponding to the untagged TCa$_V$1 channel protein in Western blots of HEK-293T cell protein lysates after transfection with the pTCa$_V$1-IR-EGFP vector, as well as a heavier band that did not migrate with the protein ladder (Fig. 3*E*). Both bands were absent in blots of untransfected cells (not shown). The specificity of the antibodies against the TCa$_V$1 channel epitope was confirmed by preadsorption of the antibodies with excess recombinant II-II linker peptide, which caused both bands to disappear (Fig. 3*E*). Altogether, these data indicate that the TCa$_V$1 channel is expressed as a full-length protein in HEK-293T cells and that a subset may be bound to other proteins, increasing its molecular weight.

The same polyclonal antibodies were then used to detect TCa$_V$1 in *Trichoplax* whole animal protein lysates. Like the TCa$_V$2 channel, the TCa$_V$1 channel is present as an endogenous full-length protein but is also fragmented within the lysates (5). Here, anti-TCa$_V$1 antibodies labeled bands at ∼90 and 260 kDa that disappeared with peptide preincubation, as well as a heavy molecular weight band that did not (Fig. 3*F*). The antibodies raised against the channel are specific to the II-III linker epitope sequence, and based on Basic Local Alignment Search Tool (BLAST) analysis of the *Trichoplax* genome and whole animal mRNA transcriptome (19, 20), they are unlikely to bind off target proteins in *Trichoplax* since the epitope does not produce significant alignments other than TCa$_V$1. Thus, the heavy molecular weight band likely represents off-target binding by other antibodies present within the rabbit serum. The smaller 90 kDa band on the other hand is specifically targeted by the TCa$_V$1 antibodies and may represent an endogenously expressed truncated variant of the channel, akin to Ca$_V$1.2 channels in the mammalian brain that become proteolytically cleaved at the DII-DIII linker, as a form of age-related regulation of channel activity (55). Overall, endogenous expression of TCa$_V$1 is apparent, indicating an active role for the calcium channel in *Trichoplax*.

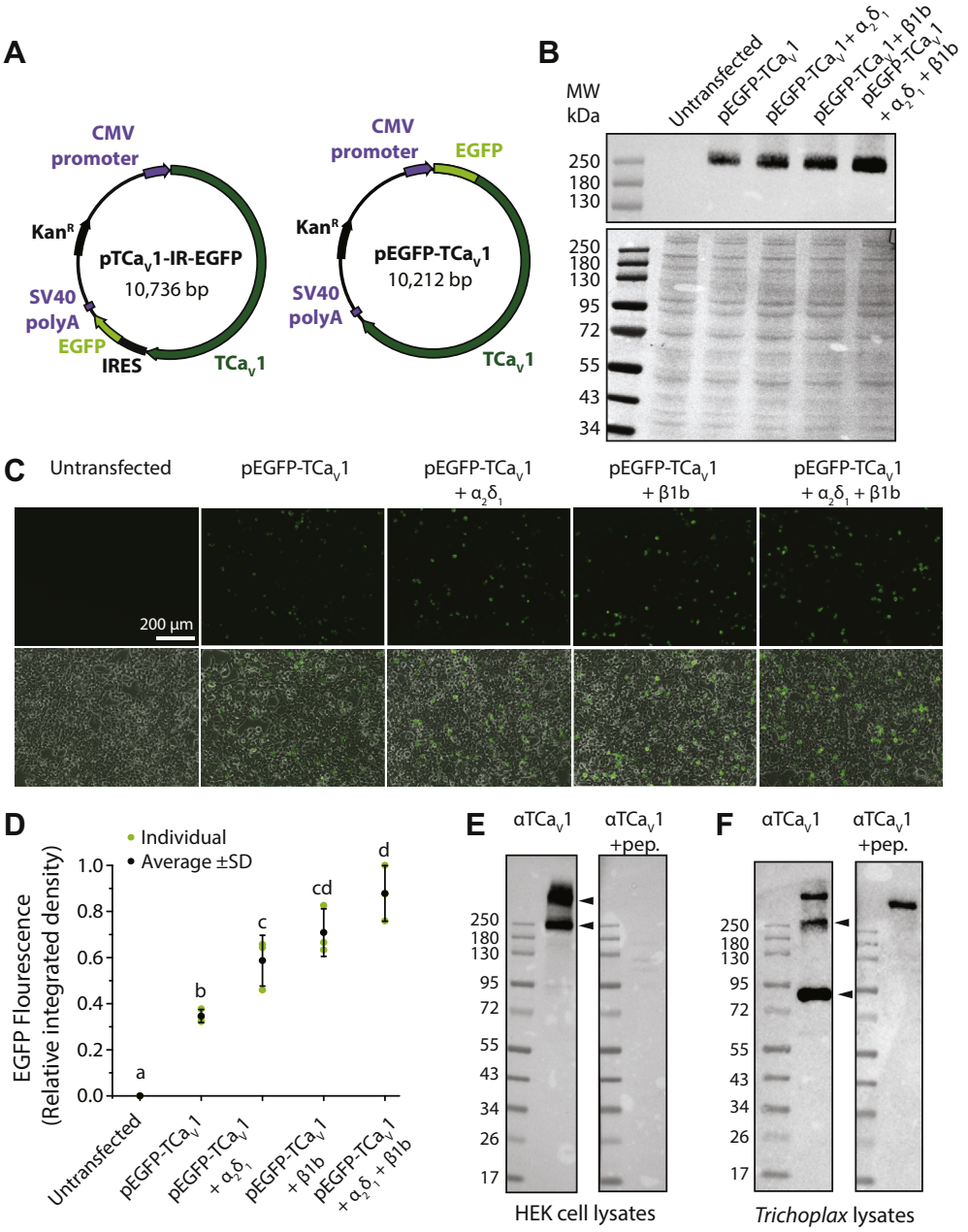

Figure 3. Expression of the TCa_V1 protein *in vitro* and *in vivo*. *A*, illustration of the pTCaV1-IR-EGFP and pEGFP-TCaV1 plasmid vectors for heterologous expression of the TCaV1 channel protein in human embryonic kidney (HEK)-293T cells. The pTCaV1-IR-EGFP vector permits bicistronic expression of TCaV1 and EGFP, whereas the pEGFP-TCaV1 vector fuses EGFP with the N terminus of TCaV1. *B*, *top*, qualitative Western blot of protein lysates from HEK-293T cells transfected with pEGFP-TCaV1 and various combinations of rat $Ca_V\beta_{1b}$ and $Ca_V\alpha_2\delta_1$ ancillary subunits. Monoclonal anti-GFP antibodies reveal a band of ~250 kDa, corresponding to the predicted molecular weight of ~237 kDa for the full-length EGFP-TCaV1 fusion protein, which is absent from untransfected cells. The combination of both subunits appears to show the greatest intensity. *Bottom*, Ponceau stain of above Western blot showing equal protein content in each lane. *C*, fluorescence (*top*) and overlaid fluorescence and transmitted light images (*bottom*) of cultured HEK-293T cells transfected with pEGFP-TCaV1 with various combinations of accessory subunits. Intensity of the EGFP-TCaV1 fusion protein fluorescence increased upon cotransfection with the rat $Ca_V\beta_{1b}$ and $Ca_V\alpha_2\delta_1$ ancillary subunits. *D*, plot of average EGFP fluorescence intensity ±S.D. (error bars) in micrographs of separately transfected HEK-293T cells (n = 3). Cotransfection of cells with both rat $Ca_V\beta_{1b}$ and $Ca_V\alpha_2\delta_1$ ancillary subunits resulted in the greatest fluorescence intensity. Integrated density values were standardized to the maximal value across all experiments. *Lower case letters* denote significant differences ($p \leq 0.021$) in integrated density as determined by a Holm-Sidak test (Table S1). *E*, Western blot of HEK-293T protein lysates expressing untagged TCaV1 protein from the pTCaV1-IR-EGFP vector. Custom rabbit polyclonal anti-TCaV1 antibodies (directed against 121 amino acids within the TCaV1 channel II–III linker) reveals strong ectopic expression of the TCaV1 channel when co-expressed with the rat $Ca_V\beta_{1b}$ and $Ca_V\alpha_2\delta_1$ subunits. Two bands are visible on the blots, one at ~250 kDa and a heavier band that did not migrate with the protein ladder, that disappeared after preadsorption of the anti-TCaV1 antibodies with recombinant peptide used to generate the antibodies (+pep.). *F*, Western blot of *Trichoplax* whole-animal protein lysates using the anti-TCaV1 polyclonal antibodies revealed three bands. A heavy molecular weight band that did not disappear with peptide preincubation and two bands with molecular masses of ~90 and 260 kDa that did. EGFP, enhanced green fluorescent protein; TCa_V, *T. adhaerens* voltage-gated calcium channel.

To examine the localization of the TCa_V1 channel in *Trichoplax*, we performed whole-mount immunohistochemistry on fixed animals. The TCa_V1 antibodies labeled two cell types: one along the outer edge that co-labeled with the cell-type marker wheat germ agglutinin (WGA) consistent with mucous secreting type II gland cells (56) and another more centrally, in a region dubbed the lipophil zone where digestive lipophil cells are expressed along the ventral/lower epithelium (Fig. 4, *A–C*) (56). Preadsorption of the TCa_V1 antibodies with the II-III linker antigen caused the prominent fluorescence signal in the lipophil zone to completely disappear, whereas labeling of the type II gland cells was diminished but not abolished (Fig. 4*D*). Possibly, this residual nonspecific labeling corresponds to the large molecular weight protein that persisted on Western blots in the antibody preadsorption experiments (Fig. 3*F*). Thus, although the antibodies provide strong evidence for expression of TCa_V1 within the lipophil zone, expression in gland cells was less conclusive. Three-dimensional reconstruction of the micrograph shown in Figure 4*C* reveals that TCa_V1 is restricted mostly to the dorsal epithelium (Fig. 4, *E–G*), a region with cells that exhibit ultrafast contractions upon cytoplasmic Ca^{2+} influx (57). A single-cell transcriptome of *Trichoplax* also documented expression of TCa_V1 in epithelial cells (metacell number 35) (58). This contrasts with the TCa_V2 and TCa_V3 channels, which we previously found to be expressed in gland cells (TCa_V2 and TCa_V3), but not within the dorsal or ventral epithelia (5, 24),

The prospect that type II gland cells might resemble neuroendocrine cells in their co-expression of Ca_V1 to Ca_V3 channels (59) prompted us to explore co-expression of TCa_V1 to TCa_V3 mRNAs in this cell type *via* fluorescence *in situ* hybridization (FISH; Fig. 3, *H–M*). Co-labeling with RNAscope probes complementary to the TCa_V1 and TCa_V2 mRNAs, and a fluorescent WGA probe (Fig. 4*H*), revealed enriched expression of TCa_V1 and TCa_V2 along the outer edge of *Trichoplax*, in regions harboring WGA-positive type II gland cells, as well as regions toward the interior (Fig. 4, *I–K*). We also performed FISH on dissociated *Trichoplax* cells, separately revealing expression of TCa_V1 and TCa_V2 in WGA-positive cells (Fig. 4, *L* and *M*). These data are consistent with our previous immunolocalization of the TCa_V2 channel within type II gland cells (5), as well as the apparent immunolocalization of TCa_V1 within these cells as noted above. Previously, immunolabeling experiments suggested that the TCa_V2 channel is weakly expressed in fiber cells, which are located between the dorsal and ventral epithelia (5). We therefore co-labeled dissociated *Trichoplax* cells with RNAscope probes for the fiber cell marker FoxC (60), revealing an absence of labeling for TCa_V1 (Fig. 4*L*) but weak labeling for TCa_V2 in a subset of fiber cells (Fig. 4*M*). Expression of TCa_V1 and TCa_V2 mRNA was also observed in subsets of dorsal and ventral epithelial cells (Fig. 4, *L* and *M*). Lastly, in a separate set of FISH experiments on dissociated cells, we found that 57 ± 6.7% of dissociated type II gland cells (±standard deviation or SD) co-express all three TCa_V channels (n = 99) and that 96.9 ± 3.1% express at least one of the three Ca_V channel mRNAs.

TCa_V1 conducts high voltage–activated Ca^{2+} currents with large window currents in vitro

To determine whether the recombinant TCa_V1 channel could produce functional voltage-dependent calcium currents *in vitro*, we performed whole-cell patch voltage clamp recording of HEK-293T cells transfected with the pTCa$_V$1-IRES-EGFP plus pMT2 vectors for co-expressing the rat $Ca_V\beta_{1b}$ and $Ca_V\alpha_2\delta_1$ ancillary subunits (61). Early in our experiments, we found that the transfected cells were generally unhealthy, and although we could record voltage-gated Ca^{2+} currents, these were quite small in amplitude. Based on preliminary analysis of the voltage properties of TCa_V1, we noted large window currents and reasoned that constitutive Ca^{2+} influx was being toxic to the cells (detailed below). Hence, we included in our transfections a pcDNA3.1 plasmid expressing the mouse Kir2.1 inward rectifying potassium channel (*i.e.*, pKir2.1-cDNA3) (62), to hyperpolarize the resting membrane potential below the TCa_V1 window current (63). This approach greatly enhanced our ability to record TCa_V1 currents *in vitro*, and hence, the Kir2.1 construct was cotransfected in all subsequent electrophysiological experiments.

Depolarizing voltage steps from −100 mV to between −80 mV and +90 mV with an external recording solution containing 3 mM Ca^{2+} revealed inward Ca^{2+} currents that resemble T-type/Ca_V3 channels in their crossing over during the inactivation phase (Fig. 5*A*), indicative of accelerated channel inactivation upon stronger membrane depolarization. A normalized average current–voltage plot of the TCa_V1 currents revealed a peak inward current at 0 mV, which is more depolarized than TCa_V2 and TCa_V3 with respective peak currents at −10 and −45 mV (Figs. S5*B*, S4*A* and Table 1). To compare the properties of TCa_V1 with a well-studied vertebrate Ca_V1 channel homologue, we conducted parallel experiments with rat $Ca_V1.2$ ($rCa_V1.2$) cotransfected with the same constructs and using the same recording solutions. Under these experimental conditions, the rat channel produced maximal inward currents at 5 mV, revealing a difference in current onset where the TCa_V1 channel begins activating at more negative voltages.

To remove the effect of driving force and visualize the macroscopic conductance of the channel population in response to depolarization, peak inward Ca^{2+} currents were transformed into conductance values using Ohm's law and fit with the Boltzmann function. This revealed that TCa_V1 is half-maximally activated ($V_{1/2}$) at −27.9 ± 1.99 mV compared to −11.0 ± 1.28 mV for $rCa_V1.2$ (Fig. 5*D*). The rates of activation of TCa_V1 and $rCa_V1.2$ in response to depolarization, represented by the conductance slope factor (k_{act}), were 8.40 ± 0.88 and 5.08 ± 0.67 mV, respectively. Both the 16.9 mV difference in $V_{1/2}$ values and the 3.32 mV difference in slope factors were significantly different between these two channels ($p < 0.001$, two-tailed t test). Thus, in addition to a

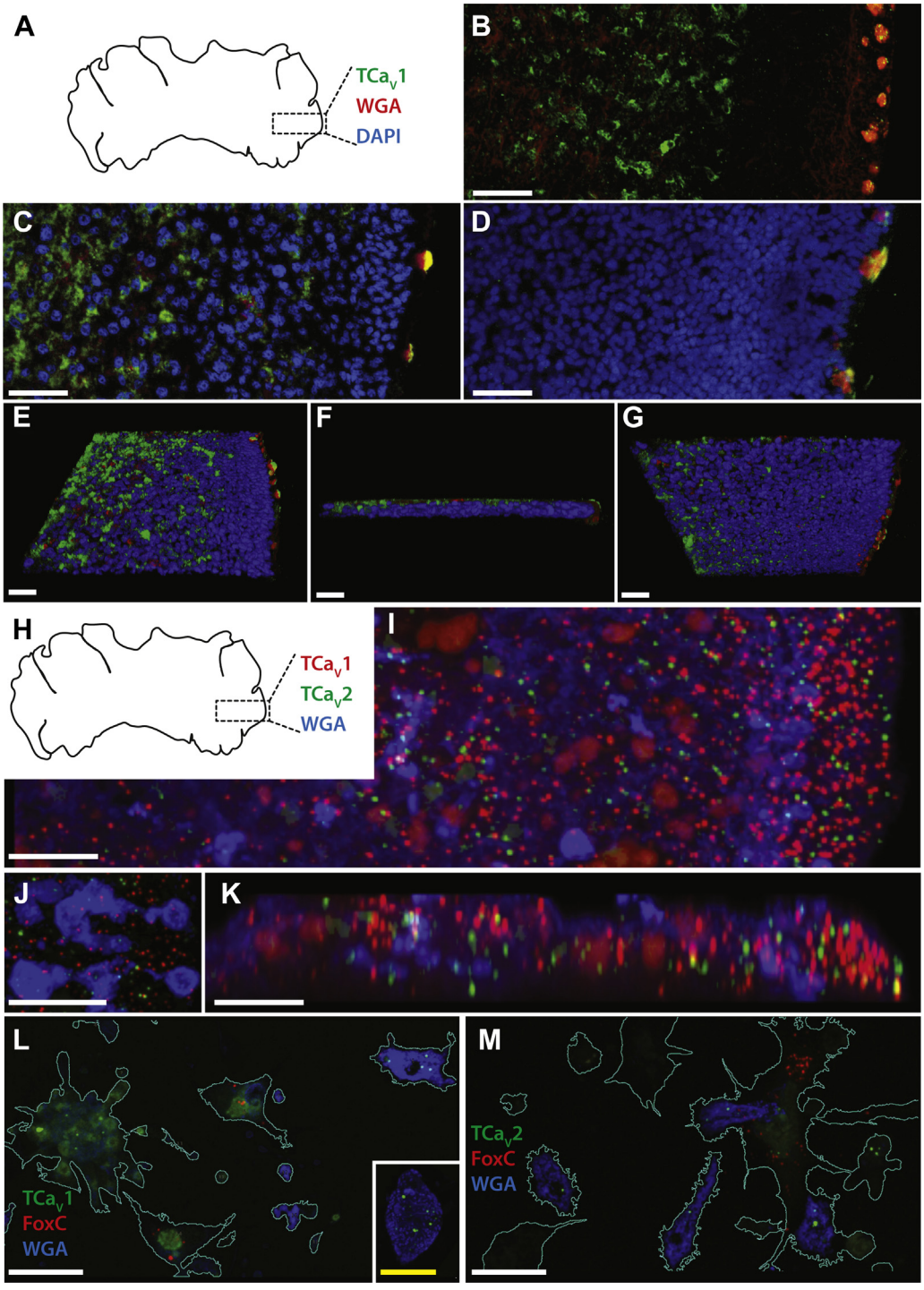

Figure 4. TCa_V1 channels are expressed in dorsal cells within the central region and type II gland cells along the periphery of *Trichoplax*. *A*, illustration of the dorsal view of *Trichoplax adhaerens*, indicating the relative area of animals imaged in panels *B–G*. Whole mount immunostaining using the rabbit anti-TCa_V1 polyclonal antibody is in *green*, Type II gland cells stained using fluorophore-conjugated wheat germ agglutinin (WGA) are in *red*, and nuclei stained with DAPI are in *blue*. *B*, Z-projection fluorescence micrograph of a *Trichoplax* animal labeled with anti-TCa_V1 and WGA reveals expression of the channel toward the center of the animal and in type II gland cells located along the periphery. *C*, fluorescence micrograph of a separate *Trichoplax* animal labeled with anti-TCa_V1, WGA, and DAPI. *D*, control experiment where the TCa_V1 antibody was preadsorbed with excess blocking peptide, revealing a complete loss of TCa_V1 label along the interior but some residual labeling in type II gland cells. *E*, top-down view of a three-dimensional reconstruction of the micrograph Z-stack shown in *C* reveals expression of TCa_V1 along the dorsal epithelium and within type II gland cells. *F*, side view of the three-dimensional reconstruction, with the dorsal epithelium oriented at the top and type II gland cells on the right. *G*, *bottom view* of the three-dimensional reconstruction showing reduced TCa_V1 labeling along the ventral epithelium. *H*, illustration of the dorsal view of *Trichoplax adhaerens*, indicating the relative area of the animal imaged in panels *I* and *J*. Whole mount fluorescence *in situ* hybridization signal using RNAscope probes are *red* for TCa_V1, *green* for TCa_V2, and *blue* for type II gland cells labeled using fluorophore-conjugated WGA. *I*, Z-projection fluorescence micrograph (xy) of a *Trichoplax* animal reveals enriched expression of TCa_V1 mRNA along the outer edge of the animal, including areas that overlap with WGA-positive type II gland cells and cells expressing the TCa_V2 channel mRNA. *J*, enlarged view of type II gland cells as shown in panel *I*, revealing overlapping labeling of both TCa_V1 and TCa_V2. *K*, Z-projection fluorescence micrograph (xz) of a 5 μm wide strip of the image stack shown in panel *I*, revealing expression of TCa_V1 mRNA along the outer edge and within interior regions. *L*, fluorescence micrograph of dissociated *Trichoplax* cells subjected to *in situ* hybridization for TCa_V1 (*green*), the fiber cell marker

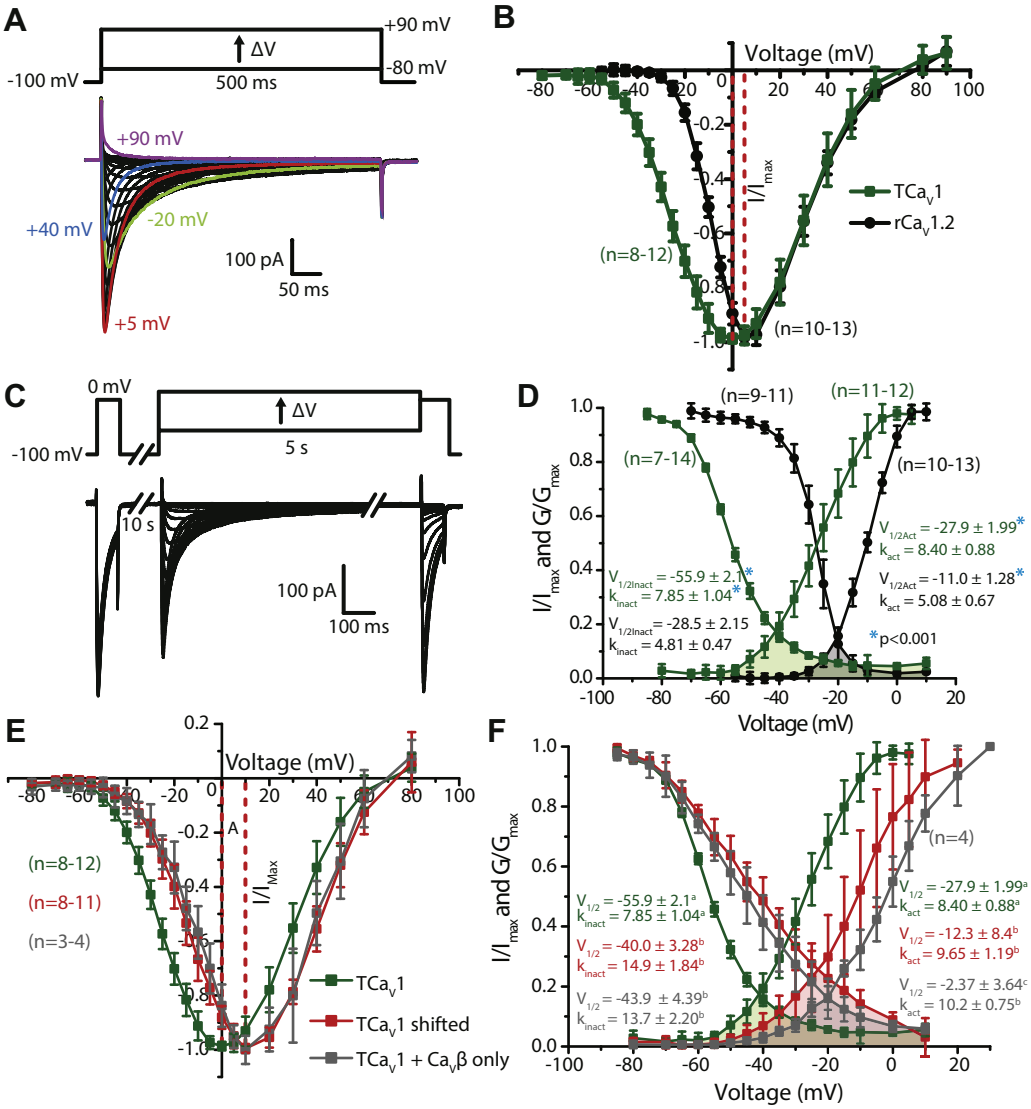

Figure 5. TCa_V1 channels conduct high-voltage–activated Ca^{2+} currents with large window currents *in vitro*. *A*, sample macroscopic current traces recorded *via* whole-cell patch voltage clamp of HEK-293T cells transfected with pTCa$_V$1-IR-EGFP, pKir2.1-cDNA3, rat Ca$_V$β1b, and Ca$_V$α$_2$δ$_1$ subunits. The voltage-clamp protocol used to elicit the currents is depicted above, showing depolarizing voltage steps from −80 to +90 mV. *B*, standardized average peak macroscopic Ca^{2+} current ±SD (*error bars*) through TCa$_V$1 (*green*) and rCa$_V$1.2 (*black*) channels plotted over corresponding voltage steps reveals a hyperpolarized current-voltage relationship of the *Trichoplax* channel relative to rCa$_V$1.2. *C*, voltage-clamp protocol used to assess inactivation of TCa$_V$1 and rCa$_V$1.2 channels (*top*) and sample currents recorded from the TCa$_V$1 channel (*bottom*). Peak amplitudes of inward Ca^{2+} currents elicited by a test pulse following a 5 s pulse to a range of inactivating voltages are compared to those elicited by a prepulse voltage step to 0 mV. *D*, plots of average inactivation and conductance ±SD reveal that TCa$_V$1 channel properties are left shifted relative to rCa$_V$1.2. The overlap between the inactivation and activation curves denotes window currents at voltages where a subset of channels are not inactivated and are able to become activated to constitutively conduct Ca^{2+} currents into the cell. The window current for TCa$_V$1 (*green fill*) is 20 mV left shifted and spans a greater voltage range than the rCa$_V$1.2 window current (*gray fill*). Average values for half-maximal activation and inactivation ($V_{1/2Act}$ and $V_{1/2Inact}$) and the slope factors k_{act} and k_{inact} are shown and were calculated by fitting the activation and inactivation data with Boltzmann functions. *Asterisks* denote a significant difference ($p < 0.001$) between corresponding TCa$_V$1 and rCa$_V$1.2 $V_{1/2}$ and k values as determined by a two-tailed *t* test. *E*, standardized average peak macroscopic Ca^{2+} current ±SD through TCa$_V$1 channels co-expressed with the rat Ca$_V$α$_2$δ$_1$ and Ca$_V$β1b subunits (*green*). Under the same conditions, certain cells produced currents that were right shifted with respect to their voltage dependence (*red*). These currents were replicated by cotransfecting TCa$_V$1 with Ca$_V$β1b and omitting the Ca$_V$α$_2$δ$_1$ subunit (*gray*). *F*, plots of average steady-state inactivation and conductance ±SD reveal that compared to co-expression with Ca$_V$β1b alone, the Ca$_V$α$_2$δ$_1$ subunit causes a leftward shift in the activation and inactivation curves of the TCa$_V$1 channel. The overlap between the inactivation and activation curves denotes the window currents. The Ca$_V$α$_2$δ$_1$ subunit left shifts the window current (*green fill*) by 20 mV and reduces its magnitude. Average values for half-maximal activation and inactivation ($V_{1/2}$) and the slope factors for activation (k_{act}) and inactivation (k_{inact}) are depicted and were calculated by fitting the activation and inactivation data with a Boltzmann function. *Lowercase letters* denote significant differences ($p \leq 0.015$) between $V_{1/2}$ and k values as determined by Holm–Sidak tests following one-way ANOVAs (Table S1). HEK, human embryonic kidney cell; rCa$_V$, *Rattus norvegicus* voltage-gated calcium channel; TCa$_V$, *T. adhaerens* voltage-gated calcium channel.

FoxC (*red*), and WGA type II gland cell labeling (*blue*). TCa$_V$1 mRNA was detected in type II gland cell that exhibit strong WGA labeling, in ventral epithelial cells (cell cluster near *left*), and in dorsal epithelial cells that exhibit weak, granular WGA staining (*inset*). No expression was observed in FoxC positive fiber cells. *M*, fluorescence micrograph of dissociated *Trichoplax* cells subjected to *in situ* hybridization for TCa$_V$2 (*green*), the fiber cell marker FoxC (*red*), and WGA type II gland cell labeling (*blue*). TCa$_V$2 mRNA was detected in type II gland cells, dorsal and ventral epithelial cells, and a subset of FoxC positive fiber cells. The *white* scale bar in all panels is 10 μm, and the *yellow* scale bar in the panel *L inset* is 5 μm. TCa$_V$, *T. adhaerens* voltage-gated calcium channel.

Table 1
Comparison of biophysical parameters of *Trichoplax* Ca_V1 to Ca_V3 channels and mammalian $Ca_V1.2$ and $Ca_V2.1$ channels

Biophysical parameter	TCa_V3[a]	TCa_V1	TCa_V2[b]	$rCa_V1.2$	$hCa_V2.1$[b]	TCa_V1 *versus* TCa_V2	$rCa_V1.2$ *versus* $hCa_V2.1$
Activation							
Initial opening (mV)	−70	−50	−30	−25	−20	Left shifted	Left shifted
Peak (mV)	−45	0	−10	5	5	Right shifted	Similar
$V_{1/2}$ (mV)	−59.32 ± 0.9	−27.9 ± 2.0	−17.7 ± 2.2	−11.0 ± 1.3	−4.4 ± 2.8	**Left shifted**	**Left shifted**
Slope factor (k, mV)	4.5 ± 0.3	8.4 ± 0.9	3.8 ± 0.7	5.1 ± 0.7	3.8 ± 0.4	**Larger**	**Larger**
Inactivation							
$V_{1/2}$ (mV)	−74.2 ± 0.9	−55.9 ± 2.1	−28.7 ±1.8	−28.5 ± 2.2	−34.3 ± 1.5	**Left shifted**	**Right shifted**
Slope factor (k, mV)	2.7 ± 0.1	7.9 ± 1.0	3.9 ± 0.5	4.8 ± 0.47	6.7 ± 1.0	**Larger**	**Smaller**
Window current							
Conductance and inactivation intersect (mV)	−68	−40	−22	−20	−15	Left shifted	Left shifted
I_{Window} size at intersect (%)	1.8	3.1	4.3	2.0	0.5	Smaller	Larger
Recovery from inactivation							
τ_1 (s)	1275.1±54.4	0.5 ± 0.1	1.6 ± 0.8	0.4 ± 0.2	0.7 ± 0.3	**Faster**	Similar
τ_2 (s)		8.6 ± 1.9	40 ± 6.1	7.1 ± 3.3	7.5 ± 3.5	**Faster**	Similar
Activation kinetics							
τ at 0 mV (ms)	11.3 ±1.3	2.6 ±0.7	10.5 ±1.5	2.1 ±0.2	2.6 ±0.3	**Faster**	**Faster**
τ at +50 mV (−50 mV for TCa_V3; ms)	35.3 ± 4.6	1.3 ± 0.2	3.8 ± 0.4	0.8 ± 0.2	0.5 ±0.1	**Faster**	**Slower**
Fold-change (0 to +50, or −50 to 0 mV)	3.1	1.8	2.9	2.1	5.2	Smaller	Smaller
Inactivation kinetics							
τ at 0 mV (ms)	52.8 ±4.8	178.8 ± 32.0[b]	144.6 ± 31.0	188.8 ± 33[b]	129.3 ± 19.5	**Slower**	**Slower**
τ at +40 mV (−40 for TCa_V3; ms)	59.0 ±7.2	169.3 ± 29.0[b]	185.2 ± 27.0	227.7 ± 45[c]	206.1 ± 39.2	Similar	Similar
Fold-change (0 to +40, or −40 to 0 mV)	1.1	1.1	1.3	1.2	1.6	Smaller	Smaller
Curve fitting	Mono-exp.	Bi-exp.	Mono-exp.	Bi-exp.	Mono-exp.	Bi-mono	Bi-mono
Deactivation kinetics							
τ at −120 mV (−110 mV for TCa_V3; ms)	1.2 ± 0.2	1.1 ± 0.2[d]	0.5 ± 0.2	0.5 ± 0.1	0.5 ± 0.05	**Slower**	Similar
τ at −40 mV (ms)	57.2 ± 8.8	2.1 ± 0.7[d]	4.0 ± 0.7	0.7 ± 0.03	0.7 ± 0.1	**Faster**	Similar
Fold-change (−120 to −40, or −110 to −40 mV)	47.7	1.9	8.0	1.4	1.4	Smaller	Similar
Curve fitting	Mono-exp.	Bi-exp.	Mono-exp.	Mono-exp.	Mono-exp.	Bi-mono	Mono-mono

Bold text represents significant differences after a two-tailed *t* test ($p < 0.05$).
[a] Data for the TCa_V3 channel were obtained previously using different recording solutions (*i.e.*, 2 mM external Ca^{2+}) (23).
[b] Data for TCa_V2 and $hCa_V2.1$ are from a previous publication (5).
[c] slow τ.
[d] fast τ.

hyperpolarized activation range, TCa_V1 also exhibited reduced voltage sensitivity for activation compared to $rCa_V1.2$. Next, we compared the voltage-dependent inactivation (VDI) properties of TCa_V1 and $rCa_V1.2$ to approximate the fraction of channels within a population that would be available for activation at different resting membrane potentials. A 0 mV depolarization step ("prepulse") was used to determine the peak amplitude of macroscopic Ca^{2+} currents before inactivation (Fig. 5*C*). This was followed by prolonged (5 s duration) inactivating voltage steps between −80 and +10 mV and a test pulse to 0 mV to measure the decline in inward current relative to the prepulse that resulted from the inactivating voltages. Plotting the test pulse/prepulse current amplitude ratio as a function of inactivating voltage resulted in an inactivation curve for TCa_V1 with a $V_{1/2}$ of −55.9 ± 2.1 mV and a slope factor (k_{inact}) of 7.85 ± 1.04 mV (Fig. 5*D*). Like activation, TCa_V1 inactivation was significantly left shifted and less voltage sensitive than $rCa_V1.2$, the latter having a $V_{1/2}$ value of −28.5 ± 2.15 mV and a k_{inact} of 4.81 ± 0.47 mV ($p < 0.001$, two-tailed *t* test). Notably, the TCa_V1 channel population did not fully inactivate, even at very depolarized voltages (Fig. 5*D*).

An important feature of calcium channels is their ability to conduct Ca^{2+} leak currents across a small range or "window" of resting voltages, where steady-state inactivation of the channel population is not complete, and a subset of channels can become activated. Window currents for example can contribute to the regulation of resting membrane potential, where tonic Ca^{2+} influx serves to draw the membrane voltage into the window current range (64). The overlap in the TCa_V1 activation and inactivation curves reveals that the *Trichoplax* channel produces a prominent window current in the voltage range between −60 and +10 mV (Fig. 4*D*, *green fill*), with a projected maximum that is 20 mV left shifted compared to $rCa_V1.2$ (Fig. 4*D*, *gray fill*). This is consistent with the difficulty we initially had in recording TCa_V1 in HEK-293T cells, which have a resting voltage of roughly −25 mV (63). At −25 mV, roughly 7.2 ±1.6% of the TCa_V1 channel population would be in an activatable state, of which 55.7 ±8.7% could become activated, compared to 34.9 ±9.0% and 6.7 ±2.4% for $rCa_V1.2$, respectively. The product of these two values estimates the fraction of channels that would constitutively conduct calcium into the cell, which is 4.0% for TCa_V1, compared to only 2.3% for $rCa_V1.2$. Altogether, when comparing the activation and inactivation properties of the three *Trichoplax* Ca_V channels, it is apparent that TCa_V1 operates in a voltage range that is between TCa_V3 and TCa_V2 channels (Fig. S4*B*) (5, 24). Furthermore, all three *Trichoplax* Ca_V channels, and especially TCa_V1, produce prominent window currents *in vitro* that would permit Ca^{2+} influx across a broad range of resting voltages (Fig. S4*B*).

Interestingly, a subset of cells expressing the TCa_V1 channel produced currents with right shifted current–voltage properties compared to the more typical recordings (Fig. 5*E*). This population of channels exhibited half-maximal ($V_{1/2}$) activation at −12.3 ± 8.4 mV and half-maximal inactivation at −40.0 ± 3.28 mV (Fig. 5*F*), both of which were significantly different from the standard currents reported above ($p < 0.001$ with Holm–Sidak tests after one-way ANOVAs; $p < 0.001$, F ≥

36.6 for all comparisons; Table S1). The slope factors k_{act} (9.65 ± 1.19 mV) and k_{inact} (14.9 ± 1.84 mV) were also significantly larger, indicative of reduced voltage sensitivity ($p < 0.001$ with Holm–Sidak tests after one-way ANOVAs; $p \leq 0.015$, $F \geq 6.9$ for all comparisons; Table S1). Compared to the more typical currents, these cells exhibited an even larger window current, with an estimated 6.3% of channels conducting calcium ions at a resting voltage of −25 mV, compared to 4.0% for most other cells. Given the relative infrequency of these atypical currents and the knowledge that $Ca_V\beta$ and $Ca_V\alpha_2\delta$ subunits can significantly impact channel expression and gating, we reasoned that perhaps one or both subunits were not expressed in these cells or expressed at a lower level and hence not interacting with a subset of channels, accounting for the altered biophysical properties. Thus, we tried recreating these currents by recording cells in which either $Ca_V\beta_{1b}$, $Ca_V\alpha_2\delta_1$, or both subunits were excluded in the transfection. Interestingly, omission of both subunits, or just $Ca_V\beta_{1b}$, did not result in recordable TCa_V1 currents. However, omission of just $Ca_V\alpha_2\delta_1$ produced currents with voltage properties that were very similar to the atypical currents, with a peak inward current at +10 mV and a statistically indistinguishable inactivation curve with a $V_{1/2}$ value of −43.9 ± 4.39 mV and a k_{inact} value of 13.7 ± 2.20 (Fig. 5*E* and *F*). In the absence of co-expressed $Ca_V\alpha_2\delta_1$, the activation curve was also similar with a statistically indistinguishable k_{inact} value of 10.2 ± 0.75 and an even more right-shifted $V_{1/2}$ value of −2.37 ± 3.64 (Fig. 5*F*). Altogether, the $Ca_V\alpha_2\delta_1$ subunit has a net hyperpolarizing influence on TCa_V1 voltage properties and increases its sensitivity to changes in voltage. Surprisingly, even though $Ca_V\alpha_2\delta_1$ increased pEGFP-TCa_V1 expression (Fig. 3, *C* and *D*), there was no significant difference in peak current density between TCa_V1 channels co-expressed with both subunits (−6.9 ± 4.0 pA/pF) and in the absence of $Ca_V\alpha_2\delta_1$ (−3.1 ± 2.1 pA/pF), although the difference was trending on significant ($p = 0.07$, two-tailed *t* test). Furthermore, our inability to record TCa_V1 currents in the absence of the $Ca_V\beta$ subunit suggests that even though both subunits promote similar increases in total channel protein expression (Fig. 3, *C* and *D*), the $Ca_V\beta$ subunit plays a more crucial role in targeting TCa_V1 to the plasma membrane.

Another biophysical property that was examined was the recovery from inactivation. Ca_V channels with fast recovery from inactivation tend to remain active through prolonged bouts of excitation (*e.g.*, AP burst firing), allowing for consistent levels of cytoplasmic Ca^{2+} influx. In contrast, channel populations with slow recovery are expected to accumulate inactivation and hence contribute less and less Ca^{2+} with prolonged excitation (65). To compare the recovery from inactivation for TCa_V1 and $rCa_V1.2$, we subjected the channels to a 10-s inactivating pulse and determined the peak current that could be elicited by a 0 mV step at different time intervals after inactivation (Fig. 6*A*). Consistent with previous reports (66, 67), the time course for recovery of $rCa_V1.2$ was fitted by two time constants, with respective fast and slow components for the recovery process of 0.39 ± 0.24 ms (τ1) and 7.10 ± 3.32 ms (τ2; Fig. 6*B*). The TCa_V1 channel population also exhibited bimodal recovery from inactivation and had statistically indistinguishable time constants of τ1 = 0.48 ± 0.13 ms ($p = 0.441$, two-tailed *t* test) and τ2 = 8.63 ± 1.85 ms ($p = 0.424$, two-tailed *t* test). Notably, TCa_V1 recovery from inactivation falls between that of TCa_V2, which recovers more slowly, and TCa_V3, which recovers more quickly (Fig. S4*C*). In this respect, TCa_V1 more resembles $rCa_V1.2$ than its two *Trichoplax* paralogues.

TCa_V1 exhibits slower kinetics than $rCa_V1.2$, with similar voltage dependencies

To compare the kinetic properties of TCa_V1 and $rCa_V1.2$ channel activation and inactivation, we fitted monoexponential or biexponential curves over the rise and decay phases of macroscopic TCa_V1 and $rCa_V1.2$ currents, producing respective time constants (Fig. 7, *A*–*C*). With increasing depolarization, both channels exhibited accelerating single component $\tau_{activation}$ values (Fig. 7*A*), decreasing ∼2.6 fold from −15 mV

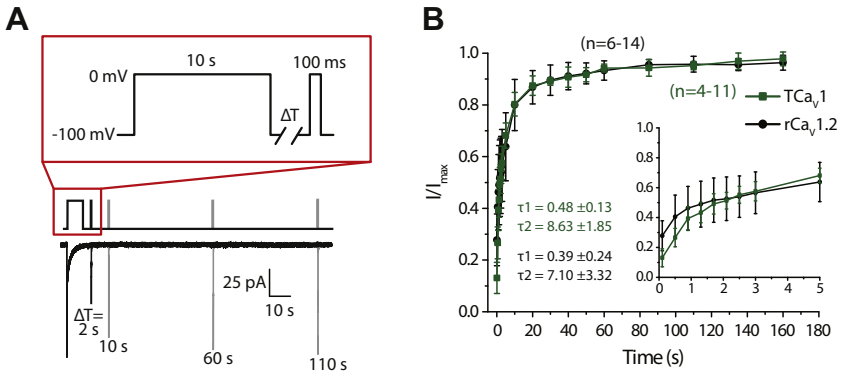

Figure 6. TCa_V1 and $rCa_V1.2$ exhibit similar bimodal recovery from inactivation. *A*, voltage-clamp protocol used to assess recovery from inactivation of TCa_V1 and $rCa_V1.2$ channels (*top*) and sample current traces recorded for the TCa_V1 channel (*bottom*). Peak amplitudes of inward Ca^{2+} currents elicited by a test pulse were measured at various intervals after a 10 s inactivating pulse. *B*, plots of average recovery from inactivation ±SD (error bars) of TCa_V1 and $rCa_V1.2$ channels. *Inset*, current amplitude recovery data for the first 5 s, with inflections in the curves indicative of two component recovery from inactivation for both channels. Biexponential curve fitting over the data produced similar τ1 and τ2 values for TCa_V1 and $rCa_V1.2$. rCa_V, *Rattus norvegicus* voltage-gated calcium channel; TCa_V, *T. adhaerens* voltage-gated calcium channel.

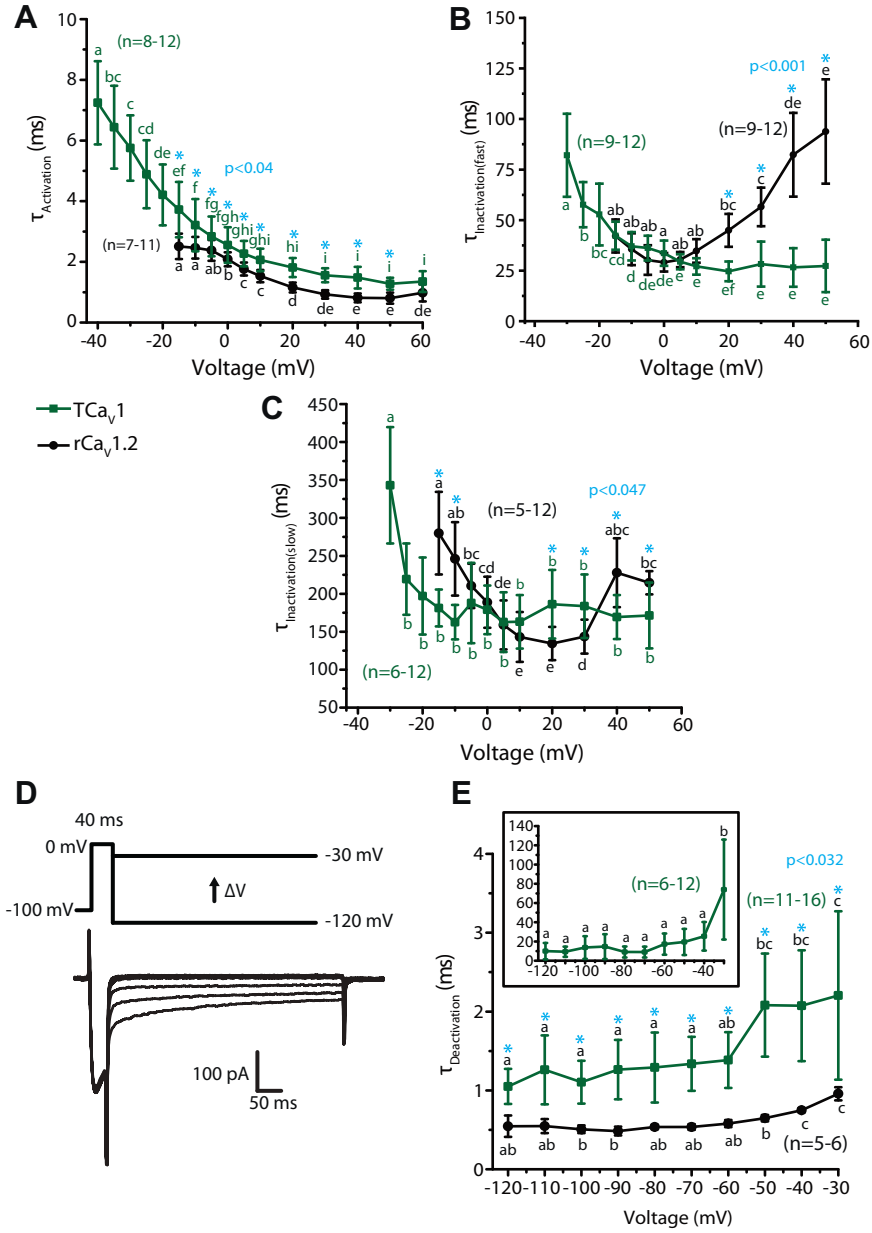

Figure 7. The activation and deactivation kinetics of TCa_V1 macroscopic currents resemble those of $rCa_V1.2$ in their voltage dependence, but the inactivation kinetics do not. *A*, plot of average $\tau_{Activation}$ values ±SD (*error bars*) over depolarizing voltages. $\tau_{Activation}$ values were obtained by monoexponential curve fitting of the activation phase of macroscopic Ca^{2+} currents. Both TCa_V1 and $rCa_V1.2$ exhibited accelerating activation with stronger depolarization, indicated by their decreasing $\tau_{Activation}$ values, with TCa_V1 activating significantly slower at all corresponding depolarizing voltages. *B*, plot of average fast component $\tau_{Inactivation}$ values ±S.D. obtained by biexponential curve fitting over the inactivation phase of macroscopic Ca^{2+} currents elicited by different depolarizing voltages. TCa_V1 exhibited decreasing $\tau_{Inactivation(fast)}$ values, whereas $rCa_V1.2$ exhibited increasing values with stronger depolarization. *C*, plot of average slow component $\tau_{Inactivation}$ values ±SD obtained by biexponential curve fitting over the inactivation phase of macroscopic Ca^{2+} currents. TCa_V1 exhibited similar $\tau_{Inactivation(slow)}$ values at most voltages, whereas the $rCa_V1.2$ data were U-shaped. *D*, protocol used to assess deactivation kinetics (*top*), with a brief step to 0 mV followed by hyperpolarizing pulses to varying voltages. Sample TCa_V1 tail current traces are shown below. *E*, plot of average $\tau_{Deactivation}$ ±SD for $rCa_V1.2$, and the fast $\tau_{Deactivation}$ ± SD component for TCa_V1 channels, revealing accelerating deactivation upon stronger hyperpolarization for both channels. The $rCa_V1.2$ $\tau_{Deactivation}$ values were obtained by monoexponential curve fitting of the tail currents, whereas TCa_V1 tail currents required biexponential curve fitting, producing fast and slow $\tau_{Deactivation}$ components. *Inset*, plot of the slow TCa_V1 $\tau_{Deactivation}$ values ±SD. Across all voltages, the fast TCa_V1 $\tau_{Deactivation}$ exhibits slower deactivation kinetics than $rCa_V1.2$. In panels *A*, *B*, *C*, and *E*, *different letters* above data points denote statistically significant differences ($p < 0.05$) using a Holm–Sidak test after respective one-way repeated measures ANOVAs for TCa_V1 and $rCa_V1.2$ τ values. *Asterisks* denote statistically significant differences ($p < 0.05$) for paired comparisons of TCa_V1 *versus* $rCa_V1.2$ current τ values at different voltages using Holm–Sidak tests after two-way ANOVAs (Table S1). rCa_V, *Rattus norvegicus* voltage-gated calcium channel; TCa_V, *T. adhaerens* voltage-gated calcium channel.

to +60 mV ($p < 0.05$ for Holm–Sidak tests after one-way repeated measures ANOVAs; $p < 0.001$ and $F \geq 68.9$ for all comparisons; Table S1). Because TCa_V1 channels started activating at more hyperpolarized voltages compared to $rCa_V1.2$, we could reliably curve-fit and quantify TCa_V1 activation and inactivation kinetics to −40 mV, showing an extended trend of accelerating kinetics with stronger depolarization. Despite the similar trend, the activation of TCa_V1 was slightly slower than $rCa_V1.2$, with respective $\tau_{activation}$ values of 3.7 ± 1.1 ms and 2.5 ± 0.4 ms at −15 mV and 1.3 ±

0.2 ms and 0.8 ± 0.2 ms at +50 mV ($p \leq 0.02$ for a Holm–Sidak test after two-way ANOVA; $p < 0.001$ and $F \geq 9.1$ for all comparisons; Table S1). Among TCa_V channels, TCa_V1 activation kinetics are very similar to those of TCa_V3, and both are considerably faster than TCa_V2 (Fig. S4*D*) (5, 24).

The inactivation kinetics of both TCa_V1 and $rCa_V1.2$ had two components, $\tau_{inactivation(fast)}$ and $\tau_{inactivation(slow)}$, and both components were voltage dependent (Fig. 7, *B* and *C*). $Ca_V1.2$ channels were previously reported to also inactivate with two time constants (66, 67), with a fast component that decelerates with increasing membrane depolarization and a U-shaped slow component (67). In the present study, similar statistically significant trends were observed for the $rCa_V1.2$ channel ($p \leq 0.04$ for Holm–Sidak tests after one-way repeated measures ANOVAs; $p < 0.001$ and $F \geq 18.8$ for all comparisons; Table S1). In contrast, the TCa_V1 $\tau_{inactivation(fast)}$ kinetics accelerated with increasing voltage steps, whereas $\tau_{inactivation(slow)}$ accelerated from −30 mV to −25 mV then remained stable for all successive voltage steps ($p \leq 0.03$ for Holm–Sidak tests after one-way repeated measures ANOVAs; $p < 0.001$ and $F \geq 11.0$ for all comparisons; Table S1). As a result, at voltage steps to +20 mV or greater, both the fast and slow components of inactivation were significantly different between TCa_V1 and $rCa_V1.2$ channels ($p < 0.05$ for Holm–Sidak tests after two-way ANOVAs; $p < 0.001$ and $F \geq 8.9$ for all comparisons; Table S1). Despite the differences, TCa_V1 and $rCa_V1.2$ resemble each other because both exhibit two-component inactivation, with fast and slow inactivating components that roughly fall within the same timescales. Compared to the other *Trichoplax* Ca_V channels, both of which inactivated with a single time constant (5, 24), it is notable that the fast inactivation component for TCa_V1 resembles that of TCa_V3, while the slow inactivation component resembles that of TCa_V2 (Fig. S4*E*).

Finally, we examined the deactivation kinetics of the TCa_V1 and $rCa_V1.2$ channels. This property reflects how quickly channels transition from an open state to a closed, activatable state upon membrane hyperpolarization. Ca_V channels with slow deactivation remain open longer, thus conducting larger Ca^{2+} currents during AP repolarization (*i.e.*, tail currents) (68). TCa_V1 and $rCa_V1.2$ differ in that $rCa_V1.2$ deactivation is a single component process, whereas TCa_V1 deactivation is a double component process. Monoexponential curves were fitted over the tail currents elicited through open $rCa_V1.2$ channels upon hyperpolarization to voltages between −120 mV and −30 mV, whereas biexponential curves were fitted over the TCa_V1 tail currents (Fig. 7*D*). For both channels, $\tau_{deactivation}$ exhibited voltage-dependent deceleration (Fig. 7*E*). Both TCa_V1 $\tau_{deactivation(fast)}$ and $rCa_V1.2$ $\tau_{deactivation}$ increased ∼2 fold, from 1.1 ± 0.2 ms at −120 mV to 2.2 ± 1.1 ms at −30 mV for TCa_V1 and from 0.5 ± 0.1 ms at −120 mV to 1.0 ± 0.1 ms at −30 mV for $rCa_V1.2$ ($p \leq 0.04$ for Holm–Sidak tests after one-way repeated measures ANOVAs; $p < 0.001$ and $F \geq 8.7$ for all comparisons; Table S1). On the other hand, TCa_V1 $\tau_{deactivation(slow)}$ was similar at most voltages, except at −30 mV, where the τ value increased to 73.9 ± 52.0 ms (Fig. 7*E*, *inset*; $p < 0.001$ for Holm–Sidak tests after a one-way repeated measures ANOVA; $p < 0.001$ and $F = 10.0$ for all comparisons; Table S1). At the more depolarized voltages of −40 to −30 mV, there is a possibility that channel inactivation is contributing to the current decay because the TCa_V1 channel undergoes activation and inactivation at these voltages. This suggests that the deactivation time may be even slower at these voltages. At all voltages, the fast deactivation component of TCa_V1 was slightly slower than $rCa_V1.2$ deactivation ($p \leq 0.03$ for Holm–Sidak test after two-way ANOVA; $p \leq 0.042$ and $F \geq 2$ for all comparisons; Table S1), although both remained within a similar timescale across all voltages. Lastly, the classic distinction that Ca_V3 channels tend to have slower deactivation kinetics than Ca_V1 and Ca_V2 channels (69) seems to hold true for the *Trichoplax* homologues, at least when considering the fast deactivation component of TCa_V1 (Fig. S4*F*).

Brief, repetitive depolarization elicits similar responses from TCa_V1 and TCa_V2 channels

T. adhaerens and *H. hongkongensis* cells were recently shown to exhibit APs (21). Extracellular recordings of *Hoilungia* crystal cells, which are identified as gravity sensors in the Placozoa (70), revealed APs ranging in duration from 1 to 3 ms and with a frequency of ∼130 Hz (21). In accordance with these observations, placozoans express an array of genes required for establishing resting membrane potential and generating graded and APs (19, 20, 30), including a unique expansion of Na_V channels (21) and a complete repertoire of Shab, Shal, Shaw, and Shaker voltage-gated potassium channels (71). Thus, we sought to explore how TCa_V1 and TCa_V2 channels will respond to simulated conditions of repeated excitation. We therefore applied a series of short depolarizing square pulses from −70 mV to +30 mV with a duration of 1, 2, or 3 ms to mimic APs of varying duration and frequency over the course of 1 s (Fig. 8*A*). At 100 Hz, as the duration of stimulation increased, the initial inward current amplitude increased with the pattern 3 ms > 2 ms > 1 ms, likely because more channels were able to activate when the depolarizations were longer, producing larger tail currents in response to membrane repolarization after each pulse (Fig. 8*B*). However, even though the initial current amplitude increased with pulse duration, the tail current amplitude decayed more rapidly over the course of 1 s. This suggests that at a frequency of 100 Hz, 2 and 3 ms-long pulses build up channel inactivation, whereas 1 ms depolarizations do not; a trend that can be seen for both TCa_V1 and TCa_V2 channels. Interestingly, when the pulses were 2 and 3 ms long, TCa_V1 channels conducted Ca^{2+} as a combination of inward currents upon channel activation and tail currents, whereas Ca^{2+} influx through TCa_V2 channels could only be observed as tail currents (Fig. 8*B*). This is likely due to the faster activation kinetics of TCa_V1 channels compared to TCa_V2 (Fig. S4). To determine if the differences in current amplitude reflect differences in cumulative Ca^{2+} influx, we examined the area of the inward Ca^{2+} currents elicited by 1, 2, and 3 ms depolarization pulses at 100 Hz over 1 s (Fig. 8*C*). To control for differences in channel expression levels between cells, we normalized the cumulative area of the Ca^{2+} currents to the peak amplitude of a voltage step that

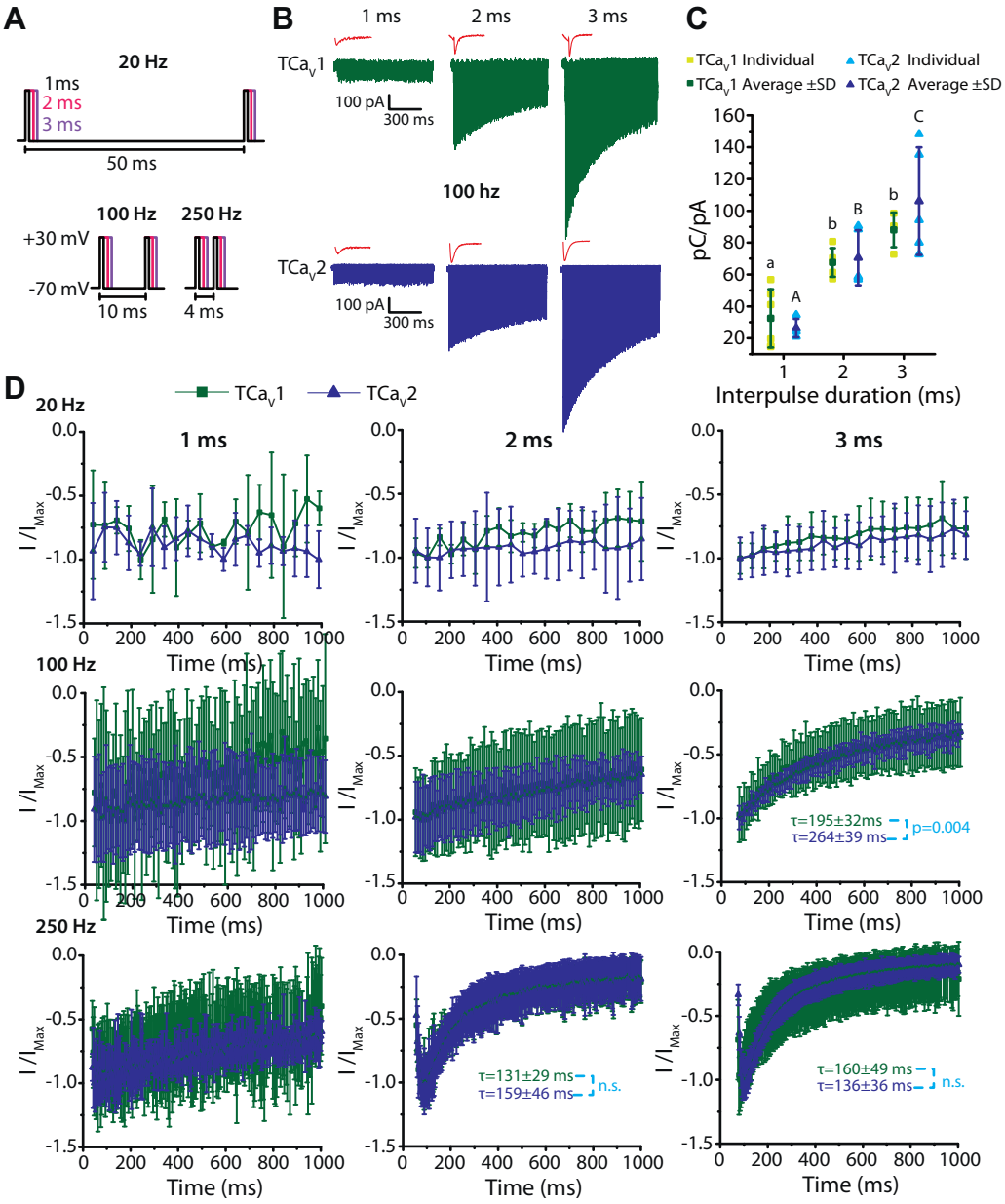

Figure 8. TCa_V1 and TCa_V2 channels respond similarly to short, repetitive depolarizing pulses. *A*, depolarization steps from −70 mV to +30 mV lasting 1 ms (*black*), 2 ms (*pink*), or 3 ms (*purple*) at frequencies of 20, 100, or 250 Hz were used to elicit macroscopic Ca^{2+} currents through TCa_V1 and TCa_V2 channels. The time from the start of one depolarizing pulse to another is depicted below the voltage-protocol illustrations. *B*, sample macroscopic Ca^{2+} currents through TCa_V1 (*green*) and TCa_V2 (*blue*) channels in response to repetitive 1, 2, or 3 ms depolarizing steps for 1 s at a frequency of 100 Hz. The current resulting from the first pulse of each train is expanded and depicted in *red* (not to scale). *C*, average integrated Ca^{2+} current mediated by the TCa_V1 and TCa_V2 channels ±SD (*error bars*) at 100 Hz. Each dataset was obtained by integrating the total Ca^{2+} current in response to 1, 2, or 3 ms depolarizing pulses (pC units) and then normalizing to the peak current response (pA units) of a preceding 500 ms step depolarization to 0 mV. Cumulative Ca^{2+} influx was significantly lower when the depolarizing pulses were 1 ms long compared to 2 or 3 ms for both channels, but there was no difference in cumulative current between TCa_V1 and TCa_V2 channels. *Uppercase letters* denote significant differences between average TCa_V2 values and *lowercase letters* denote significant differences between average TCa_V1 values ($p \leq 0.01$) as determined by a Holm–Sidak test after a two-way ANOVA (Table S1). *D*, plots of peak current amplitudes ±SD mediated by the TCa_V1 and TCa_V2 channels over the course of 1 s in response to repetitive 1, 2, or 3 ms depolarizing pulses at frequencies of 20, 100, or 250 Hz. To compare the decay of current over time from the TCa_V1 and TCa_V2 channels, current amplitudes were normalized to a maximal inward current value within the 1 s depolarization train, and these were curve fitted with a monoexponential decay function starting from the maximum inward current to determine average time constants (τ) for the decay process. The probability value reflects a statistically significant difference ($p = 0.004$) in average τ values between TCa_V1 and TCa_V2 using a two-tailed *t* test. TCa_V, *T. adhaerens* voltage-gated calcium channel.

elicited maximal channel activation (see Experimental procedures). For both TCa_V1 and TCa_V2 channels, the cumulative integrated Ca^{2+} current was lowest with a 1 ms depolarization protocol (32.5 ± 18.3 pC/pA for TCa_V1, 26 ± 5.8 pC/pA for TCa_V2) and higher when the pulses were 2 ms (67.5 ± 9 pC/pA for TCa_V1, 70.5 ± 17.3 pC/pA for TCa_V2) or 3 ms long (88 ± 10.9 pC/pA for TCa_V1, 106 ± 33.8 pC/pA for TCa_V2; $p < 0.01$ with a Holm–Sidak test after a two-way ANOVA; $p < 0.001$ and $F = 30$ for all comparisons; Table S1). Finally, we examined the effect of varying depolarization pulse frequency on the peak Ca^{2+} current decay. We compared peak inward Ca^{2+} current amplitudes elicited by

TCa_V1 and TCa_V2 channels with 1, 2, and 3 ms depolarization pulses that had a frequency of 20, 100, and 250 Hz (Fig. 8, *A* and *D*). As the duration and frequency of the depolarization steps increased, there was a greater decay in current amplitude for both TCa_V1 and TCa_V2. At 250 Hz, the current amplitudes increased for the first few depolarization steps and then began to decay. The only condition that produced a difference in current decay between TCa_V1 and TCa_V2 channels was 3 ms pulses at 100 Hz, where TCa_V1 exhibited faster decay with a τ value of 195 ±32 ms, compared to 264 ±39 ms for TCa_V2 (Fig. 8*D*; $p = 0.004$ for two-tailed *t* test). Altogether, under the experimental conditions tested, TCa_V1 and TCa_V2 channels conduct similar levels of Ca^{2+} into the cytoplasm in response to a wide range of high-frequency stimulations.

TCa_V1 resembles $rCa_V1.2$ in its sensitivity to the cation channel blocker Cd^{2+} but is insensitive to DHPs

In vertebrates, the divalent cation cadmium (Cd^{2+}) is considered a general blocker of high-voltage–activated Ca_V channels (72). Previously, we found the TCa_V2 channel to have a Cd^{2+} block IC_{50} of 20.6 ± 2.8 μM, which was considerably less sensitive than human $Ca_V2.1$ with an IC_{50} of 1.0 ± 0.2 μM (5). Perfusion of external Cd^{2+} at increasing concentrations blocked TCa_V1 and $rCa_V1.2$ channels with a similar affinity as TCa_V2, with respective IC_{50} values of 11.4 ± 0.8 μM and 12.6 ± 2.5 μM that did not significantly differ from one another (Fig. 9*A*; $p = 0.317$ after a two-tailed *t* test). Thus, Cd^{2+} blocked the TCa_V1 and TCa_V2 channels with a lower affinity than the more sensitive $hCa_V2.1$ channel.

We next examined the effects of the DHPs, nifedipine and isradipine, which are selective blockers of mammalian Ca_V1 channels (73). As expected, the $rCa_V1.2$ channel was completely blocked by 10 μM of nifedipine and isradipine (99.7 ± 0.001% and 94.9 ± 0.06% block, respectively). In contrast, TCa_V1 was relatively insensitive exhibiting a 5.7 ± 0.04% block by 10 μM nifedipine and a 11.5 ± 0.02% block by 10 μM isradipine (Fig. 9, *B* and *C*). The *Trichoplax* channel is therefore slightly less sensitive to DHP block than the Ca_V1 channel from the jellyfish *C. capillata*, where 10 μM nifedipine blocked peak current by roughly 25%, and 100 μM isradipine caused 36% block (31). The most studied invertebrate Ca_V1 channel with respect to DHP sensitivity is the homologue from *Lymnaea* (LCa_V1), which unlike TCa_V1 is fully blocked by 10 μM nifedipine (50). Nevertheless, side-by-side comparison of the snail channel with $rCa_V1.2$ revealed a reduced sensitivity to DHP block, where isradipine produced an IC_{50} value of 632 nM for LCa_V1 *versus* 43 nM for $rCa_V1.2$ (74). In this particular study, comparison of known amino acids for DHP binding that are distributed within the Ca_V1 channel DIII S5–S6 helices and the DIV P-loop and S6 helices (74–80), combined with structural modeling, identified three key amino acids that differed in the *Lymnaea* homologue compared to $rCa_V1.2$ (*i.e.*, asparagine^{3o18}, phenylalanine^{3i10}, and isoluecine^{4i12}; Fig. 9*D*). Mutation of these residues in LCa_V1 to match those of $rCa_V1.2$ (*i.e.*, $N^{3o18}Q$, $F^{3i10}Y$, and I^{4i12} M) increased the channel's sensitivity to isradipine to a level that resembled the rat channel, reducing the IC_{50} by an order of magnitude to 64.5 nM (74). Analysis of the TCa_V1 channel protein sequence revealed that like LCa_V1, it lacks the 3o18 glutamine (N) and 4i12 methionine (M) residues but contains a tyrosine (Y) in position 3i10 (Fig. 9*D*). This is also the case for the Ca_V1 channels from the cnidarians *N. vectensis* and *Aiptasia pallida*, but interestingly, the *C. capillata* homologue, noted as less sensitive to DHP block than mammalian Ca_V1 channels (31), contains the same residues in these key positions as $rCa_V1.2$. The *Trichoplax* and cnidarian Ca_V1 channels also differ at additional positions from the vertebrate and *Lymnaea* homologues (Fig. 9*D*), and it may be that the lowered sensitivity for the *Cyanea* homologue is attributable to these divergent sites.

Lastly, we tested the effects of the DHP stereoisomers *S*(-)-BayK 8644 and *R*(+)BayK 8644, which respectively enhance and block macroscopic currents through mammalian Ca_V1 channels (81, 82). When applied extracellularly to the TCa_V1 channel, 5 μM of the *S*(-) isomer increased the macroscopic currents elicited from a voltage step from −100 to 0 mV, but not to the same extent as $rCa_V1.2$ (Fig. 8*E*). This resulted in a 1.11 ± 0.024-fold increase in peak current for TCa_V1 *versus* 1.64 ± 0.32-fold increase for rCav1.2 (Fig. 9*F*; $p = 0.004$ for a two-tailed *t* test). The *R*(+) isomer blocked TCa_V1 channel currents (74.2 ± 0.05% block), but only at the highest concentration of 100 μM, whereas the $rCa_V1.2$ channel was blocked by 97.3 ± 0.01% (Fig. 9*G*; $p < 0.001$ for a Holm–Sidak test after a two-way ANOVA; $p < 0.001$ and $F \geq 29.3$ for all comparisons; Table S1). Altogether, TCa_V1 is much less sensitive to DHPs compared to mammalian orthologues.

TCa_V1 and TCa_V2 exhibit differential regulation by CaM, like bilaterian channels

As noted, the *Trichoplax* Ca_V1 and Ca_V2 channels both possess conserved C-terminal EF-hand, pre-IQ, and IQ domains where the cytoplasmic Ca^{2+} sensor protein binds and generally promotes CDI (Figs. 1*F* and 10*A*) (10). Alignment of various calcium channel protein sequences reveals the conserved nature of the EF-hand, pre-IQ, and IQ domains in Ca_V1 and placozoan Ca_V2 channels (Fig. 10*B*). We note that key amino acids for preassociation of Ca^{2+}–free CaM (ApoCaM), identified in $Ca_V1.3$ channels within the EF-hand and IQ regions (83), as well as aromatic amino acids in the IQ domains of $Ca_V1.2$ and $Ca_V2.1$/$Ca_V2.3$ channels that anchor Ca^{2+}–bound CaM in X-ray crystallography structures (84–86), are broadly conserved (Fig. 10*B*). Notable is that the placozoan Ca_V1 and Ca_V2 channels bear several amino acid differences in these regions, more so than the early diverging homologues from cnidarians (Fig. 10*B*). Also notable is that amino acids that are deterministic for C-lobe regulation (*i.e.*, C-lobe effector sites), which underlie the unique regulation of Ca_V1 channels by CaM (83), are not necessarily more similar between TCa_V1 and other Ca_V1 channels, compared to TCa_V2. Specifically, each *Trichoplax* channel type differs at six of these marked positions, occurring differentially within the EF-hand and pre-IQ domain structures (Fig. 10*B*).

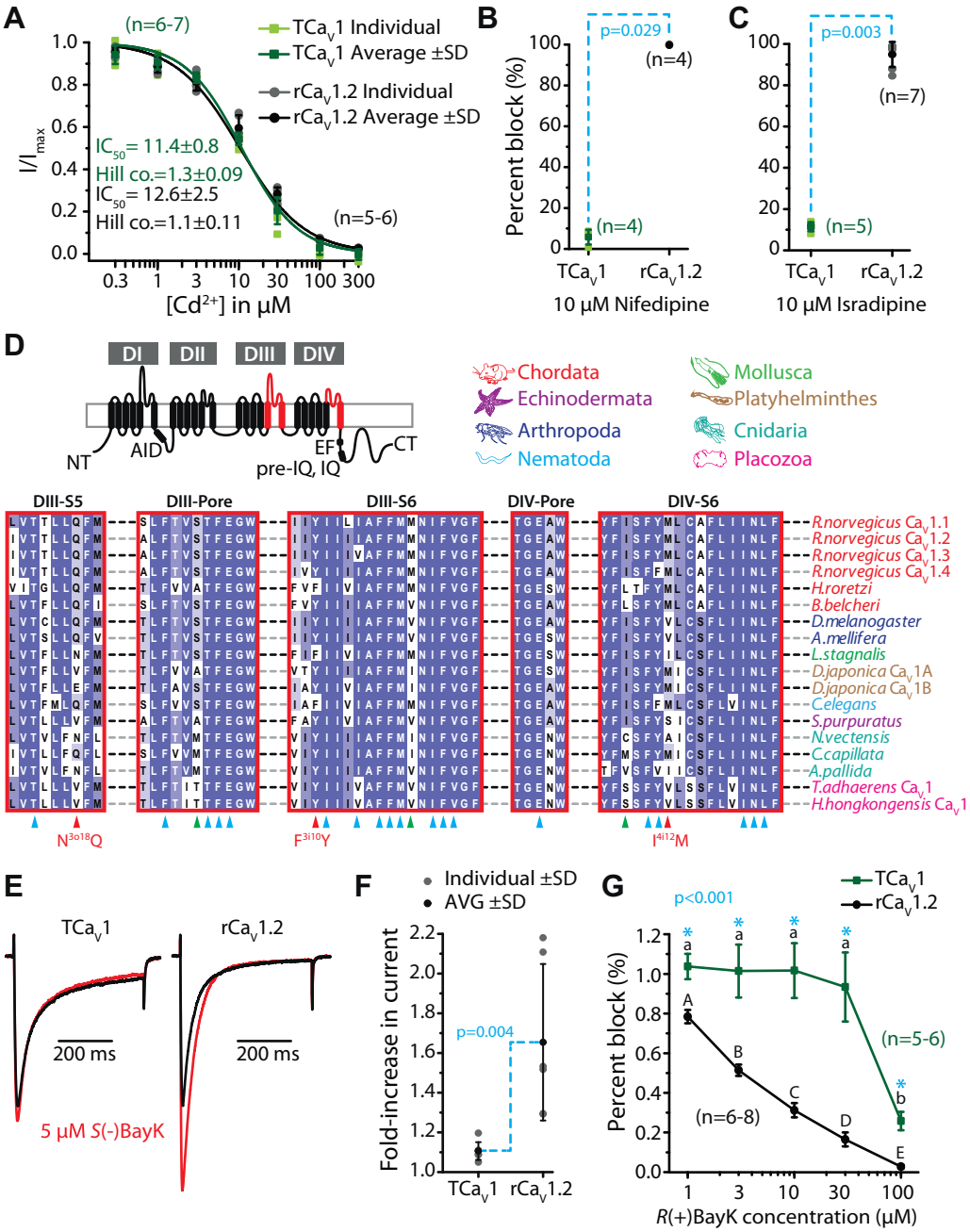

Figure 9. The TCa_V1 channel has similar sensitivity to cadmium (Cd^{2+}) block as the $rCa_V1.2$ channel but is relatively insensitive to dihydropyridines. *A*, dose–response curve for block of average TCa_V1 and $rCa_V1.2$ peak macroscopic currents ±SD (*error bars*) with increasing concentrations of perfused external Cd^{2+} ions. IC_{50} and Hill coefficients ±SD are shown and were statistically indistinguishable between the two channels. *B*, plot of average percent block ±SD of peak macroscopic currents elicited by voltage steps to 0 mV for TCa_V1 and $rCa_V1.2$ upon external perfusion of 10 µM nifedipine, revealing complete block (99.7 ± 0.1%) for the $rCa_V1.2$ channel, as opposed to only 5.8 ± 3.6% block for TCa_V1 ($p = 0.029$ using a two-tailed *t* test). *C*, plot of average percent block ±SD of peak macroscopic currents at 0 mV for TCa_V1 and $rCa_V1.2$ by external perfusion of 10 µM isradipine, revealing nearly complete block (95.0 ± 6.1%) for the $rCa_V1.2$ channel, as opposed to only 11.5 ± 2.2% block for TCa_V1 ($p = 0.003$ using a two-tailed *t* test). *D*, *top left*, illustration of Ca_V1 channel protein highlighting regions that bear residues associated with high-affinity dihydropyridine binding (*red*). *Top right*, color-coding of phyla corresponding to the aligned Ca_V1 channel protein sequences shown below. *Bottom*, protein alignment of the DIII-S5, DIII pore-loop, DIII-S6, DIV pore-loop, and DIV-S6 regions of various Ca_V1 channels reveals presence/absence of key residues important for dihydropyridine binding. *Blue* and *red* chevrons reflect positions determined to be important for dihydropyridine block of mammalian and *Lymnaea stagnalis* channels, whereas *green* chevrons denote positions where TCa_V1 and cnidarian Ca_V1 channels differ from the mammalian and *Lymnaea* homologues. *E*, sample TCa_V1 and $rCa_V1.2$ current traces elicited by a voltage step from −100 mV to 0 mV with extracellular perfusion of 0 (*black*) or 5 µM *S*(-)BayK 8644 (*red*). *F*, plot of average fold-increase in current amplitude ±SD for TCa_V1 and $rCa_V1.2$ channels after application of 5 µM extracellular *S*(-)BayK 8644 agonist. Current amplitudes with 5 µM *S*(-)BayK 8644 were normalized to currents from the same cell prior to addition of the drug. Application of *S*(-)BayK 8644 caused a significantly greater increase in current for $rCa_V1.2$ compared to TCa_V1 ($p = 0.004$ for two-tailed *t* test). *G*, dose–response curve for change in mean TCa_V1 and $rCa_V1.2$ peak macroscopic currents ±SD with increasing concentrations of *R*(+)BayK 8644, revealing that TCa_V1 is only blocked by this stereoisomer at high concentrations. Current amplitudes with *R*(+)BayK perfusion were normalized to currents from the same cell perfused with external solution lacking *R*(+)BayK. *Uppercase* and *lowercase letters* denote within-group significant differences ($p \leq 0.003$) and *asterisks* denote between-group (*i.e.*, TCa_V1 *versus* $rCa_V1.2$) significant differences ($p \leq 0.001$) as determined by Holm–Sidak tests after a two-way ANOVA (Table S1). For all experiments, the holding potential was −100 mV. DI to DIV, domains I to IV; rCa_V, *Rattus norvegicus* voltage-gated calcium channel; TCa_V, *T. adhaerens* voltage-gated calcium channel.

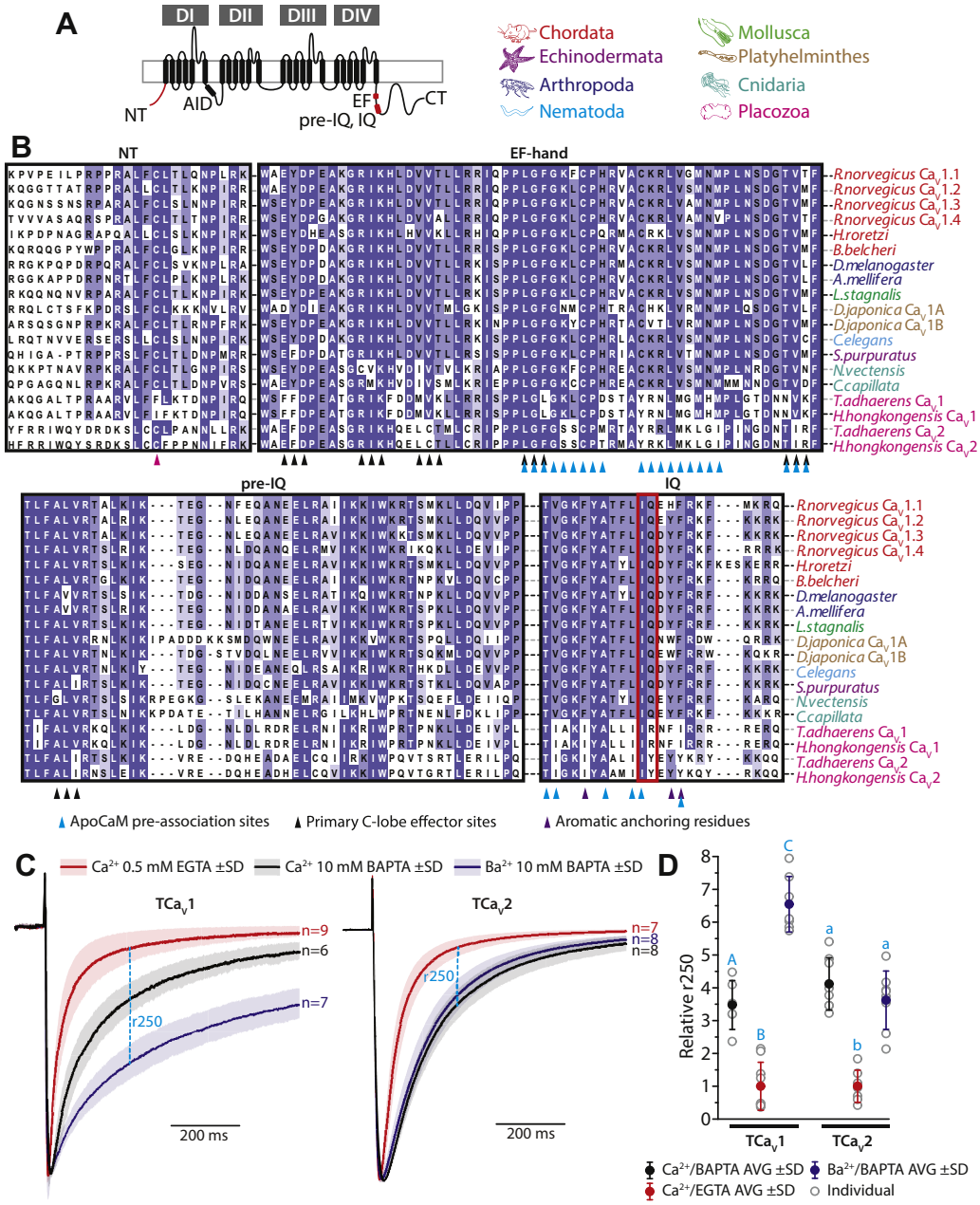

Figure 10. TCa_V1 and TCa_V2 channels undergo Ca^{2+}/calmodulin-dependent inactivation. *A*, *left*, illustration of the Ca_V1 channel protein highlighting regions that bear key residues for calmodulin regulation (*red*). *Right*, color-coding of phyla corresponding to the aligned Ca_V channel protein sequences shown in panel *B*. *B*, protein alignments of the N-terminal calcium-binding protein (CaBP) region and C-terminal EF hand domain, pre-IQ motif, and IQ motif from various Ca_V1 channel homologues, as well as the *T. adhaerens* and *H. hongkongensis* Ca_V2 channels. The *pink* chevron denotes a conserved cysteine residue within the CaBP region involved in N-lobe Ca^{2+}/calmodulin-dependent inactivation of $Ca_V1.2$ channels (14). *Blue* chevrons denote amino acid positions required for preassociation of apocalmodulin (ApoCaM) to $Ca_V1.3$ channels (83), *black* chevrons denote amino acid positions determined to be effector sites for calmodulin C-lobe dependent inactivation of $Ca_V1.3$ channels (83), and *purple* chevrons denote conserved aromatic amino acids in the IQ regions of $Ca_V1.2$ and $Ca_V2.1$/$Ca_V2.3$ channels identified as anchor points for calmodulin binding in X-ray crystallography studies (84–86). The red box delineates the namesake IQ motif present in the IQ region of most Ca_V1 channels. *C*, average normalized macroscopic Ca^{2+} and Ba^{2+} currents of TCa_V1 and TCa_V2 channels (±SD), with either 0.5 mM EGTA or 10 mM BAPTA in the internal solution. Both TCa_V1 and TCa_V2 exhibited CDI with 0.5 mM EGTA that was disrupted with 10 mM BAPTA, but only TCa_V1 channels retained an additional buffer-resistant CDI that became evident after replacing external Ca^{2+} with Ba^{2+}. The location of residual current at 250 ms into the voltage step (r250) is indicated by the *cyan-colored dashed lines*. *D*, average relative r250 values ±SD (*error bars*) of TCa_V1 and TCa_V2 channels in response to three different conditions: 5 mM external Ca^{2+} and 10 mM internal BAPTA (*black*), 5 mM external Ca^{2+} and 0.5 mM internal EGTA (*red*), or 5 mM external Ba^{2+} and 10 mM BAPTA (*purple*). Values were normalized against the average r250 observed using 0.5 mM internal EGTA and 5 mM external Ca^{2+} for each channel. *Uppercase* and *lowercase letters* denote within-group significant differences ($p \leq 0.001$) as determined by Holm–Sidak tests after one-way ANOVAs (Table S1). AID, alpha interaction domain; CT, C terminus; DI to DIV, domains I to IV; NT, N terminus; TCa_V, *T. adhaerens* voltage-gated calcium channel.

Also noted earlier, $Ca_V1.2$ and $Ca_V1.3$ channels bear NSCaTE motifs at their N termini, which convert N-lobe mediated CDI into a local, buffer-resistant process (13). This motif is absent in vertebrate $Ca_V1.1$ and $Ca_V1.4$ channels, conserved in bilaterian invertebrate Ca_V1 channels, but absent in more early diverging Ca_V1 channels from cnidarians and

placozoans (15). Thus, NSCaTE appears to be a bilaterian innovation. However, alignment of an N-terminal region just downstream of the NSCaTE motif (Fig. 10, *A* and *B*) reveals deep conservation of second motif, termed NATE, that contributes to N-lobe conversion mediated by NSCaTE (14). We note the presence of a deterministic cysteine residue in all included bilaterian and cnidarian Ca_V1 channels and placozoan Ca_V2 channels, identified as a secondary binding site for CaM within the NATE motif. Notably however, placozoan Ca_V1 channels lack this cysteine but, like most Ca_V1 channels, bear conserved proline (P) residues that flank this particular amino acid position, which would similarly impact the local secondary structure (Fig. 10*B*).

We sought to determine whether the TCa_V1 and TCa_V2 channels are regulated by CaM and if they differ in their regulation, like their bilaterian orthologues. In the presence of low intracellular Ca^{2+} buffering (*i.e.*, 0.5 mM EGTA) with 3 mM Ca^{2+} as the permeating cation, voltage steps from −100 to 0 mV produce relatively fast inactivating currents for both TCa_V1 and TCa_V2 (Fig. 10*C*). Similar experiments, but with strong intracellular buffering that would selectively disrupt N-lobe modulation, resulted in decreased TCa_V1 and TCa_V2 channel inactivation consistent with a loss of CDI (Fig. 10*C*). The decrease in channel inactivation was quantified by determining the amplitude of residual current relative to peak at 250 ms into the voltage step (r250), normalized against the average r250 observed using 0.5 mM internal EGTA and 5 mM external Ca^{2+} for each channel (Fig. 10*D*). Compared to 0.5 mM EGTA, 10 mM BAPTA caused the average r250 values of TCa_V1 and TCa_V2 to increase from 1.0 ± 0.7 and 1.0 ± 0.5 to 3.5 ±0.7 and 4.1 ±0.8, respectively (Fig. 10*D*; $p \leq 0.001$ for Holm–Sidak tests after one-way ANOVAs; $p \leq 0.001$ and $F \geq 35.9$ for all comparisons; Table S1). Subsequently, switching external Ca^{2+} with equimolar Ba^{2+} caused a significant slowing of TCa_V1 current inactivation, with the average relative r250 value increasing to 6.6 ± 0.8 ($p \leq 0.001$ for Holm–Sidak tests after one-way ANOVA), while TCa_V2 showed no difference, with an r250 value of 3.6 ± 0.9. Notably, switching from Ca^{2+} to Ba^{2+} did not impact the activation properties of TCa_V1, with the current–voltage relationship showing a similar peak at 0 mV (not shown). The loss of this additional CDI component in the presence of Ba^{2+} indicates that the TCa_V1 channel is uniquely subject to buffer-resistant CDI, which given the absence of NSCaTE and NATE motifs is most likely due to C-lobe regulation. Thus, like in bilaterians, the TCa_V1 and TCa_V2 channels exhibit differential regulation by CaM, indicating that this divergence in modulatory control most likely evolved in the common ancestor of placozoans, cnidarians, and bilaterians, shortly after the emergence of these two channel types in early animals.

To confirm that the observed CDI processes were indeed mediated by CaM, we conducted a series of experiments employing a mutant CaM (CaM_{1234}), which lacks the ability to bind Ca^{2+} (12). Previously, it has been documented that HEK-293T cells endogenously express CaM and that overexpression of this mutant form outcompetes the WT protein to prevent its regulation of Ca_V channels, disrupting the CDI process (83). For these experiments, we employed a classical approach that compares the amplitude of currents elicited by a test pulse as a function of various prepulses to different depolarizing voltages (87). Thus, the membrane was depolarized to various voltages ranging from −50 mV to +90 mV (*i.e.*, the prepulses), and after a brief repolarization to −100 mV, a subsequent test pulse was taken to +5 mV (Fig. 11*A*). For TCa_V1, TCa_V2, and $rCa_V1.2$ channels, the depolarizing prepulses elicited increasing amounts of Ca^{2+} to enter the cell, as more channels became activated, subsequently declining with a loss of driving force for Ca^{2+} influx and saturation of channel activation (Fig. 11, *B*, *D* and *F*). In the presence of endogenous (wt) CaM, the peak current amplitude elicited by test pulses produced classic U-shaped relationships when plotted as a function of prepulse voltages (Fig. 11, *C*, *E* and *G*), attributable to a combination of CDI caused by Ca^{2+} influx and VDI that increases with stronger depolarization. At more depolarized voltages where Ca^{2+} influx began to decline, test-pulse current amplitudes recovered, attributable to a loss of the CDI effect. The smallest test pulse currents occurred after prepulses of +20 mV for TCa_V1, 0 mV for TCa_V2, and +10 mV for $rCa_V1.2$, where the average current amplitudes decayed to 23.5 ± 0.1%, 22 ± 0.1%, and 27 ± 0.1% of the initial maximum current, respectively. Importantly, cotransfection of mutant CaM_{1234} completely disrupted CDI for all channels, isolating the VDI component (Fig. 11, *C*, *E* and *G*). Here, the currents only decayed to 59 ± 0.01% for TCav1, 58 ± 0.1% for TCa_V2, and 79 ± 0.1% of the initial current at the noted peak prepulse voltages. In general, the current decay was significantly greater at most voltages in the presence of WT CaM compared to CaM_{1234} ($p \leq 0.025$ for Holm–Sidak tests after two-way ANOVAs; $p < 0.001$ and $F \geq 7.0$ for all comparisons; Table S1). Only when the voltage steps reached +50 to +70 mV was the difference between mutant and WT CaM not significant, where only VDI is apparent. This indicates that CaM can modulate the inactivation of all three channels in a Ca^{2+}–dependent manner.

In addition to modulating inactivation, CaM was also able to alter TCa_V channel current density. Whereas the $rCa_V1.2$ channel current density was not significantly different with WT CaM (−9.3 ± 4.7 pA/pF) and CaM_{1234} (−6.2 ± 5.1; $p = 0.233$ with a two-tailed *t* test), TCa_V1 current density increased when CaM_{1234} was overexpressed (WT CaM = −5.9 ± 4.0 pA/pF; CaM_{1234} = −19.4 ± 10.2 pA/pF; $p < 0.001$ after a two-tailed *t* test), whereas TCa_V2 current density decreased with CaM_{1234} (WT CaM = −14 ± 5.0 pA/pF; CaM_{1234} = −4.5 ± 3.9 pA/pF; $p = 0.002$ after a two-tailed *t* test). The effect of CaM on TCa_V2 current density has been reported previously for other channels (88, 89), but its effect on TCa_V1, to our knowledge, has not been observed. Whether the increased current density with CaM_{1234} is due to a change in TCa_V1 cell surface expression or channel open probability will have to be followed up in a future study.

TCa_V1 is not subject to direct regulation by G proteins in vitro

Previously, we documented that the TCa_V2 channel lacks a key functional feature that is unique to its bilaterian Ca_V2

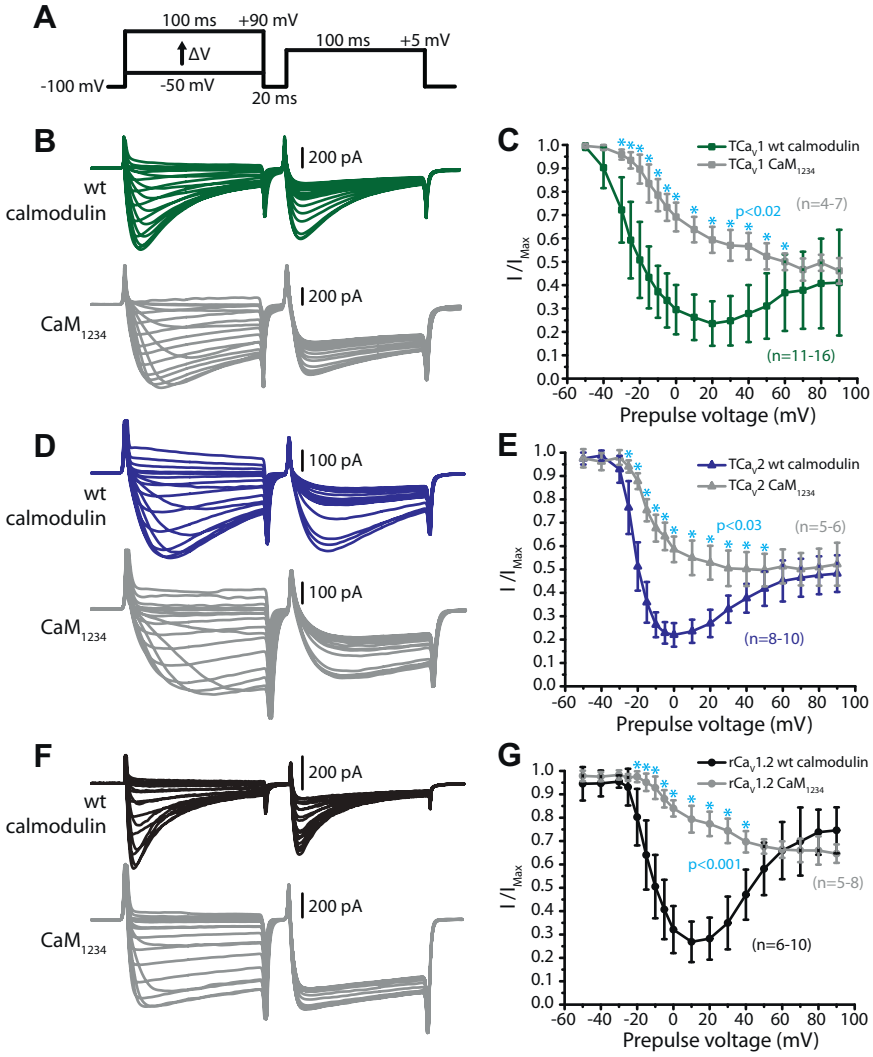

Figure 11. Voltage-dependent and calcium-dependent inactivation are two separate processes in TCa_V1, TCa_V2, and $rCa_V1.2$ channels. *A*, protocol used to examine calcium-dependent inactivation. Prepulse voltage steps from −50 mV to +90 mV caused an influx of varying amounts of Ca^{2+} into the cell, after which test pulses to +5 mV were used to measure the effect of Ca^{2+} influx on peak current amplitude. *B*, *top*, sample macroscopic Ca^{2+} current traces from TCa_V1 with endogenous, wildtype (wt) calmodulin, or *bottom*, co-expressed with mutant CaM (CaM_{1234}). *C*, plot of average TCa_V1 current amplitudes ±SD (*error bars*) elicited by the test pulse expressed relative to the prepulse voltage. *D*, sample current traces illustrating the effect of wt calmodulin (*top*) and CaM_{1234} (*bottom*) on peak inward TCa_V2 Ca^{2+} currents. *E*, plot of average TCa_V2 current amplitudes ±SD elicited by the test pulse over the prepulse voltage. *F*, sample current traces illustrating the effect of wt calmodulin (*top*) and CaM_{1234} (*bottom*) on peak inward $rCa_V1.2$ Ca^{2+} currents. *G*, plot of average $rCa_V1.2$ current amplitudes ±SD elicited by the test pulse over the prepulse voltage. For all plots, asterisks denote significant differences ($p < 0.03$) between TCa_V1, TCa_V2, or $rCa_V1.2$ current amplitudes as determined by Holm–Sidak tests after a two-way ANOVAs (Table S1). rCa_V, *Rattus norvegicus* voltage-gated calcium channel; TCa_V, *T. adhaerens* voltage-gated calcium channel.

orthologues, namely direct inhibition by G protein βγ proteins (5). G protein regulation of Ca_V2 channels permits control of Ca^{2+} influx at synapses and other cellular compartments through G protein–coupled receptors and their neuromodulatory ligands (90). Interestingly, the cloned *Trichoplax* Gβγ proteins inhibit the human $Ca_V2.1$ channel *in vitro*, indicating that the absence of regulation for TCa_V2 is likely due to structural features of the α_1 subunit and not the G proteins. Here, we sought to rule out G protein regulation of the TCa_V1 channel, by conducting a similar set of *in vitro* experiments as done previously for TCa_V2. We find no evidence for direct Gβγ inhibition of TCa_V1 (Fig. S5), suggesting that this unique form of regulation evolved strictly in bilaterians.

Discussion

On the phylogeny and evolution of Ca_V channel α_1 subunits

In this study, we complete the initial characterization of Ca_V channel α_1 subunits from *T. adhaerens* from the most early diverging phylum where Ca_V1, Ca_V2, and Ca_V3 channels co-exist. *Trichoplax* is only the third invertebrate species for which this has been done, the other two being the mollusc snail *L. stagnalis* (16, 50, 91) and the arthropod honeybee *Apis melifera* (92). The two most early diverging animal phyla, Porifera (sponges) and Ctenophora (comb jellies) (Fig. 1*C*), independently lost Ca_V3 channels and lack Ca_V1 channels (ctenophores and sponges) and Ca_V2 channels (sponges) (4, 5). Sponges are therefore unique among animals in that they lack

Ca_V1 to Ca_V3 channels, possessing instead a $Ca_V1/2$ channel also found in premetazoan single-celled choanoflagellates like *Salpingoeca rosetta* (4). Because of its phylogenetic sister relationship and shared structural features with Ca_V1 and Ca_V2 channels (Fig. S1) and apparent premetazoan origin, the $Ca_V1/2$ type channel is proposed to have given rise to Ca_V1 and Ca_V2 channel types *via* one or more gene duplication events, early on in animal evolution (4, 5). Nevertheless, we lack an understanding of precisely when and in which animal lineages these evolutionary events took place. Confounding the matter is the unresolved placement of either sponges or ctenophores as the most early diverging animals on the metazoan phylogenetic tree. That is, whereas numerous phylogenomic studies suggest that ctenophores are the most early diverging (28, 93, 94), others support the classic morphology-based view that sponges are (95, 96). Perhaps, the most parsimonious explanation for Ca_V channel evolution in animals comes about if we consider sponges as the most early diverging. Here, the duplication of a $Ca_V1/2$ channel gene that gave rise to Ca_V1 and Ca_V2 channels could have occurred after sponges diverged, in the common ancestor of ctenophores, placozoans, cnidarians, and bilaterians (Fig. 1*C*). Since ctenophores lack Ca_V1 channels, they would have lost this gene (in addition to Ca_V3 channels), retaining only a single Ca_V2 channel orthologue, while placozoans, cnidarians, and bilaterians all retained Ca_V1 to Ca_V3 channels.

Our analysis of the TCa_V1 protein sequence revealed deep conservation of hallmark structural features conserved among Ca_V1, Ca_V2, and $Ca_V1/2$ channels (Figs. 1, 10 and S1). This includes ion selectivity filter motifs of EEEE (EDEE for the *S. rosetta* $Ca_V1/2$), voltage sensor S4 helices with positively charged lysine and arginine amino acids, and structures for interacting with the $Ca_V\beta$ (AID) and $Ca_V\alpha_2\delta$ subunits (domain 1 S1–S2 loop). Indeed, although transmembrane regions tend to be well conserved when comparing Ca_V1 channels across phyla, most of the cytoplasmic linkers and N and C termini are extremely divergent (Fig. 1*F*), and this is also the case for Ca_V2 and Ca_V3 channels (5). This is significant because these cytoplasmic regions, which are generally devoid of secondary structure, are often sites for unique modulation of the α_1 subunit by cytoplasmic factors including interacting proteins and kinases (97–100). Thus, modulation at these divergent loci might be very different among channel orthologues from different phyla. Still, there is evidence that stretches of intrinsically disordered, highly divergent protein sequences might nevertheless harbor conserved functional short linear motifs that are difficult to identify *via* sequence alignment (101), or cryptic molecular signatures that are not apparent in sequence alignments at all (*e.g.*, length, amino acid composition, net charge) (102).

We also found the C-terminal EF-hand, pre-IQ, and IQ domain structures to be present in the TCa_V1 channel protein (Figs. 10*B* and S1), indicative of regulation by the Ca^{2+} sensor protein CaM. These structures are also found in Ca_V2 channels (5) and $Ca_V1/2$ channels from *S. rosetta* (Fig. S1) and the sponge species *Amphimedon queenslandica*, *Haliclona tubifera*, and *Haliclona ambioensis* (not shown) (103, 104). Indeed, the IQ domain is fairly ubiquitous among eukaryotic four-domain channels, with few exceptions (*e.g.*, Ca_V3 and sodium leak channels) (1), suggesting that CaM regulation and/or signaling is an ancient invention of broad physiological significance. Early diverging Ca_V1 channels from non-bilaterians, including TCa_V1, lack an NSCaTE motif (Fig. S1), a noted secondary binding locus for CaM shared among vertebrate and bilaterian invertebrate Ca_V1 channels (15). TCa_V1 also lacks a key a cysteine residue in the reported NATE motif (13), just downstream of NSCaTE, that independently mediates interactions with CaM (Fig. 10*B*) (14). On the other hand, the cnidarian homologues possess a NATE-like motif and so do placozoan Ca_V2 channels despite some divergence a few amino acids positions upstream (Fig. 10*B*). Whether CaM binds to the NATE region in invertebrate channels has not been determined, so the significance of this apparent conservation is unclear.

TCa_V1 sheds light on the distinguishing biophysical features of Ca_V1 to Ca_V3 channels

Altogether, the functional properties of the TCa_V1 to TCa_V3 channels point to an early establishment of several unique biophysical features that distinguish these three calcium channel types from each other, the most obvious being activation voltages where TCa_V3 classifies as an low-voltage–activated channel (24) and TCa_V1 and TCa_V2 as HVA channels (Fig. S4, *A* and *B*) (5). Within the literature, reported biophysical parameters of vertebrate Ca_V channels come from a multitude of studies, each employing different recording solutions and conditions, channels cloned from different tissues and subject to alternative splicing, and co-expressed with different $Ca_V\beta$ and $Ca_V\alpha_2\delta$ subunits (vertebrates possess four of each (105)), all of which can significantly impact biophysical properties. Hence, a broad phylogenetic comparison of reported parameters cannot be done with confidence. However, because our characterization of TCa_V1 and TCa_V2 was done alongside rat $Ca_V1.2$ and human $Ca_V2.1$ channels, using the same subunits and recording conditions, we can compare these channels to each other with more confidence. Table 1 is a summary of the biophysical properties of the four channels, revealing that comparisons between TCa_V1 *versus* TCa_V2 and $rCa_V1.2$ *versus* $hCa_V2.1$ are similar for most parameters, except for steady-state inactivation and deactivation. Thus, when considering only these four homologues, it appears as though some core biophysical distinctions between the mammalian Ca_V1 and Ca_V2 channels hold true for the *Trichoplax* homologues, although they are by no means striking.

In general, the most striking functional divergence of the three *Trichoplax* Ca_V channels pertains to their voltage sensitivity, where all three exhibit hyperpolarized voltages for activation and inactivation compared to their mammalian orthologues (5, 24). Thus, it is important to consider putative structural features that might account for these differences. For mammalian $Ca_V1.1$ to $Ca_V1.4$ channels, several disease-causing point mutations have been identified that cause left-shifted voltage properties (reviewed in (106)); however,

TCa_V1 does not possess any sequence differences at these positions (Fig. S1). TCa_V1 also bears a conserved signature of two glutamate and one aspartate residues within the AID structure, which when mutated in $Ca_V1.2$ causes hyperpolarized gating properties (107) (Fig. S1). Notably, TCa_V1 lacks an optional exon equivalent to conserved exons 29, 33, and 32 in $Ca_V1.1$ to $Ca_V1.3$ channels, respectively, that encode small inserts in the DIV extracellular S3–S4 loop (Figs. S1 and S6). For all three of these mammalian channels, exclusion of this optional exon imposes left-shifted voltage sensitivity (108–110), for example, hyperpolarizing the activation and inactivation of $Ca_V1.2$ by more than 10 mV. Because the TCa_V1 channel resembles the Δ exon 33 variant of $rCa_V1.2$, the noted differences in gating could perhaps be in part attributable to this particular structural difference, given that the $rCa_V1.2$ channel used in our electrophysiology experiments possessed exon 33.

Clearly, an important next step will be to explore how the single *Trichoplax* $Ca_V\beta$ and two $Ca_V\alpha_2\delta$ subunits impact the functional properties of the *Trichoplax* Ca_V channels and furthermore, to determine whether the CACHD1 and $\alpha_2\delta$-like proteins also play a role in regulating the α1 subunits (Fig. 2). Indeed, ancillary subunits can impose striking deviations from canonical ion conducing properties, in lieu of structural or functional alterations to the α_1 subunit. For example, *in vitro* expression of the Ca_V2a channel from the sea anemone *N. vectensis* with its native $Ca_V\beta$ subunit produces highly atypical macroscopic currents with extremely left-shifted steady-state inactivation properties, such that the channel population is completely inactivated at a typical resting membrane potential of −60 mV (111). Because the *Nematostella* $Ca_V\beta$ subunit exerts the same effect on human $Ca_V2.1$, the observed adaptation must have occurred *via* structural changes in the ancillary subunit. Similarly, the $Ca_V\beta B$ subunit from the parasitic flatworm *Schistosoma mansoni* imposes a hyperpolarizing shift in the steady-state inactivation of the human $Ca_V2.3$ channel (112), coupled with significant rundown of macroscopic current amplitude (113). Given these and other similar observations, the biophysical properties of the TCa_V1 channel reported here should be interpreted with caution, until the effects of cognate ancillary subunits are determined.

Here, as we did previously for TCa_V2 (5), we have shown that TCa_V1 channel protein expression is significantly increased upon co-expression with the rat $Ca_V\beta_{1b}$ and $Ca_V\alpha_2\delta_1$ subunits *in vitro* (Fig. 3, *B–D*), like vertebrate and bilaterian invertebrate HVA channels (50, 51, 53). Given our inability to record TCa_V1 currents *in vitro* without the co-expressed $Ca_V\beta_{1b}$ subunit and the ability to do so when $Ca_V\alpha_2\delta_1$ was excluded, it appears as though the $Ca_V\alpha_2\delta$ subunit plays a small role in membrane trafficking of the *Trichoplax* channel. This is in contrast to vertebrate Ca_V channels, where $Ca_V\alpha_2\delta$ significantly enhances membrane expression (53). Perhaps, this could be due to a structural divergence between the rat and *Trichoplax* proteins, such that the rat $Ca_V\alpha_2\delta_1$ subunit has a low affinity for the TCa_V1 channel. In accordance, we found that in some cells, the TCa_V1 currents were considerably right shifted in their voltage properties, resembling those conditions when the rat $Ca_V\alpha_2\delta_1$ was excluded from the transfections (Fig. 5, *E* and *F*). Although less common, the occurrence of these events might suggest that the affinity between the channel and the subunit is weak, such that cells co-expressing low levels of $Ca_V\alpha_2\delta_1$ would be enriched with membrane channels lacking this subunit. Nevertheless, comparing TCa_V1 channel currents with and without rat $Ca_V\alpha_2\delta_1$ revealed that the subunit caused a hyperpolarizing shift in voltage properties and increased sensitivity to voltage changes, as is observed for vertebrate Ca_V channels (53). Clearly, a more complete picture about the comparative properties of the *Trichoplax* Ca_V channels will emerge once the biophysical properties of the different endogenous Ca_V channel complexes are known.

On the divergent modulation of Ca_V1 and Ca_V2 channels by CaM

One key distinguishing feature of bilaterian Ca_V1 and Ca_V2 channels is their differential regulation by CaM, where only Ca_V1 channels exhibit fast, buffer-resistant CDI that becomes apparent when the permeating ion is switched from Ca^{2+} to Ba^{2+}. Here, we sought to explore whether the TCa_V1 and TCa_V2 channels are subject to CaM regulation and whether they exhibit the same functional distinction. Indeed, both channels were found to exhibit CDI, evident in the slowing of current inactivation when the intracellular recording solution was switched from one containing 0.5 mM EGTA, a permissive condition that does not disrupt CaM Ca^{2+} binding, to 10 mM BAPTA, a strong buffering condition that selectively disrupts Ca^{2+} binding at the N-lobe, but not the C-lobe of CaM (Fig. 10*C*). A direct role for CaM was established by co-expression of a mutant CaM lacking the ability to bind Ca^{2+}, which completely abrogated the CDI process for the *Trichoplax* Ca_V1 and Ca_V2 channels, as well as the $rCa_V1.2$ channel (Fig. 11). Thus, CaM regulation of HVA Ca_V channels is likely an ancestral feature, inherited from the parental $Ca_V1/2$ channel that gave rise to these two channel types and consistent with the noted ubiquity of IQ domain structures among eukaryotic four-domain channels, including the more distantly related Na_V channels which are subject to CaM regulation and CDI (114).

Interestingly, switching the permeating cation from Ca^{2+} to Ba^{2+} cased a dramatic reduction in TCa_V1 inactivation, with no effect on TCa_V2 (Fig. 10*C*), consistent with exclusive buffer-resistant CDI for the placozoan L-type channel. Given the noted absence of NSCaTE and NATE motifs in the TCa_V1 N terminus (Figs. 10*B* and S1), the most likely explanation is that this unique component of the CDI process is mediated by the C-lobe of CaM. In the presence of Ba^{2+}, the TCa_V1 channel inactivation is dramatically slowed, suggesting that at least for a voltage step to 0 mV, CDI accounts for a large portion of channel inactivation, with a diminished contribution from VDI compared to TCa_V2. Thus, TCa_V1 distinguishes itself from TCa_V2 in being less susceptible to VDI, rendering the channel population more sensitive to Ca^{2+} levels in the cytoplasm, rather than alterations in membrane voltage. Perhaps, this key

distinction between Ca_V1 and Ca_V2 channels, conserved in placozoans, played a central role in their differential adaptation for different Ca^{2+} signaling roles in the evolving neuromuscular system. Going forward, future studies on $Ca_V1/2$ channels from choanoflagellates and sponges might reveal whether the unique regulation of Ca_V1 channels by CaM preceded the emergence of Ca_V1 and Ca_V2 channels and was subsequently lost in Ca_V2 channels, or rather, is a unique adaptation of Ca_V1 channels.

Physiological functions of Ca_V channels in the placozoa

In vertebrates, the different Ca_V channel types exhibit notable differences in their tissue/cell-type expression patterns. Generally, Ca_V2 channels are restricted to neurons and neuroendocrine cells, while Ca_V1 and Ca_V3 channels are expressed more broadly, also found in smooth and cardiac muscle (Ca_V1 and Ca_V3) and skeletal muscle (Ca_V1) (2, 105, 115). In *Lymnaea*, similar patterns are apparent where Ca_V2 channel expression is restricted to the nervous system and neuroendocrine glands, while Ca_V1 and Ca_V3 channels are additionally expressed in the heart, as well as muscular structures of the mouth and foot (7, 116). Thus, another feature of bilaterian Ca_V channel orthologues that appears to be deeply conserved is their differential tissue/cell-type expression. Using a custom antibody, we show here that the TCa_V1 channel is expressed in dorsal epithelial cells within the interior of the animal (*i.e.*, the lipophil zone) (Fig. 4). Although *Trichoplax* lacks true muscle (18), their dorsal epithelium is made up of fast-contracting cells that require cytoplasmic Ca^{2+} influx for contraction, akin to myocytes (57). Accordingly, placozoans possess most genes necessary for driving Ca^{2+}-dependent actin–myosin contractions in other animals (117). Given the uncovered expression of TCa_V1 in these cells, it may be that the channel contributes to excitation–contraction coupling, similar to its bilaterian counterparts. Similarly, we show here that, similar to vertebrates and the snail, all three Ca_V channels are co-expressed in neuroendocrine-like type II gland cells (Fig. 4), which express the molecular machinery required for regulated exocytosis (*e.g.*, SNAP-25, synapsin, and complexin) (18, 56) and a small endomorphin-like peptide that is secreted by these cells to control ciliary locomotion (56, 118). Additionally, gland cells are teardrop/hourglass shaped (56), oriented longitudinally toward the outside edge of the animal, perhaps indicative of cellular polarity with a region specialized for vesicle exocytosis. This is certainly suggested by the immunolocalization of TCa_V2 channel along the outward facing edge of these cells (5). We also previously documented weak expression of TCa_V2 in fiber cells, which are situated between the dorsal and ventral epithelium of the animals, although this was not observed in all preparations. Here, using fluorescent probes, we also detected the TCa_V2 mRNA in fiber cells (5), and not TCa_V1 (Fig. 4, *L* and *M*). However, this labeling was weak and infrequent, and altogether, it is difficult to state with certainty that TCa_V2 is significantly expressed in fiber cells. Recently, fiber cells were shown to mediate innate immunity and wound healing and to express gene markers homologous to macrophage cells (60). Lastly, immunofluorescence and *in situ* hybridization experiments indicate that TCa_V1 is expressed in both dorsal and ventral epithelial cells (Fig. 4, *E*, *F* and *I–K*); however, antibody staining suggests the protein is more abundant in the dorsal epithelium. We note that the antibody labeling was completely blocked after preadsorption with the corresponding protein epitope (Fig. 4*D*), which was consistent with our Western blotting experiments (Fig. 3*F*), indicative of specific labeling of the TCa_V1 protein. In summary, although the expression patterns of the *Trichoplax* Ca_V channels are suggestive of cellular transcriptional homology, more work needs to be done to better understand the evolutionary relationship of *Trichoplax* cells to those of other animals and on the transcriptional programs that controls the expression of the *Trichoplax* channels in different cell types.

A key question of course is how membrane excitation and electrical signaling serves to recruit *Trichoplax* Ca_V channel activity and in turn influence their contributions to cellular physiology. Placozoans have recently been demonstrated to fire rapid, Na^+-based APs lasting 1 to 3 ms at a frequency of ~130 Hz (21). These recordings were performed using extracellular electrodes on immobilized whole animals and isolated gravity-sensing crystal cells (21), indicating that there is at least one type of excitable cell in the animal. These findings suggest that *Trichoplax* Ca_V channels may experience, and open in response to, high-frequency APs. Mammalian Ca_V1 and Ca_V2 channels differ in their response to high-frequency depolarizations (119). *In vitro* recordings applying voltage waveforms that resembled hippocampal neuron APs showed that $Ca_V2.1$ channels caused less cumulative Ca^{2+} entry into the cell and greater current decay over time compared to $Ca_V1.2$ channels (120). Thus, in mammals, there is a clear difference in response of Ca_V1 and Ca_V2 channels to the same repetitive AP stimulus. Here, we wanted to determine if the TCa_V1 and TCa_V2 channels also differ in this respect. Applying short, repetitive depolarizations to both channels revealed surprisingly little difference (Fig. 8). Both the cumulative Ca^{2+} entering the cell and the activity-dependent decay in peak current after 1 s of 100 Hz stimulation were similar between TCa_V1 and TCa_V2. Therefore, the differences in biophysical properties and kinetics seen between TCa_V1 and TCa_V2 channels with prolonged depolarizations (>100 ms) did not translate to differences in Ca^{2+} influx with short, repetitive depolarizations. Even though placozoan APs were reported to fire at a frequency of ~130 Hz, it is possible for APs to be modulated to become slower or faster (121). Therefore, we next examined the combined effects of different depolarization lengths and frequencies on the TCa_V1 and TCa_V2 channels. With increased depolarization frequency, both channels exhibited a decay in current amplitude, but there was very little difference between TCa_V1 and TCa_V2. The only difference in current decay that could be observed was at 100 Hz with 3 ms-long pulses. Perhaps, more striking differences would emerge in experiments using varying baseline holding voltages. Indeed, the left-shifted inactivation curve of TCa_V1 relative to TCa_V2 (Fig. S4*B*) suggests that this channel contributes minimally to excitation-induced Ca^{2+} influx when the resting voltage is

more positive than −50 mV. In this respect, the population of available TCa_V1 channels in a cell could be dynamically regulated by altering resting membrane voltage. For example, if co-expressed with TCa_V2, the TCa_V1 channel population could be utilized as a reserve pool that only becomes available after a bout of membrane hyperpolarization, in a process akin to postinhibitory rebound excitation. Future studies examining the excitability of cell types expressing TCa_V1 and TCa_V2 channels would help identify the voltage changes that these channels are experiencing.

Conclusions

Duplication of an ancestral $Ca_V1/2$ channel into separate Ca_V1 and Ca_V2 channels allowed them to acquire variations in sequence and diverge in their biophysical properties and protein interactions. Differences in biophysical properties may have made these channels better suited for activating certain Ca^{2+} signaling pathways, whereas the expansion of Ca_V channel protein interactions may have facilitated the distinct modulation and subcellular localization of Ca_V1 and Ca_V2 channels. Collectively, these changes likely resulted in Ca_V channels taking on conserved yet distinct roles across many extant animal phyla. *Trichoplax* Ca_V1 and Ca_V2 channels may represent a more ancestral form of these channels seeing as they have some, but not all, of the features present in Ca_V channels of more derived animals. Differences in their cellular expression, biophysical properties, and modulation suggests that they play different roles in the animal. However, whether they have distinct excitation-secretion or excitation-transcription/excitation-contraction coupling capabilities as seen in other animals will need to be investigated further. Future work on the functions of these channels *in vivo* (*e.g.*, through knockdown and behavioral assays) could help reveal the roles of TCa_V1 and TCa_V2 channels in *Trichoplax* cells.

Experimental procedures

All animal studies were approved by the University of Toronto Research Oversight and Compliance Office.

Sequencing and synthesis of full-length Trichoplax Ca_V1 channel cDNA for in vitro *expression*

A putative full-length protein-coding sequence of the *Trichoplax* Ca_V1 channel was identified within the *T. adhaerens* mRNA transcriptome (GenBank accession number GHJI00000000) (20). To determine a consensus coding sequence, we used nested gene-specific primers (Table 2) to PCR amplify, clone, and sequence the N- and C-terminal halves of the TCa_V1 channel cDNA, in triplicate, from a whole-animal cDNA library. The resulting full-length TCa_V1 consensus coding sequence was submitted to GenBank with accession number MW915585. The sequence was subsequently provided to GenScript for gene synthesis employing codon optimization for expression in human cells, flanked by SacII and BamHI restriction sites for cloning into the pIRES2-EGFP and pEGFP-C1 mammalian expression vectors (Clontech), and a Kozak sequence of GCCACCATGG flanking the start codon for efficient translation of the channel *in vitro* (122).

Table 2
Sequences of primers used for cloning the *Trichoplax* Ca_V1 channel cDNA

Primer name	Sequence (5 - 3′)
TCa_V1_NT_F1	TTATTCACAGTACGTGTTTTGTAGAGC
TCa_V1_NT_F2	ATGGCTGATGATAAAGTAGGCACAG
TCa_V1_NT_R1	CAATAACGAAGCCAACAAATATGTTTACC
TCa_V1_NT_R2	TACGAGGGGTTGGTGATTTCTACTAGG
TCa_V1_CT_F1	ACGGAAGCTGGCCGAGGACCTAG
TCa_V1_CT_F2	CCAACCCCTCGTAGCGATCTACTTCG
TCa_V1_CT_R1	AAAGTAAGTAGATCAATCCAAGAATAGG
TCa_V1_CT_R2	GATCAATTATACGACTGACACTC

In silico phylogenetic inference and sequence alignments

Ca_V subunit protein sequences were extracted from select NCBI gene databases using the BLAST program (123) using human sequences as query, with the exception of the placozoan and cnidarian homologues which were extracted from available genome and transcriptome resources (20, 40, 41). All identified sequences that produced BLAST Expect value alignment scores below 1E-6 were subsequently analyzed via reciprocal BLAST of the NCBI Landmark Database, in order to filter out sequences with higher similarity to non-Ca_V subunit proteins. Accession numbers and protein sequences for all identified Ca_V channels and ancillary subunits are provided in File S1, with the exception of the Ca_V1 channel sequence from *A. pallida*, for which an accession was not available, and included sequences were copied directly from a published figure (124). All protein sequence alignments were generated with the program MUSCLE (125) using default parameters. Alignments were visualized and annotated with JalView, version 2.11.1.0, (126) and Adobe Illustrator CS6. Bioinformatic prediction of transmembrane helices of the TCa_V1 channel was done using the Phobius web server (127), and the plot of sequence conservation (EBLOSUM62 score) for aligned representative Ca_V1 channel protein sequences was done using EMBOSS Plotcon (128) using a window size of 11 aligned positions. Predictions of conserved sites and domains were done using the software InterProScan (129). All maximum likelihood phylogenetic trees were inferred from protein alignments of selected protein sequences, trimmed with the program trimAl (130) using gap thresholds of 95% (for $Ca_V\alpha_1$ subunits), 70% (for $Ca_V\beta$ subunits), and 60% (for $Ca_V\alpha_2\delta$ subunits). Best fit model selection and phylogenetic inference was done using IQ-Tree (131), with node support values generated *via* 1000 ultrafast bootstrap replicates and the models LG+R5 (for $Ca_V\alpha_1$ subunits), JTT+R3 (for $Ca_V\beta$ subunits), and WAG+F + R6 (for $Ca_V\alpha_2\delta$ subunits) selected according to Bayesian Information Criterion.

Imaging and quantification of EGFP fluorescence

For quantification of EGFP fluorescence, HEK-293T cells were transfected in triplicate using 1 μg of $pTCa_V1$-IR-EGFP with 0.5 μg of Kir2.1 cDNA with or without 1 μg of rat $Ca_V\beta_{1b}$ and $Ca_V\alpha_2\delta_1$ subunits. The cells were incubated at 28 °C for

2 days and then imaged with transmitted and fluorescent light at 20x magnification, using a Zeiss AxioCam MRm Rev3 camera mounted on a Zeiss AxioObserver A1 inverted microscope. All micrographs were taken with the Zeiss ZEN Lite software using the same exposure settings. ImageJ software (132) was used to measure the integrated density and the cell confluency of the acquired fluorescence images. Integrated density values were normalized to the highest value for all replicate sets, averaged, and plotted.

Antibody synthesis

Polyclonal anti-TCa_V1 antibodies were generated in rabbits. The II-III linker of TCa_V1 (bases 2188–2550, residues 730–850; GenBank accession number MW915585) was expressed in BL21(DE3) *E. coli* as a C-terminal 6xHis fusion protein using the expression vector pET-28b(+) (Novagen). Transformed BL21 *E. coli* were grown to an optical density of 0.5 in 700 ml of Luria Bertani broth. Protein expression was induced with 0.5 mM isopropyl β-d-1-thiogalactopyranoside for 4 h, then cells were harvested by centrifugation at 4000*g* for 30 min and sonicated in lysis buffer (500 mM NaCl, 20 mM Tris-HCl 1 mM PMSF, 10% glycerol, 1 mg/ml lysozyme, pH 7.9). Lysed bacteria were centrifuged again at 12,000*g* for 30 min to separate the supernatant with soluble proteins from the pellet. His-tagged recombinant proteins were purified by Ni^{2+} affinity chromatography using Ni-NTA His-Bind Resin (EMD Millipore) according to manufacturer instructions, using a 20 mM imidazole column wash solution and 100 mM imidazole elution solution. After elution, the purified proteins were dialyzed with PBS (137 mM NaCl, 2.7 mM KCl, 10 mM Na_2HPO_4, and 1.8 mM KH_2PO_4, pH 7.4). Final yields averaged 0.5 mg/ml. Purified TCa_V1 II-III linker peptides were injected into rabbits, and rabbit serum was collected and used for Western blotting and immunostaining experiments. All reagents were obtained from MilliporeSigma.

Western blotting and immunohistochemistry

For Western blotting of *Trichoplax* proteins, ∼600 animals were lysed in 200 μl of chilled lysis buffer composed of 8 M urea, 50 mM ammonium bicarbonate, and a protease inhibitor cocktail (MilliporeSigma). Protein lysates of HEK-293T cells ectopically expressing TCa_V1 channels were prepared as described previously (5). In short, $pTCa_V1$-IR-EGFP was cotransfected into HEK-293T cells with pKir2.1, rat $Ca_V\beta_{1b}$, and $Ca_V\alpha_2\delta_1$ subunits as outlined below, and cells were incubated at 28 °C for 2 days to increase channel expression. HEK-293T cells were washed with PBS and lysed with 300 μl of 1% Nonidet P-40 lysis buffer (125 mM NaCl, 50 mM Tris base, 1.5 mM MgCl2, 5% glycerol, 1% NP-40, pH 7.4). Protein lysates were quantified using the BCA protein assay (Thermo), and 50 μg were electrophoretically separated on 4 to 12% Bis-Tris Gels (Invitrogen) and transferred onto nitrocellulose membranes. Membranes were then washed in TBS-T saline (10 mM Tris-Cl, 150 mM NaCl, 0.05% (v/v) Tween 20, pH 7.4) and blocked for 1 h at room temperature in TBS-T containing 5% skimmed milk powder. After blocking, the membranes were incubated overnight at 4 °C with either mouse monoclonal anti-EGFP antibodies (Cell Signaling Technologies) or custom rabbit polyclonal anti-TCa_V1 antibodies (1:4000 and 1:5000 dilution in 5% milk TBS-T, respectively). For Western blots of *Trichoplax* lysates, anti-TCa_V1 antibodies were used at a 1:4000 dilution. To confirm that the antibody was recognizing the protein of interest, antibodies were preadsorbed with immunization antigen in excess (1:5 mass ratio) overnight at 4 °C. Blots were incubated with goat anti-rabbit or goat anti-mouse secondary antibodies conjugated to horseradish peroxidase (Cell Signaling Technology; 1:2000 in 5% milk TBS-T) at room temperature for 1 h. Membranes were imaged following 1 to 5 min incubation in Clarity Western ECL Substrate (Bio-Rad). Ponceau staining of Western blots was done to confirm equal protein content among samples. Western blot analyses performed using custom anti-TCa_V1 antibodies were done using unpurified antibodies (terminal bleed serum). All indicated reagents were obtained from MilliporeSigma. Quantification of bands observed on Western blots was performed using ImageJ (132), standardized to corresponding total protein on lanes of Coomassie-stained gels.

For immunohistochemistry experiments, *Trichoplax* were frozen and freeze substituted as described previously (5, 18). In short, several *Trichoplax* were transferred to a drop of a 1:1 mixture of artificial seawater (ASW) and 1 M mannitol placed in the center of Superfrost Plus slides (Thermo Fisher Scientific) and left to adhere for 30 min. The liquid was then removed, and the slides were plunged into acetone on dry ice and kept at −80 °C overnight. The next day, slides with specimens were fixed in methanol with 1.6% paraformaldehyde for 2 h at −20 °C, then at room temperature for 1 h. Slides were then gradually rehydrated into PBS and blocked for 15 min in blocking buffer (3% goat serum, 2% horse serum, 1% BSA in PBS). After rehydration, specimens were incubated overnight at 4 °C with polyclonal rabbit anti-TCa_V1 antibody (terminal bleed serum) diluted 1:1000 in blocking buffer. Negative controls used preimmune serum or lacked anti-TCa_V1 antibody. The slides were subsequently incubated with a 1:500 dilution of Alexa Fluor 647 goat anti-rabbit secondary antibody (A-21245, Thermo Fisher Scientific) in blocking buffer for 4 h at room temperature. WGA and Alexa Fluor 555 conjugate (Themo Fisher Scientific) were added together with the secondary antibodies at a dilution of 1:200. Finally, slides were rinsed in PBS and mounted with ProLong Gold antifade reagent with DAPI (Invitrogen), and fluorescence micrographs were captured using an inverted LSM 880 confocal microscope (Zeiss) and merged using ImageJ software (132). Volocity Software (Quorum Technologies) was used to create three-dimensional renderings of confocal image stacks. To confirm that the antibody was recognizing the protein of interest, antibody was preadsorbed with immunization antigen in excess (1:10 mass ratio) overnight at 4 °C.

Fluorescence in situ *hybridization experiments*

In situ hybridization was performed on whole animals and dissociated cells with probes and reagents from Advanced Cell

Diagnostics. Whole animals were transferred to a 200 μl drop of ASW mixed in equal parts with 0.97 M mannitol (in water) on Superfrost Plus Gold glass slides (Fischer). After 2 h, the ASW/mannitol was removed, and the samples were frozen by plunging into tetrahydrofuran on dry ice and kept overnight. The slides were transferred to methanol containing 3% acetic acid at −20 °C for 30 min followed by methanol with 4% formalin, initially at −20 °C and then at room temperature, each for 30 min. The samples were rinsed twice in methanol, once in ethanol, dried for 5 min, and then treated with Protease IV for 30 min at room temperature.

Dissociated cells were prepared from animals incubated for 1 hr in calcium-free ASW (133) containing 2 mM EGTA (Sigma-Aldrich) and 0.25% trypsin (Gibco). The animals were rinsed twice in normal ASW, transferred to ASW mixed 1:1 with 0.97 M mannitol, and then triturated with a glass pipette until the suspension appeared homogeneous. Samples of the cell suspension were transferred to Superfrost Plus Gold glass slides (Thermo Fisher Scientific). The sample were kept at room temperature for 1 hr and then frozen by plunging into tetrahydrafuran on dry ice and kept overnight. The slides were transferred to methanol with 4% formalin initially at −20 and then at room temperature, each for 30 min. The samples were rinsed twice in methanol, once in ethanol, and rehydrated by incubation in 90%, 70%, and 50% ethanol in PBS, each for 5 min. The samples were rinsed twice with PBS and then treated with Protease III for 15 min at room temperature.

Hybridization was performed with an RNAscope Multiplex Fluorescent assay according to supplier's instructions using the following RNAscope probes: TCa_V1 (# 442461), TCa_V2 (#442471), TCa_V3 (#488711; 442481-C2), and *Trichoplax* FoxC (# 30534-C2). Samples were counterstained with WGA conjugated to CF405M (Biotium; 1:200 in PBS for 30 min) or DAPI (2 min), mounted in ProLong Gold antifade reagent (Invitrogen) and examined with an LSM 880 AiryScan confocal microscope (Carl Zeiss Microscopy LLC). Labeling with each probe was done at least twice; the results of independently repeated experiments were similar. Cell types in dissociated cell samples were identified based on their distinctive features: mucocytes by intense cytoplasmic WGA staining; dorsal epithelial cells by possession of small WGA-stained cortical granules; ventral epithelial cells by their columnar shapes; and fiber cells by their possession of a large autofluorescent inclusion or by expression of FoxC.

In vitro *expression of cDNAs and electrophysiological recording*

Detailed procedures for culturing and transfecting HEK-293T cells were described previously (24, 25, 74). For electrophysiological experiments, cultured cells in 25-cm^2 vented flasks were transiently transfected with either 1 μg of the $pTCa_V1$-IR-EGFP plasmid, 0.5 μg of the $rCa_V1.2$ plasmid (74), or 1 μg of the $pTCa_V2$-IR-EGFP plasmid (5), along with 1 μg each of the rat $Ca_V\beta_{1b}$ and $Ca_V\alpha_2\delta_1$ subunit cDNAs cloned into the mammalian expression vector pMT2 (61). In order to hyperpolarize the resting membrane potential of transfected HEK-293T cells below the window current range of the TCa_V1 channel, 0.5 μg of the mouse Kir2.1 inwardly rectifying potassium channel cDNA cloned into the expression vector pcDNA3.1 was included in all transfections (62). For experiments involving co-expression of the *Trichoplax* and rat Ca_V channels with a nonfunctional CaM bearing four mutant EF hand motifs (CaM_{1234}), the expression plasmid $pCaM_{1234}$-IR-EGFP (Addgene) was modified to exchange and replace the EGFP coding sequence with that of the red fluorescent protein DsRed2 from the plasmid pIRES2-DsRed2 (Clontech), using compatible restriction enzyme sites BamHI and NotI. The resulting $pCaM_{1234}$-IR-DsRed2 construct permitted identification of cells co-expressing the *Trichoplax* Ca_V channels and EGFP from the bicistronic pIRES2-EGFP plasmid and CaM_{1234} plus DsRed2 from the pIRES2-DsRed2 plasmid. For these experiments, 1 μg of the $pCaM_{1234}$-IR-dsRed2 construct was included in transfections used for general electrophysiology experiments as indicated above. For control conditions, this construct was excluded, allowing for endogenously expressed WT CaM to interact with and regulate the *in vitro* expressed channels as previously documented (83). To determine the effects of excluding either the rat $Ca_V\beta_{1b}$ or $Ca_V\alpha_2\delta_1$ subunits, or both, on TCa_V1 channel biophysical properties, HEK-293T cells were transfected with 1 μg of the $pTCa_V1$-IR-EGFP, 0.5 μg of Kir2.1 cDNA, and either 1 μg of the rat $Ca_V\beta_{1b}$ subunit or $Ca_V\alpha_2\delta_1$ subunit. For experiments involving G-proteins, transfections were carried out using 1 μg of $pTCa_V1$-IR-EGFP, 1 μg each of rat $Ca_V\beta_{1b}$ and $Ca_V\alpha_2\delta_1$ subunit cDNAs, 1.5 μg of the *Trichoplax* $G\beta_1$ subunit cDNA, and 0.5 μg of each of the three *Trichoplax* Gγ subunit cDNAs ($G\gamma_1$-$G\gamma_3$) previously cloned into the pIRES2-DsRed2 vector (5). All transfections were performed using PolyJet transfection reagent (SignaGen Laboratories), according to the manufacturer's instructions for 4 to 6 h, after which cells were washed and transferred to a 37 °C incubator overnight. The next day, cells were treated with trypsin (Sigma-Aldrich), plated onto tissue culture–treated 35-mm cell culture dishes (Eppendorf), and incubated at 37 °C overnight or at 28 °C for 2 to 3 nights. For patch clamp experiments, media were aspirated from culture dishes, and these were washed and filled with 3 ml of appropriate extracellular recoding solution.

For whole-cell patch clamp recording of macroscopic Ca^{2+} currents, an extracellular recording solution containing 140 mM tetraethylammonium chloride (TEA-Cl), 2 mM $MgCl_2$, 3 mM $CaCl_2$, 10 mM glucose, and 10 mM Hepes (pH 7.4 with TEA-OH, 320 mOsM with glucose) was used. Electrodes were filled with pipette solution containing 120 mM CsCl, 1 mM $MgCl_2$, 10 mM Hepes, 10 mM EGTA, 4 mM Mg-ATP, and 0.3 mM Li-GTP (pH 7.2 with CsOH, 300 mOsM with glucose). For pharmacology experiments, a 300 mM stock solution of Cd^{2+} was prepared by dissolving powder in ultrapure water. 100 mM stocks of *R*(+)-BayK 8644, *S*(-)-BayK 8644 (Alomone Labs Ltd), and Nifedipine (Millipore Sigma), as well as a 10 mM stock of Isradipine (MilliporeSigma) were made by dissolving powders in dimethylsulfoxide. Stock solutions were diluted with the 3 mM external Ca^{2+} solution to the final working concentrations. The dimethylsulfoxide concentration

in the working solutions did not exceed 0.1%. For WT CaM and CaM_{1234} experiments, the external solution contained 140 mM TEA-Cl, 5 mM $CaCl_2$ or $BaCl_2$, and 10 mM Hepes (pH 7.3 with TEA-OH, 300 mOsM with glucose), and the internal solution contained 140 mM CsCl, 1 mM $MgCl_2$, 10 mM Hepes, 4 mM Mg-ATP, as well as either 0.5 mM EGTA or 10 mM BAPTA (pH 7.3 with CsOH, 290 mOsM with glucose). Unless otherwise indicated, all reagents for electrophysiological saline solutions were obtained from MilliporeSigma and were of >99% purity.

To perform whole-cell patch voltage-clamp recordings, an Axopatch 200B amplifier (Axon Instruments) and a Digidata 1440A digitizer controlled with pCLAMP 10 software (Molecular Devices) were used. Pipettes were pulled using a Sutter P-1000 micropipette puller from thick-walled borosilicate capillary tubes (1.5-mm outer and 0.86-mm inner diameter, Sutter) and fire polished with a Narishige MF-900 Microforge to obtain a pipette resistance between 2 to 5 MΩ. With the exception of the repetitive depolarization protocols (see below), series resistance was not compensated, and recordings were sampled at 10 kHz. The recordings were filtered offline at 500 Hz and leak-subtracted (baseline adjustment) using the pCLAMP software. For recordings of the deactivation kinetics, a P/4 leak subtraction protocol was performed to remove the capacitative currents. Only recordings that had minimal access resistance and minimal leak currents (*i.e.*, <10% of peak inward current) were used for analyses. For the repetitive depolarization protocols, the peak current amplitudes were determined by depolarizing the cell membrane to 0 mV for 500 ms (*i.e.*, the "step pulse"). For the train of depolarization pulses, 70 % series resistance compensation was obtained, and a P/4 leak subtraction protocol was performed for all the recordings. Currents were sampled at 100 kHz and filtered offline at 5 kHz. To determine the charge, currents were integrated over the 1 s period of train depolarizations (*i.e.*, the area under individual inward peaks was summed) using pClamp, and the results were expressed in picocoulombs, pC. The integral was then divided by the peak current amplitude elicited by a 500 ms step pulse to +5 mV to obtain pC/pA. Only the area under the tail currents was used to calculate pC/pA to avoid any artifacts of leak subtraction.

For pharmacology experiments, the Valvelink8.2 gravity flow Teflon perfusion system (Auto-Mate Scientific) was used. Normalized conductance values were obtained by transforming peak current–voltage data using Equation 1, where G_{ion} is the conductance for Ca^{2+} at a given command voltage ($V_{command}$), I_{peak} is the peak amplitude of the macroscopic inward current, and E_{ion} is the Ca^{2+} reversal potential determined by linear extrapolation of the ascending components of the current–voltage data.

$$G_{ion} = \frac{I_{peak}}{V_{command} - V_{ion}} \tag{1}$$

Tau (τ) values for quantifying kinetics of channel activation, inactivation, and deactivation were obtained by mono-exponential/biexponential curve fitting of current traces with the pCLAMP software using Equation 2. Here, A is the amplitude, τ is the time constant, C is the y-offset constant, *n* is the number of terms, and *i* represents each component.

$$f(t) = \sum_{i=1}^{n} A_i e^{-\frac{t}{\tau_i}} + C \tag{2}$$

To quantify kinetics of channel recovery from inactivation, τ values were obtained by fitting a biexponential function (Equation 3) on the data using the software package Origin 2016. Here, y0 represents the offset, A1 and A2 represent current amplitudes, and t1 and t2 represent time constants. Tau values were calculated based on Equation 4 and averaged to obtain τ1 ± SD and τ2 ± SD

$$y = y0 + A_1 e^{-x/t_1} + A_2 e^{-x/t_2} \tag{3}$$

$$\tau_1 = t1 \times \ln(2) \quad \tau_2 = t2 \times \ln(2) \tag{4}$$

Boltzmann functions (Equation 5) were fitted over conductance and inactivation curves to obtain $V_{1/2}$ and the k slope factor values. In this equation, A1 and A2 represent the initial and final values, respectively, x0 is the center of the curve, and dx is the time constant. Mean $V_{1/2}$ ± SD was obtained by averaging x0 values, and mean k ± SD was obtained by averaging dx values.

$$y = \frac{A1 - A2}{1 + e^{(x - x0)/dx}} + A2 \tag{5}$$

IC_{50} and Hill coefficient values for Cd^{2+} dose–response curves were determined by fitting monophasic dose–response curves over the data (Equation 6). A1 and A2 represent the bottom and top asymptotes, logx0 represents the center of the curve, and the *p* value is the hill slope. The mean ± SD of the Hill coefficients were calculated by averaging *p* values, and the IC_{50} values were calculated using Equation 7 and averaged to obtain the mean ± SD. All $V_{1/2}$, k, IC_{50}, and Hill coefficient values were calculated using Origin 2016 (OriginLab).

$$y = \frac{A2 - A1}{1 + 10^{(logx0 - x)p}} \tag{6}$$

$$IC_{50} = 10^{logx0} \tag{7}$$

Statistical analyses

Data are expressed as mean ± SD. All statistical analyses (ANOVAs and Student's *t* tests) were performed using SigmaPlot 14.0 (Systat Software Inc, San Jose, CA).

Data availability

All data are contained in this manuscript with the exception of the gene sequence for the cloned *Trichoplax* Ca_V1 channel

cDNA that is available on GenBank with accession number MW915585.

Supporting information—This article contains supporting information (32, 38, 106, 108, 109).

Acknowledgments—We thank Dr Terry Snutch (University of British Columbia) *via* Drs Gerald Zamponi (University of Calgary) and David Spafford (University of Waterloo) for generously gifting us the rat $Ca_V1.2$, $Ca_V\beta_{1b}$, and $Ca_V\alpha_2\delta_1$ expression plasmids and Dr Lily Jan (University of California, San Francisco) for generously gifting us the Kir2.1 expression plasmid.

Author contribution—Adriano Senatore conceptualization; Adriano Senatore supervision; Adriano Senatore, J. G., C. L. S., W. E., and Anhadvir Singh investigation; Adriano Senatore and J. G. methodology; Adriano Senatore, J. G., and C. L. S. visualization; Adriano Senatore and J. G. writing-original draft; J. G., C. L. S., W. E., and Anhadvir Singh formal analysis; C. L. S., W. E., and Anhadvir Singh writing-review and editing.

Funding and additional information—This project was funded by an NSERC Discovery Grant (RGPIN-2016-06023), a Canadian Foundation for Innovation Grant (35297), and an Ontario Early Researcher Award (ER17-13-247) to Adriano Senatore, an NSERC Canadian Graduate Scholarship to J. G., and the Intramural Research Program of the NIH, NINDS to C. L. S. The content is solely the responsibility of the authors and does not necessarily represent the official views of the National Institutes of Health.

Conflict of interest—The authors declare that they have no conflicts of interest with the contents of this article.

Abbreviations—The abbreviations used are: AID, Alpha interaction domain; APs, Action potentials; ASW, Artificial seawater; BLAST, Basic Local Alignment Search Tool; Ca^{2+}, Calcium; CaM, Calmodulin; Ca_V, Voltage-gated calcium channel; Cd^{2+}, Cadmium; CDI, Calcium-dependent inactivation; DI, DII, DIII, DIV, Domains I, II, III, IV; DHPs, Dihydropyridines; EF, Helix-loop-helix; EGFP, Enhanced green fluorescence protein; FISH, Fluorescence *in situ* hybridization; HEK, Human embryonic kidney cell; HVA, High-voltage–activated; IRES, Internal ribosome entry site; K^+, Potassium; Kir, Inward rectifying potassium channel; LCa_V, *Lymnaea stagnalis* voltage-gated calcium channel; Na_V, Voltage-gated sodium channel; NSCaTE, N-terminal Spatial Ca^{2+} Transforming Element; S1–6, Segments 1 to 6; TCaV, *T. adhaerens* voltage-gated calcium channel; TEA, Tetraethylammonium; VDI, Voltage-dependent inactivation; vWA, von Willebrand factor type A; WGA, Wheat germ agglutinin.

References

1. Pozdnyakov, I., Matantseva, O., and Skarlato, S. (2018) Diversity and evolution of four-domain voltage-gated cation channels of eukaryotes and their ancestral functional determinants. *Sci. Rep.* **8**, 1–10
2. Catterall, W. A. (2011) Voltage-gated calcium channels. *Cold Spring Harb. Perspect. Biol.* **3**, a003947
3. Ertel, E. A., Campbell, K. P., Harpold, M. M., Hofmann, F., Mori, Y., Perez-Reyes, E., Schwartz, A., Snutch, T. P., Tanabe, T., and Birnbaumer, L. (2000) Nomenclature of voltage-gated calcium channels. *Neuron* **25**, 533–535
4. Moran, Y., and Zakon, H. H. (2014) The evolution of the four subunits of voltage-gated calcium channels: Ancient roots, increasing complexity, and multiple losses. *Genome Biol. Evol.* **6**, 2210–2217
5. Gauberg, J., Abdallah, S., Elkhatib, W., Harracksingh, A. N., Piekut, T., Stanley, E. F., and Senatore, A. (2020) Conserved biophysical features of the CaV2 presynaptic Ca2+ channel homologue from the early-diverging animal Trichoplax adhaerens. *J. Biol. Chem.* **295**, 18553–18578
6. Dolphin, A. C. (2016) Voltage-gated calcium channels and their auxiliary subunits: Physiology and pathophysiology and pharmacology. *J. Physiol.* **594**, 5369–5390
7. Dawson, T. F., Boone, A. N., Senatore, A., Piticaru, J., Thiyagalingam, S., Jackson, D., Davison, A., and Spafford, J. D. (2014) Gene splicing of an invertebrate beta subunit (LCavβ) in the N-terminal and HOOK domains and its regulation of LCav1 and LCav2 calcium channels. *PLoS One* **9**, e92941
8. Segura, E., Mehta, A., Marsolais, M., Quan, X. R., Zhao, J., Sauvé, R., Spafford, J. D., and Parent, L. (2020) An ancestral MAGUK protein supports the modulation of mammalian voltage-gated Ca2+ channels through a conserved CaVβ–like interface. *Biochim. Biophys. Acta Biomembr.* **1862**, 183439
9. Mehta, A. (2016) *Cloning and Characterization of Voltage-Gated Sodium and Calcium Channel Homologs from the Single-Cell Choanoflagellate, Salpingoeca Rosetta*, UWSpace, University of Waterloo, Waterloo, Ontario, Canada
10. Ben-Johny, M., and Yue, D. T. (2014) Calmodulin regulation (calmodulation) of voltage-gated calcium channels. *J. Gen. Physiol.* **143**, 679–692
11. Bayley, P., Ahlström, P., Martin, S. R., and Forsen, S. (1984) The kinetics of calcium binding to calmodulin: Quin 2 and ANS stopped-flow fluorescence studies. *Biochem. Biophys. Res. Commun.* **120**, 185–191
12. Peterson, B. Z., DeMaria, C. D., and Yue, D. T. (1999) Calmodulin is the Ca^{2+} sensor for Ca^{2+}-dependent inactivation of L-type calcium channels. *Neuron* **22**, 549–558
13. Dick, I. E., Tadross, M. R., Liang, H., Tay, L. H., Yang, W., and Yue, D. T. (2008) A modular switch for spatial Ca 2+ selectivity in the calmodulin regulation of Ca V channels. *Nature* **451**, 830–834
14. Simms, B. A., Souza, I. A., and Zamponi, G. W. (2014) A novel calmodulin site in the Cav1. 2 N-terminus regulates calcium-dependent inactivation. *Pflügers Arch.* **466**, 1793–1803
15. Taiakina, V., Boone, A. N., Fux, J., Senatore, A., Weber-Adrian, D., Guillemette, J. G., and Spafford, J. D. (2013) The calmodulin-binding, short linear motif, NSCaTE is conserved in L-type channel ancestors of vertebrate Cav1. 2 and Cav1. 3 channels. *PLoS One* **8**, e61765
16. Spafford, J. D., Chen, L., Feng, Z.-P., Smit, A. B., and Zamponi, G. W. (2003) Expression and modulation of an invertebrate presynaptic calcium channel α1 subunit homolog. *J. Biol. Chem.* **278**, 21178–21187
17. Senatore, A., Zhorov, B. S., and Spafford, J. D. (2012) Cav3 T-type calcium channels. *Wiley Interdiscip. Rev. Membr. Transp. Signal.* **1**, 467–491
18. Smith, C. L., Varoqueaux, F., Kittelmann, M., Azzam, R. N., Cooper, B., Winters, C. A., Eitel, M., Fasshauer, D., and Reese, T. S. (2014) Novel cell types, neurosecretory cells, and body plan of the early-diverging metazoan Trichoplax adhaerens. *Curr. Biol.* **24**, 1565–1572
19. Srivastava, M., Begovic, E., Chapman, J., Putnam, N. H., Hellsten, U., Kawashima, T., Kuo, A., Mitros, T., Salamov, A., and Carpenter, M. L. (2008) The Trichoplax genome and the nature of placozoans. *Nature* **454**, 955–960
20. Wong, Y. Y., Le, P., Elkhatib, W., Piekut, T., and Senatore, A. (2019) Transcriptome profiling of *Trichoplax adhaerens* highlights its digestive epithelium and a rich set of genes for fast electrogenic and slow neuromodulatory cellular signaling. *Res Sq*. https://doi.org/10.21203/rs.2.14504/v1
21. Romanova, D. Y., Smirnov, I. V., Nikitin, M. A., Kohn, A. B., Borman, A. I., Malyshev, A. Y., Balaban, P. M., and Moroz, L. L. (2020) Sodium action potentials in placozoa: Insights into behavioral integration and evolution of nerveless animals. *Biochem. Biophys. Res. Commun.* **532**, 120–126
22. Wang, D. Y.-C., Kumar, S., and Hedges, S. B. (1999) Divergence time estimates for the early history of animal phyla and the origin of plants, animals and fungi. *Proc. Biol. Sci.* **266**, 163–171

23. Peterson, K. J., Lyons, J. B., Nowak, K. S., Takacs, C. M., Wargo, M. J., and McPeek, M. A. (2004) Estimating metazoan divergence times with a molecular clock. *Proc. Natl. Acad. Sci. U. S. A.* **101**, 6536–6541
24. Smith, C. L., Abdallah, S., Wong, Y. Y., Le, P., Harracksingh, A. N., Artinian, L., Tamvacakis, A. N., Rehder, V., Reese, T. S., and Senatore, A. (2017) Evolutionary insights into T-type Ca2+ channel structure, function, and ion selectivity from the Trichoplax adhaerens homologue. *J. Gen. Physiol.* **149**, 483–510
25. Gauberg, J., Senatore, A., and Heyland, A. (2021) Functional studies of Trichoplax adhaerens voltage-gated calcium channel activity. In *Developmental Biology of the Sea Urchin and Other Marine Invertebrates*, Humana Press, Totowa, NJ: 277–288
26. Leys, S. P. (2015) Elements of a 'nervous system'in sponges. *J. Exp. Biol.* **218**, 581–591
27. Moroz, L. L. (2021) Multiple origins of neurons from secretory cells. *Front. Cell Dev. Biol.* **9**, 669087
28. Whelan, N. V., Kocot, K. M., Moroz, T. P., Mukherjee, K., Williams, P., Paulay, G., Moroz, L. L., and Halanych, K. M. (2017) Ctenophore relationships and their placement as the sister group to all other animals. *Nat. Ecol. Evol.* **1**, 1737–1746
29. Chan, J. D., Zhang, D., Liu, X., Zarowiecki, M., Berriman, M., and Marchant, J. S. (2017) Utilizing the planarian voltage-gated ion channel transcriptome to resolve a role for a Ca2+ channel in neuromuscular function and regeneration. *Biochim. Biophys. Acta Mol. Cell Res.* **1864**, 1036–1045
30. Senatore, A., Raiss, H., and Le, P. (2016) Physiology and evolution of voltage-gated calcium channels in early diverging animal phyla: Cnidaria, placozoa, porifera and ctenophora. *Front. Physiol.* **7**, 481
31. Jeziorski, M. C., Greenberg, R. M., Clark, K. S., and Anderson, P. A. (1998) Cloning and functional expression of a voltage-gated calcium channel α1 subunit from jellyfish. *J. Biol. Chem.* **273**, 22792–22799
32. Tikhonov, D. B., and Zhorov, B. S. (2011) Possible roles of exceptionally conserved residues around the selectivity filters of sodium and calcium channels. *J. Biol. Chem.* **286**, 2998–3006
33. Tang, L., El-Din, T. M. G., Payandeh, J., Martinez, G. Q., Heard, T. M., Scheuer, T., Zheng, N., and Catterall, W. A. (2014) Structural basis for Ca 2+ selectivity of a voltage-gated calcium channel. *Nature* **505**, 56–61
34. Stephens, R. F., Guan, W., Zhorov, B. S., and Spafford, J. D. (2015) Selectivity filters and cysteine-rich extracellular loops in voltage-gated sodium, calcium, and NALCN channels. *Front. Physiol.* **6**, 153
35. Catterall, W. A. (2010) Ion channel voltage sensors: Structure, function, and pathophysiology. *Neuron* **67**, 915–928
36. Yamaguchi, H., Muth, J. N., Varadi, M., Schwartz, A., and Varadi, G. (1999) Critical role of conserved proline residues in the transmembrane segment 4 voltage sensor function and in the gating of L-type calcium channels. *Proc. Natl. Acad. Sci. U. S. A.* **96**, 1357–1362
37. Opatowsky, Y., Chen, C.-C., Campbell, K. P., and Hirsch, J. A. (2004) Structural analysis of the voltage-dependent calcium channel β subunit functional core and its complex with the α1 interaction domain. *Neuron* **42**, 387–399
38. Chen, Y.-h., Li, M.-h., Zhang, Y., He, L.-l., Yamada, Y., Fitzmaurice, A., Shen, Y., Zhang, H., Tong, L., and Yang, J. (2004) Structural basis of the α1–β subunit interaction of voltage-gated Ca^{2+} channels. *Nature* **429**, 675–680
39. Bourdin, B., Briot, J., Tétreault, M.-P., Sauvé, R., and Parent, L. (2017) Negatively charged residues in the first extracellular loop of the L-type CaV1. 2 channel anchor the interaction with the CaVα2δ1 auxiliary subunit. *J. Biol. Chem.* **292**, 17236–17249
40. Kamm, K., Osigus, H.-J., Stadler, P. F., DeSalle, R., and Schierwater, B. (2018) Trichoplax genomes reveal profound admixture and suggest stable wild populations without bisexual reproduction. *Sci. Rep.* **8**, 1–11
41. Eitel, M., Francis, W. R., Varoqueaux, F., Daraspe, J., Osigus, H.-J., Krebs, S., Vargas, S., Blum, H., Williams, G. A., and Schierwater, B. (2018) Comparative genomics and the nature of placozoan species. *PLoS Biol.* **16**, e2005359
42. Te Velthuis, A. J., Admiraal, J. F., and Bagowski, C. P. (2007) Molecular evolution of the MAGUK family in metazoan genomes. *BMC Evol. Biol.* **7**, 1–10
43. Lainé, V., Frøkjær-Jensen, C., Couchoux, H., and Jospin, M. (2011) The α1 subunit EGL-19, the α2/δ subunit UNC-36, and the β subunit CCB-1 underlie voltage-dependent calcium currents in Caenorhabditis elegans striated muscle. *J. Biol. Chem.* **286**, 36180–36187
44. Richards, M. W., Leroy, J., Pratt, W. S., and Dolphin, A. C. (2007) The HOOK-domain between the SH3-and the GK-domains of CaVβ subunits contains key determinants controlling calcium channel inactivation. *Channels* **1**, 92–101
45. He, L.-l., Zhang, Y., Chen, Y.-H., Yamada, Y., and Yang, J. (2007) Functional modularity of the β-subunit of voltage-gated Ca2+ channels. *Biophys. J.* **93**, 834–845
46. Cottrell, G. S., Soubrane, C. H., Hounshell, J. A., Lin, H., Owenson, V., Rigby, M., Cox, P. J., Barker, B. S., Ottolini, M., and Ince, S. (2018) CACHD1 is an α2δ-like protein that modulates CaV3 voltage-gated calcium channel activity. *J. Neurosci.* **38**, 9186–9201
47. Stephens, G. J., and Cottrell, G. S. (2019) CACHD1: A new activity-modifying protein for voltage-gated calcium channels. *Channels* **13**, 120–123
48. Canti, C., Nieto-Rostro, M., Foucault, I., Heblich, F., Wratten, J., Richards, M., Hendrich, J., Douglas, L., Page, K., and Davies, A. (2005) The metal-ion-dependent adhesion site in the Von Willebrand factor-A domain of α2δ subunits is key to trafficking voltage-gated Ca2+ channels. *Proc. Natl. Acad. Sci. U. S. A.* **102**, 11230–11235
49. Davies, A., Kadurin, I., Alvarez-Laviada, A., Douglas, L., Nieto-Rostro, M., Bauer, C. S., Pratt, W. S., and Dolphin, A. C. (2010) The α2δ subunits of voltage-gated calcium channels form GPI-anchored proteins, a posttranslational modification essential for function. *Proc. Natl. Acad. Sci. U. S. A.* **107**, 1654–1659
50. Spafford, J. D., Dunn, T., Smit, A. B., Syed, N. I., and Zamponi, G. W. (2006) *In vitro* characterization of L-type calcium channels and their contribution to firing behavior in invertebrate respiratory neurons. *J. Neurophysiol.* **95**, 42–52
51. Spafford, J. D., Munno, D. W., Van Nierop, P., Feng, Z.-P., Jarvis, S. E., Gallin, W. J., Smit, A. B., Zamponi, G. W., and Syed, N. I. (2003) Calcium channel structural determinants of synaptic transmission between identified invertebrate neurons. *J. Biol. Chem.* **278**, 4258–4267
52. Jeziorski, M. C., Greenberg, R. M., and Anderson, P. (1999) Cloning and expression of a jellyfish calcium channel beta subunit reveal functional conservation of the alpha1-beta interaction. *Recept. Channels* **6**, 375–386
53. Dolphin, A. C. (2012) Calcium channel auxiliary $\alpha_2\delta$ and β subunits: Trafficking and one step beyond. *Nat. Rev. Neurosci.* **13**, 542–555
54. Gul, I. S., Staal, J., Hulpiau, P., De Keuckelaere, E., Kamm, K., Deroo, T., Sanders, E., Staes, K., Driege, Y., and Saeys, Y. (2018) GC content of early metazoan genes and its impact on gene expression levels in mammalian cell lines. *Genome Biol. Evol.* **10**, 909–917
55. Michailidis, I. E., Abele-Henckels, K., Zhang, W. K., Lin, B., Yu, Y., Geyman, L. S., Ehlers, M. D., Pnevmatikakis, E. A., and Yang, J. (2014) Age-related homeostatic midchannel proteolysis of neuronal L-type voltage-gated Ca2+ channels. *Neuron* **82**, 1045–1057
56. Mayorova, T. D., Hammar, K., Winters, C. A., Reese, T. S., and Smith, C. L. (2019) The ventral epithelium of Trichoplax adhaerens deploys in distinct patterns cells that secrete digestive enzymes, mucus or diverse neuropeptides. *Biol. Open* **8**, bio045674
57. Armon, S., Bull, M. S., Aranda-Diaz, A., and Prakash, M. (2018) Ultrafast epithelial contractions provide insights into contraction speed limits and tissue integrity. *Proc. Natl. Acad. Sci. U. S. A.* **115**, E10333–E10341
58. Sebé-Pedrós, A., Chomsky, E., Pang, K., Lara-Astiaso, D., Gaiti, F., Mukamel, Z., Amit, I., Hejnol, A., Degnan, B. M., and Tanay, A. (2018) Early metazoan cell type diversity and the evolution of multicellular gene regulation. *Nat. Ecol. Evol.* **2**, 1176–1188
59. Mahapatra, S., Calorio, C., Vandael, D. H. F., Marcantoni, A., Carabelli, V., and Carbone, E. (2012) Calcium channel types contributing to chromaffin cell excitability, exocytosis and endocytosis. *Cell Calcium* **51**, 321–330
60. Mayorova, T. D., Hammar, K., Jung, J. H., Aronova, M. A., Zhang, G., Winters, C. A., Reese, T. S., and Smith, C. L. (2021) Placozoan fiber cells:

Mediators of innate immunity and participants in wound healing. *Sci. Rep.* **11**, 1–18
61. Tomlinson, W. J., Stea, A., Bourinet, E., Charnet, P., Nargeot, J., and Snutch, T. P. (1993) Functional properties of a neuronal class C L-type calcium channel. *Neuropharmacology* **32**, 1117–1126
62. Kubo, Y., Baldwin, T. J., Jan, Y. N., and Jan, L. Y. (1993) Primary structure and functional expression of a mouse inward rectifier potassium channel. *Nature* **362**, 127–133
63. Kirkton, R. D., and Bursac, N. (2011) Engineering biosynthetic excitable tissues from unexcitable cells for electrophysiological and cell therapy studies. *Nat. Commun.* **2**, 1–9
64. Dreyfus, F. M., Tscherter, A., Errington, A. C., Renger, J. J., Shin, H.-S., Uebele, V. N., Crunelli, V., Lambert, R. C., and Leresche, N. (2010) Selective T-type calcium channel block in thalamic neurons reveals channel redundancy and physiological impact of ITwindow. *J. Neurosci.* **30**, 99–109
65. Adams, P. J., Garcia, E., David, L. S., Mulatz, K. J., Spacey, S. D., and Snutch, T. P. (2009) CaV2.1 P/Q-type calcium channel alternative splicing affects the functional impact of familial hemiplegic migraine mutations: Implications for calcium channelopathies. *Channels* **3**, 110–121
66. Ferreira, G., Ríos, E., and Reyes, N. (2003) Two components of voltage-dependent inactivation in $Ca_v1.2$ channels revealed by its gating currents. *Biophys. J.* **84**, 3662–3678
67. Lacinová, L., and Hofmann, F. (2005) Ca^{2+}- and voltage-dependent inactivation of the expressed L-type $Ca_v1.2$ calcium channel. *Arch. Biochem. Biophys.* **437**, 42–50
68. Llinas, R., Steinberg, I. Z., and Walton, K. (1981) Presynaptic calcium currents in squid giant synapse. *Biophys. J.* **33**, 289–321
69. Perez-Reyes, E. (2003) Molecular physiology of low-voltage-activated t-type calcium channels. *Physiol. Rev.* **83**, 117–161
70. Mayorova, T. D., Smith, C. L., Hammar, K., Winters, C. A., Pivovarova, N. B., Aronova, M. A., Leapman, R. D., and Reese, T. S. (2018) Cells containing aragonite crystals mediate responses to gravity in Trichoplax adhaerens (Placozoa), an animal lacking neurons and synapses. *PLoS One* **13**, e0190905
71. Li, X., Liu, H., Luo, J. C., Rhodes, S. A., Trigg, L. M., Van Rossum, D. B., Anishkin, A., Diatta, F. H., Sassic, J. K., and Simmons, D. K. (2015) Major diversification of voltage-gated K+ channels occurred in ancestral parahoxozoans. *Proc. Natl. Acad. Sci. U. S. A.* **112**, E1010–E1019
72. Simms, B. A., and Zamponi, G. W. (2014) Neuronal voltage-gated calcium channels: Structure, function, and dysfunction. *Neuron* **82**, 24–45
73. Lipscombe, D., Helton, T. D., and Xu, W. (2004) L-type calcium channels: The low down. *J. Neurophysiol.* **92**, 2633–2641
74. Senatore, A., Boone, A., Lam, S., Dawson, T. F., Zhorov, B., and Spafford, J. (2011) Mapping of dihydropyridine binding residues in a less sensitive invertebrate L-type calcium channel (LCav1). *Channels* **5**, 173–187
75. Mitterdorfer, J., Wang, Z., Sinnegger, M. J., Hering, S., Jörg, S., Grabner, M., and Glossmann, H. (1996) Two amino acid residues in the IIIS5 segment of L-type calcium channels differentially contribute to 1,4-dihydropyridine sensitivity. *J. Biol. Chem.* **271**, 30330–30335
76. Wappl, E., Mitterdorfer, J., Glossmann, H., and Striessnig, J. (2001) Mechanism of dihydropyridine interaction with critical binding residues of L-type Ca2+ channel α1 subunits. *J. Biol. Chem.* **276**, 12730–12735
77. Yamaguchi, S., Zhorov, B. S., Yoshioka, K., Nagao, T., Ichijo, H., and Adachi-Akahane, S. (2003) Key roles of Phe1112 and Ser1115 in the pore-forming IIIS5-S6 linker of L-type Ca2+ channel α1C subunit (CaV 1.2) in binding of dihydropyridines and action of Ca2+ channel agonists. *Mol. Pharmacol.* **64**, 235–248
78. Kwok, T. C., Hui, K., Kostelecki, W., Ricker, N., Selman, G., Feng, Z.-P., and Roy, P. J. (2008) A genetic screen for dihydropyridine (DHP)-resistant worms reveals new residues required for DHP-blockage of mammalian calcium channels. *PLoS Genet.* **4**, e1000067
79. Tikhonov, D. B., and Zhorov, B. S. (2009) Structural model for dihydropyridine binding to L-type calcium channels. *J. Biol. Chem.* **284**, 19006–19017
80. Zhao, Y., Huang, G., Wu, J., Wu, Q., Gao, S., Yan, Z., Lei, J., and Yan, N. (2019) Molecular basis for ligand modulation of a mammalian voltage-gated Ca2+ channel. *Cell* **177**, 1495–1506.e12
81. Kass, R. (1987) Voltage-dependent modulation of cardiac calcium channel current by optical isomers of Bay K 8644: Implications for channel gating. *Circ. Res.* **61**, I1–5
82. Ravens, U., and Schöpper, H.-P. (1990) Opposite cardiac actions of the enantiomers of Bay K 8644 at different membrane potentials in Guinea-pig papillary muscles. *Naunyn Schmiedebergs Arch. Pharmacol.* **341**, 232–239
83. Bazzazi, H., Johny, M. B., Adams, P. J., Soong, T. W., and Yue, D. T. (2013) Continuously tunable Ca^{2+} regulation of RNA-edited $Ca_V1.3$ channels. *Cell Rep.* **5**, 367–377
84. Van Petegem, F., Chatelain, F. C., and Minor, D. L. (2005) Insights into voltage-gated calcium channel regulation from the structure of the Ca V 1.2 IQ domain–Ca 2+/calmodulin complex. *Nat. Struct. Mol. Biol.* **12**, 1108–1115
85. Mori, M. X., Vander Kooi, C. W., Leahy, D. J., and Yue, D. T. (2008) Crystal structure of the CaV2 IQ domain in complex with Ca2+/calmodulin: High-resolution mechanistic implications for channel regulation by Ca2+. *Structure* **16**, 607–620
86. Fallon, J. L., Halling, D. B., Hamilton, S. L., and Quiocho, F. A. (2005) Structure of calmodulin bound to the hydrophobic IQ domain of the cardiac Cav1. 2 calcium channel. *Structure* **13**, 1881–1886
87. Eckert, R., and Tillotson, D. L. (1981) Calcium-mediated inactivation of the calcium conductance in caesium-loaded giant neurones of *Aplysia californica*. *J. Physiol.* **314**, 265–280
88. Chi, C.-H., Tang, C.-Y., and Pan, C.-Y. (2017) Calmodulin modulates the Ca2+-dependent inactivation and expression level of bovine CaV2. 2 expressed in HEK293T cells. *IBRO Rep.* **2**, 63–71
89. Banerjee, R., Yoder, J. B., Yue, D. T., Amzel, L. M., Tomaselli, G. F., Gabelli, S. B., and Ben-Johny, M. (2018) Bilobal architecture is a requirement for calmodulin signaling to CaV1. 3 channels. *Proc. Natl. Acad. Sci. U. S. A.* **115**, E3026–E3035
90. Tedford, H. W., and Zamponi, G. W. (2006) Direct G protein modulation of Cav2 calcium channels. *Pharmacol. Rev.* **58**, 837–862
91. Senatore, A., and Spafford, J. D. (2010) Transient and big are key features of an invertebrate T-type channel (LCav3) from the central nervous system of Lymnaea stagnalis. *J. Biol. Chem.* **285**, 7447–7458
92. Cens, T., Rousset, M., Collet, C., Charreton, M., Garnery, L., Le Conte, Y., Chahine, M., Sandoz, J.-C., and Charnet, P. (2015) Molecular characterization and functional expression of the Apis mellifera voltage-dependent Ca2+ channels. *Insect Biochem. Mol. Biol.* **58**, 12–27
93. Ryan, J. F., Pang, K., Schnitzler, C. E., Nguyen, A.-D., Moreland, R. T., Simmons, D. K., Koch, B. J., Francis, W. R., Havlak, P., and Smith, S. A. (2013) The genome of the ctenophore *Mnemiopsis leidyi* and its implications for cell type evolution. *Science* **342**, 1242592
94. Moroz, L. L., Kocot, K. M., Citarella, M. R., Dosung, S., Norekian, T. P., Povolotskaya, I. S., Grigorenko, A. P., Dailey, C., Berezikov, E., and Buckley, K. M. (2014) The ctenophore genome and the evolutionary origins of neural systems. *Nature* **510**, 109–114
95. Simion, P., Philippe, H., Baurain, D., Jager, M., Richter, D. J., Di Franco, A., Roure, B., Satoh, N., Quéinnec, É., and Ereskovsky, A. (2017) A large and consistent phylogenomic dataset supports sponges as the sister group to all other animals. *Curr. Biol.* **27**, 958–967
96. Kapli, P., and Telford, M. J. (2020) Topology-dependent asymmetry in systematic errors affects phylogenetic placement of Ctenophora and Xenacoelomorpha. *Sci. Adv.* **6**, eabc5162
97. Blesneac, I., Chemin, J., Bidaud, I., Huc-Brandt, S., Vandermoere, F., and Lory, P. (2015) Phosphorylation of the $Ca_v3.2$ T-type calcium channel directly regulates its gating properties. *Proc. Natl. Acad. Sci. U. S. A.* **112**, 13705–13710
98. Kamp, T. J., and Hell, J. W. (2000) Regulation of cardiac L-type calcium channels by protein kinase A and protein kinase C. *Circ. Res.* **87**, 1095–1102
99. Fuller, M. D., Fu, Y., Scheuer, T., and Catterall, W. A. (2014) Differential regulation of CaV1. 2 channels by cAMP-dependent protein kinase

bound to A-kinase anchoring proteins 15 and 79/150. *J. Gen. Physiol.* **143**, 315–324
100. Catterall, W. A., and Few, A. P. (2008) Calcium channel regulation and presynaptic plasticity. *Neuron* **59**, 882–901
101. Tompa, P., Davey, N. E., Gibson, T. J., and Babu, M. M. (2014) A million peptide motifs for the molecular biologist. *Mol. Cell* **55**, 161–169
102. Zarin, T., Strome, B., Ba, A. N. N., Alberti, S., Forman-Kay, J. D., and Moses, A. M. (2019) Proteome-wide signatures of function in highly diverged intrinsically disordered regions. *Elife* **8**, e46883
103. Fernandez-Valverde, S. L., Calcino, A. D., and Degnan, B. M. (2015) Deep developmental transcriptome sequencing uncovers numerous new genes and enhances gene annotation in the sponge Amphimedon queenslandica. *BMC Genomics* **16**, 1–11
104. Guzman, C., and Conaco, C. (2016) Comparative transcriptome analysis reveals insights into the streamlined genomes of haplosclerid demosponges. *Sci. Rep.* **6**, 1–10
105. Tyson, J. R., and Snutch, T. P. (2013) Molecular nature of voltage-gated calcium channels: Structure and species comparison. *Wiley Interdiscip. Rev. Membr. Transp. Signal.* **2**, 181–206
106. Hering, S., Zangerl-Plessl, E.-M., Beyl, S., Hohaus, A., Andranovits, S., and Timin, E. (2018) Calcium channel gating. *Pflügers Arch.* **470**, 1291–1309
107. Dafi, O., Berrou, L., Dodier, Y., Raybaud, A., Sauvé, R., and Parent, L. (2004) Negatively charged residues in the N-terminal of the AID helix confer slow voltage dependent inactivation gating to CaV1. 2. *Biophys. J.* **87**, 3181–3192
108. Liao, P., Yu, D., Li, G., Yong, T. F., Soon, J. L., Chua, Y. L., and Soong, T. W. (2007) A smooth muscle Cav1. 2 calcium channel splice variant underlies hyperpolarized window current and enhanced state-dependent inhibition by nifedipine. *J. Biol. Chem.* **282**, 35133–35142
109. Tuluc, P., Molenda, N., Schlick, B., Obermair, G. J., Flucher, B. E., and Jurkat-Rott, K. (2009) A CaV1. 1 Ca2+ channel splice variant with high conductance and voltage-sensitivity alters EC coupling in developing skeletal muscle. *Biophys. J.* **96**, 35–44
110. Hofer, N. T., Pinggera, A., Nikonishyna, Y. V., Tuluc, P., Fritz, E. M., Obermair, G. J., and Striessnig, J. (2021) Stabilization of negative activation voltages of Cav1. 3 L-Type Ca2+-channels by alternative splicing. *Channels* **15**, 38–52
111. Weir, K., Dupre, C., van Giesen, L., Lee, A. S., and Bellono, N. W. (2020) A molecular filter for the cnidarian stinging response. *Elife* **9**, e57578
112. Kohn, A., Roberts-Misterly, J., Anderson, P., Khan, N., and Greenberg, R. (2003) Specific sites in the beta interaction domain of a schistosome Ca2+ channel β subunit are key to its role in sensitivity to the anti-schistosomal drug praziquantel. *Parasitology* **127**, 349–356
113. Salvador-Recatalà, V., Schneider, T., and Greenberg, R. M. (2008) Atypical properties of a conventional calcium channel β subunit from the platyhelminth Schistosoma mansoni. *BMC Physiol.* **8**, 1–11
114. Ben-Johny, M., Yang, P. S., Niu, J., Yang, W., Joshi-Mukherjee, R., and Yue, D. T. (2014) Conservation of Ca2+/calmodulin regulation across Na and Ca2+ channels. *Cell* **157**, 1657–1670
115. Catterall, W. A., Perez-Reyes, E., Snutch, T. P., and Striessnig, J. (2019) Voltage-gated calcium channels (version 2019.4) in the IUPHAR/BPS Guide to pharmacology database. *IUPHAR/BPS Guide Pharmacol. CITE* **2019**, 10.2218/gtopdb/F80/2019.4
116. Senatore, A., Guan, W., Boone, A. N., and Spafford, J. D. (2014) T-type channels become highly permeable to sodium ions using an alternative extracellular turret region (S5-P) outside the selectivity filter. *J. Biol. Chem.* **289**, 11952–11969
117. Steinmetz, P. R. H., Kraus, J. E. M., Larroux, C., Hammel, J. U., Amon-Hassenzahl, A., Houliston, E., Wörheide, G., Nickel, M., Degnan, B. M., and Technau, U. (2012) Independent evolution of striated muscles in cnidarians and bilaterians. *Nature* **487**, 231–234
118. Senatore, A., Reese, T. S., and Smith, C. L. (2017) Neuropeptidergic integration of behavior in Trichoplax adhaerens, an animal without synapses. *J. Exp. Biol.* **220**, 3381–3390
119. Patil, P. G., Brody, D. L., and Yue, D. T. (1998) Preferential closed-state inactivation of neuronal calcium channels. *Neuron* **20**, 1027–1038
120. Liu, Z., Ren, J., and Murphy, T. H. (2003) Decoding of synaptic voltage waveforms by specific classes of recombinant high-threshold Ca 2+ channels. *J. Physiol.* **553**, 473–488
121. Byczkowicz, N., Eshra, A., Montanaro, J., Trevisiol, A., Hirrlinger, J., Kole, M. H., Shigemoto, R., and Hallermann, S. (2019) HCN channel-mediated neuromodulation can control action potential velocity and fidelity in central axons. *Elife* **8**, e42766
122. Kozak, M. (1987) An analysis of 5'-noncoding sequences from 699 vertebrate messenger RNAs. *Nucleic Acids Res.* **15**, 8125–8148
123. Johnson, M., Zaretskaya, I., Raytselis, Y., Merezhuk, Y., McGinnis, S., and Madden, T. L. (2008) NCBI BLAST: A better web interface. *Nucleic Acids Res.* **36**, W5–W9
124. Thorington, G. U., and Hessinger, D. A. (2020) Activated L-type calcium channels inhibit chemosensitized nematocyst discharge from sea anemone tentacles. *Biol. Bull.* **238**, 180–192
125. Edgar, R. C. (2004) Muscle: Multiple sequence alignment with high accuracy and high throughput. *Nucleic Acids Res.* **32**, 1792–1797
126. Waterhouse, A. M., Procter, J. B., Martin, D. M., Clamp, M., and Barton, G. J. (2009) Jalview version 2—a multiple sequence alignment editor and analysis workbench. *Bioinformatics* **25**, 1189–1191
127. Käll, L., Krogh, A., and Sonnhammer, E. L. (2007) Advantages of combined transmembrane topology and signal peptide prediction—the Phobius web server. *Nucleic Acids Res.* **35**, W429–W432
128. Rice, P., Longden, I., and Bleasby, A. (2000) EMBOSS: The European molecular biology open software suite. *Trends Genet* **16**, 276–277
129. Jones, P., Binns, D., Chang, H.-Y., Fraser, M., Li, W., McAnulla, C., McWilliam, H., Maslen, J., Mitchell, A., and Nuka, G. (2014) InterProScan 5: Genome-scale protein function classification. *Bioinformatics* **30**, 1236–1240
130. Capella-Gutiérrez, S., Silla-Martínez, J. M., and Gabaldón, T. (2009) trimAl: A tool for automated alignment trimming in large-scale phylogenetic analyses. *Bioinformatics* **25**, 1972–1973
131. Nguyen, L.-T., Schmidt, H. A., Von Haeseler, A., and Minh, B. Q. (2015) IQ-TREE: A fast and effective stochastic algorithm for estimating maximum-likelihood phylogenies. *Mol. Biol. Evol.* **32**, 268–274
132. Schneider, C. A., Rasband, W. S., and Eliceiri, K. W. (2012) NIH image to ImageJ: 25 years of image analysis. *Nat. Methods* **9**, 671–675
133. Tamm, S. L., and Tamm, S. (1981) Ciliary reversal without rotation of axonemal structures in ctenophore comb plates. *J. Cell Biol.* **89**, 495–509